BROADBAND SPECTRAL CONTROL OF QUANTUM LIGHT WITH FREQUENCY CONVERSION

A Dissertation

Presented to the Faculty of the Graduate School

of Cornell University

in Partial Fulfillment of the Requirements for the Degree of

Doctor of Philosophy

by

Federico Presutti

August 2024

BROADBAND SPECTRAL CONTROL OF QUANTUM LIGHT WITH FREQUENCY CONVERSION

Federico Presutti, Ph.D.

Cornell University 2024

The preparation, control, and measurement of non-classical states of light are necessary to realizing optical quantum technologies. The frequency of light – the photon energy or its wavelength – is one of its fundamental degrees of freedom, within which we can manipulate a quantum state: for example, we can imagine preparing photons in superpositions of various wavelengths; or entangling photons such that their energies correlate. In contrast to the other luminal degrees of freedom, however, modifying the energy of photons requires nonlinear optics. The greater difficulty that this introduces in implementing quantum state transformations and measurements has proven to be an obstacle to the development of experimental methods for frequency-domain quantum optics. However, frequency-domain engineering would allow us to leverage the breadth of optical bandwidths, hence is advantageous for parallel quantum state generation and information encoding. In addition, the preparation of squeezed vacuum – the most accessible non-classical optical state – already relies on a frequency conversion process. This implies that the ability to combine the preparation and transformation steps into a joint nonlinear process may greatly benefit the efficiency and fidelity of producing the final state.

In this thesis I will present an experimental paradigm which uses ultrafast nonlinear optics and broadband frequency conversion techniques to enable the transformation and measurement of frequency-multimode squeezed vacuum states.

BIOGRAPHICAL SKETCH

Federico Presutti was born in 1995 in Ixelles, Belgium. Growing up in Brussels and New York City, he attended the European School of Brussels I and the United Nations International School in New York, from which he earned an IB diploma. In the summer of 2017, Federico graduated from the California Institute of Technology in Pasadena, CA, where he earned a Bachelor of Science in Applied Physics, with minors in Computer Science and Aerospace Engineering. In 2018, following a one-year gap in academics that he spent working in the San Francisco Bay Area, Federico joined the Cornell University doctoral program in Applied Physics in Ithaca, NY.

ACKNOWLEDGEMENTS

I would like to express my gratitude towards my advisor and the members of my committee, Professors Peter McMahon, Francesco Monticone and Frank Wise, for their support and the time spent advising me and sharing their invaluable experience regarding the world of research and academics. I am also grateful for the guidance of my colleagues, especially the postdoctoral scholars with whom I worked – namely: Logan Wright, Tianyu Wang, Tatsuhiro Onodera, Benjamin Malia, and Ryotatsu Yanagimoto – as well as graduate students, namely Shi-Yuan Ma. Finally, I would like to recognize the daily support I received from all members of the Applied Physics department, including staff and fellow students.

TABLE OF CONTENTS

Introduction

It is an understatement to say that modern light sources are important components of the science and engineering toolbox: these underpin an extensive series of diverse technologies that we now take for granted, in areas ranging from medicine, telecommunications, information storage, sensing and manufacturing – even entertainment. The developments of lasers and LEDs – light emitting diodes – and the discretion they have afforded us in fashioning electromagnetic waves, can be regarded as the major scientific breakthroughs of the past century. These scientific advances were enabled in large part by the advent of quantum mechanics.

The physics of light has always been at the forefront of the quantum sciences: blackbody radiation and the photoelectric effect were among the scientific mysteries that motivated the development of quantum mechanics. Indeed, classical physics could not properly explain how the simple incandescent lamp radiates light – a clue that a quantum theory of light was needed. In its maturity, quantum mechanics led us to the theories of stimulated emission and electron-hole recombination, which made lasers and LEDs possible.

Despite the fact that the physics underlying much of light-matter interaction and light emission requires a quantum-mechanical description, the kind of light generated by the majority of our sources can be entirely described by classical physics. This excludes a large space of possibilities. The scientific frontier, arguably, now lies in producing and exploiting non-classical states of light: states of the electromagnetic field that require a quantum-mechanical description. To date, the most prominent example of this has been at the Laser Interferometer Gravitational-Wave Observatory, LIGO [1]. The use of "squeezed" light allows measurements with significantly improved sensitivity, in a manner that derives essentially from exploiting Heisenberg's uncertainty relation.

This, however, is "big science;" the question is whether we can develop and adopt quantum light more broadly, and whether existing technologies can be enhanced to use quantum light.

The nature, or physical behavior, of light changes first as its wave aspects become more important, and then once again as the particle aspects become pronounced. Namely, once the mathematical description of a state of light requires considering its individual quanta – photons – the number of degrees of freedom explodes exponentially. This is interesting from a scientific point of view, since, in principle, it means that quantum light "engineering" may intrinsically require more control than classical light. Indeed, depending on the context, we may wish to find ways to either exploit this enormous complexity, or instead to minimize it (often, these two cases must be satisfied simultaneously, should we need to embed the complexity in one luminal degree of freedom – space and wavevector; time and frequency; polarization; etc. – while isolating it from any other).

To motivate why we might need different types of light sources, let us consider the behavior of light in various, ostensibly different forms, using three illustrative examples: the light emitted by a flashlight, a laser beam, and a single photon. These sources are inherently different, and are best described in different ways: the flashlight emits what is essentially an incoherent flux of electromagnetic (EM) energy, and its intensity is usually a sufficient description of this physical manifestation of light; the laser tends to emit a wave or wave-packet, which we describe by its EM field, including a well-defined phase in space and time, and often a polarization; finally, the single photon – quantum of the EM field – is represented as a Fock state within some Hilbert space.

Nevertheless, on their own, the light emitted from these sources, as different as it may be, tends to behave in a similar manner. It is only when we combine identical sources that different behaviors emerge. Consider a balanced beamsplitter, as illustrated in Fig. 1(a), through which

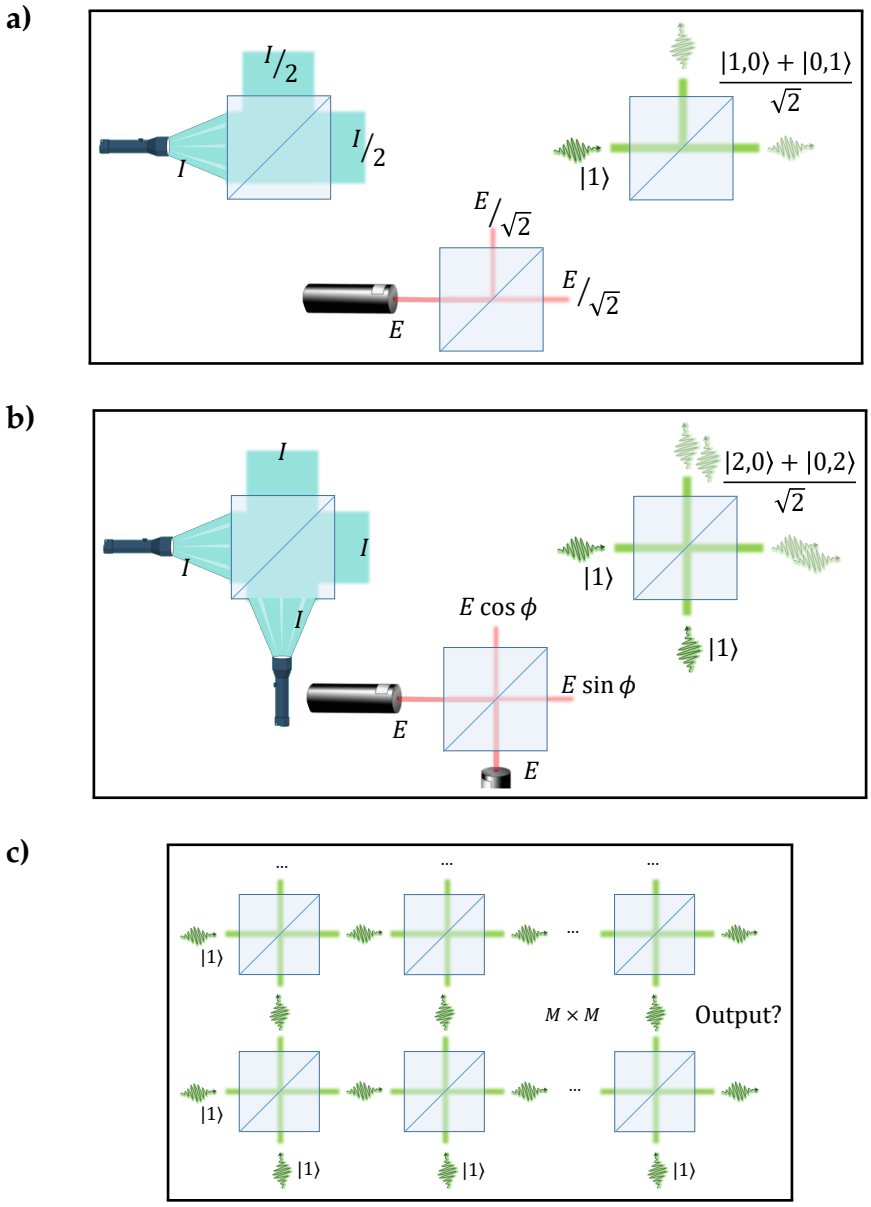

Figure 1: **Different behaviors of classical and non-classical light. a.** A flashlight beam, laser beam and photon represent different states, or physical manifestations, of light. These behave in a similar manner when propagating singly. E.g. when shining onto a beamsplitter, half the light goes through each of the two outputs of the beamsplitter, whether we prefer to think of it as an average intensity, field, or number of particles. **b.** The role of different types of interference is what makes the behavior of light unique. Two flashlights do not affect each other; two coherent laser beams will constructively and destructively interfere; two photons will bunch due to their probability-amplitude interference. **c.** What happens when we feed n photons through an $M \times M$ array of beamsplitters? Can we compute the output distribution of the photons? Is this generally solvable problem?

we shine either the flashlight, laser beam, or single photon. The beamsplitter acts on these three inputs in more or less the same way, sending (on average) half the light one way, half the other.

The interesting, or distinctive, behavior emerges when we use the beamsplitter to combine two copies of the same source, as illustrated in Fig.1(b), due to the underlying collective state of the photons involved. Two flashlights act independently: macroscopically the intensities simply add, and the two output ports of the beamsplitter emit the averaged powers. Not so for two mutually coherent lasers: the two light waves must destructively or constructively interfere, allowing uneven transmission to one side or the other depending on the relative phase. The single photon case also experiences interference, but instead in its probability amplitudes. This results in bunching: the photons travel together, always forming a pair (known as the Hong–Ou–Mandel effect). The state of the electromagnetic field at the outputs of the beamsplitter, being perfectly correlated, are also entangled.

As a thought experiment, we may try to extend or generalize this last scenario. Let us consider n photons sent through an $M \times M$ array of beamsplitters, as illustrated in Fig. 1(c). What is the state that comes out on the other side? This is a hard problem, closely related to fundamental questions in quantum field theory, namely the (many-body) algebras of bosons [2], developed midway through the last century. From a more modern perspective, however, interest in the nature, or "hardness," of this problem arose due to questions in computational complexity and quantum computing [3].

Quantum computing is based on the premise that entanglement and probability amplitude interference may be leveraged to improve the algorithmic complexity of a certain class of computational problems, including what are otherwise believed to be (classically) intractable problems. However, it involves the fine control of large ensembles of fragile quantum resources, further-

more, in a manner that must be able to scale as needed. This has been so far out of reach, which has prompted scientists to consider the possibilities in the near-term, and to find ways to verify whether quantum mechanics truly does bestow a practical "advantage" in the physical world. Therefore, in a paper wedding quantum optics to complexity theory, Aaronson et al. proved that the many-body functions describing these photon ensembles are classically intractable to approximate [4], and proposed the first *Boson sampling* protocol. This random sampling problem relies on the "natural computation" performed by entangled photons, which is impossible to reproduce by classical means. This was motivated [1] as a near-term way to provide some evidence as to whether we could indeed produce and manipulate quantum states at a large scale with high fidelity, as necessary for quantum computing, hinging on photonics being an accessible experimental platform.

This development spurred new interest in the field of optical quantum computing, especially as it related to building experimental realizations of the protocols described by Aaronson et al., or variations thereof, with gradually greater sophistication. This also served as a sort engineering testing-grounds: what technologies and which architectures are the best for producing these quantum states of light, and therefore eventually useful for the quantum sciences? *Best* here would be determined as a combination of three factors:

1. scalability – how large the state can be made, in terms of number of modes and photons;
2. programmability – the control of the quantum state and how many different states can be prepared;

[1] From a more fundamental perspective, it is also of physical interest to understand the limit to the complexity of the "tasks" that the universe can perform – especially as it relates to quantum mechanics. Related to the Extended Church–Turing thesis, we could imagine that the universe might have a complexity limit just as it has a speed limit [5].

3. and fidelity – how reliably the state can be prepared into precisely the one we want.

Developing the technologies necessary to unmistakably demonstrate Boson sampling is considered an intermediate step towards universal quantum computing using photonics. As Knill, Laflamme and Milburn showed (the KLM protocol), universal quantum computing is achievable with what amounts to a more general version of Boson sampling, with intermediate photon measurements and adaptive control of the remaining photons [6].

Within this larger context, our aim was to explore the ways in which light may be controlled experimentally and theoretically to reveal its quantum nature.

Chapter 1, which makes up the bulk of the work presented in this thesis, aimed to inspire a paradigm shift in the way experimental quantum optics is done. The publication presented a novel way to manipulate and measure vacuum squeezing, and broke records in the number of squeezed modes measured simultaneously by photon counting. The research started with the realization of three synergistic facts:

1. Optics is incredibly broadband: in principle, the terahertzes of bandwidth have an enormous capacity for encoding information optically. In addition, nonlinear processes – especially vacuum squeezing – naturally tend to be highly multimode, with many spectral degrees of freedom.

2. Different wavelengths of light present different advantages and disadvantages. This is a question of technology and materials. Namely, the lasers and nonlinear materials available, especially in the context vacuum squeezing, work best at near-infrared (NIR) wavelengths The best detectors, however, tend to be at visible wavelengths. Bridging this gap, allows the benefits of both: high-quality optical materials with strong nonlinearities; and efficient, low-noise photon-detection.

3. Nonlinear optics is the field that concerns the conversion of light between different wavelengths, and coherent, unitary, wave conversion results in what can be thought of as a frequency-domain beamsplitting. This beamsplitter can be controlled by the driving field (pump) and optical device design.

The first point is especially important from a quantum optics perspective, because frequency (photon energy) is arguably the most fundamental variable in nonlinear optics (closely related momentum is also important, but it is usually a bijective relationship in a waveguide). Spatial degrees of freedom can be eliminated by using single-mode waveguides. Temporal degrees of freedom can be eliminated by using temporally localized driving fields. But frequency remains somewhat of an experimental headache. There is a fun saying that in quantum mechanics, "anything that can happen, will happen." It unfortunately applies all-too-well in vacuum squeezing: when we rely on a spontaneous process to generate photons, we cannot dictate at which wavelengths they are created – this "uncertainty" can often span a spectrum of hundreds of THz or nm. This creates a distinguishability problem: the photons are no longer identical particles, and do not interfere as such. Indeed many experiments, despite careful engineering effort towards single-mode spectral behavior, suffer from subtle distinguishability effects [7]. Hence, our original thinking was not to fight this fact, but to embrace it, and take advantage of the hundreds of distinguishable photonic modes generated in conventional squeezing processes.

The second point is mainly due to the fact that vacuum squeezing is a parametric amplification process, hence involves down-conversion of light to half the driving field frequency. In addition, the driving field is usually red or NIR, as most nonlinear materials do not respond well to high intensity visible light, and especially not ultraviolet light. Related to this is the fact that a lot of the photonics technology we would like to use of sits at near-infrared wavelengths; it is no coincidence that the world's telecommunications infrastructure also operates at that end of

the spectrum. However, single-photon detection does not work well at those wavelengths: the quantum efficiency and noise are unacceptable, unless superconducting nanowire single photon detectors are used. Although gaining in popularity, probably driven by necessity, these – as the name implies – require single-Kelvin temperatures, and therefore interfacing optics with cryogenics. However, semiconductor devices are another technological pillar, and this includes camera sensors. Cameras are interesting from a scalability perspective because they are (mass-)produced with millions of individual detectors – pixels. In addition, the quantum efficiency tends to be very high, without incurring significant noise due to charge carriers. The production of high-quality single-photon-detecting cameras a few years prior to this project was fortuitous.

Nonlinear optics allows us to bridge the visible and NIR wavelengths, and – given our use of a frequency degree-of-freedom encoding – perform frequency-domain transformations. Energy conservation constrains the conversion, which makes it particularly challenging when compared to spatial or temporal transformations. Indeed, a monochromatic pump would perform an identity transformation across the visible-NIR. By using a broadband driving field (pump), we have access to a broader set of energies and are not limited to bijective transformations. Pulse shaping – controlling the phase and amplitude of the frequencies within the pump – changes the conversion process and hence the overall transformation. Therefore, instead of physically interacting with beamsplitters, phase-shifters, active delay lines, or other such devices, the quantum light can simply propagate while interacting with the classical driving field. The burden of programming and control falls onto the classical light, so that the quantum light might sustain less loss and decoherence.

This first work inspired follow-up ideas about controlling spectro-temporal degrees of freedom of light and new ways to generate squeezed light by using frequency conversion. This is presented

in Chapter 2. We sought to explore the power of frequency conversion as a tool for manipulating quantum light. In doing so, we realized that simultaneous frequency conversion and parametric amplification was a powerful combination. Not only can frequency conversion be used for broadband unitary transformations (moving pulses or states around in frequency and time) but it can be used to hybridize frequency modes. By bringing a state into a spectral superposition of two wavelengths, we can make a state interact with itself in ways that are not otherwise possible. This could potentially be applied to engineering single-mode squeezing, and creating optical "traps": where one weak light pulse is trapped within a larger light pulse. This work is incomplete and has yet to be published, but interesting enough to include even in a limited capacity.

Finally, Chapter 3 is a study of spatially-dependent broadband temporal operations in linear metasurfaces. Metasurfaces are two-dimensional devices composed of sub-wavelength elements or patterns. These can be designed to control the wavefront of incoming light, by imparting local, wavelength-dependent phase shifts, deforming the wavefront in unprecedented ways. The most notable motivation and application has been to replace bulky imaging lenses and objectives with slim, compact devices: metalenses. The topic of this Chapter is of a different flavor, and the work builds on the slow light and optical signal processing literature: fields which sought to determine the bandwidth limits of passive, time-invariant devices in performing temporal operations, namely time delays. These theories were applied to derive physical limits to the performance of wavefront shaping by metasurfaces. Specifically, we derive the bandwidth over which a metalens can have achromatic focusing.

Background

The following chapters and their appendices are mostly self-contained, so here we will briefly summarize some fundamentals of nonlinear and quantum optics not covered therein, as can be found in various textbooks on the subject, such as [8, 9]. Namely we will review the classical equations for nonlinear wave mixing (frequency conversion), and how to use them quantum-mechanically.

We start with Maxwell's wave equation in a dielectric, with no magnetic response:

$$\nabla^2 E = \frac{1}{c^2}\frac{\partial^2}{\partial t^2}\left(E + \frac{P}{\varepsilon_0}\right). \tag{1}$$

Outside the scope of nonlinear optics, the polarization term P is usually treated as linear, perhaps with some birefringence or anisotropy, or with an absorption or gain component. However, at high field intensities, the oscillatory electronic response in the material will eventually become anharmonic, and these distortions may cause nonlinear effects, known as wave mixing. We can model the polarization by expanding it as a series, with linear and nonlinear parts:

$$P_i = \varepsilon_0\Big(\underbrace{\chi^{(1)}_{ij}E_j}_{P_{\mathrm{L}}} + \underbrace{\chi^{(2)}_{ijk}E_jE_k + \chi^{(3)}_{ijkl}E_jE_kE_l + \ldots}_{P_{\mathrm{NL}}}\Big). \tag{2}$$

where the χ terms represent the susceptibilities. Although we only consider only local, instantaneous polarization terms, the Raman and Brillouin effects are well-known examples of third-order, time-dependent phenomena.

We then make a few assumptions that allow us to reduce the wave-mixing physics to a coupled-mode theory. First of all, we treat the nonlinear responses as a small perturbations to the total induced polarization. Second, we represent each frequency component of the field in terms of its

complex amplitude:

$$E = \sum_n E_n(r,t) \tag{3}$$

$$E_n(r,t) = \frac{1}{2}E_n(r)\mathrm{e}^{-i\omega_n t} + c.c. \tag{4}$$

and similarly with polarization:

$$P = \sum_n P_n^{(\mathrm{L})}(r,t) + P_n^{(\mathrm{NL})}(r,t). \tag{5}$$

This separation of variables reduces the wave equation to the Helmholtz equation, where we group field and polarization terms at the same frequency:

$$\begin{aligned} \nabla^2 E_n - \frac{1}{c^2}\frac{\partial^2}{\partial t^2}\left(E_n + \frac{P_n^{(\mathrm{L})}}{\varepsilon_0}\right) &= \frac{1}{\varepsilon_0 c^2}\frac{\partial^2 P_n^{(\mathrm{NL})}}{\partial t^2} \\ \nabla^2 E_n + \frac{\omega_n^2}{c^2}\varepsilon_n(\omega_n)E_n &= -\frac{\omega_n^2}{\varepsilon_0 c^2}P_n^{(\mathrm{NL})}. \end{aligned} \tag{6}$$

We can then substitute in the wavenumber $k_n^2 = \varepsilon_n(\omega_n)\omega_n^2/c^2$, by assuming a plane wave or guided mode,

$$\begin{aligned} E_n(r) &= A_n(z)\mathrm{e}^{ik_n z} \\ \left(\frac{d^2A}{dz^2} + 2ik\frac{dA}{dz} - k^2 A_n\right)\mathrm{e}^{ik_n z} + k_n^2 A_n \mathrm{e}^{ik_n z} &= -\frac{\omega_n^2}{\varepsilon_0 c^2}P_n^{(\mathrm{NL})} \\ \left(\frac{d^2A}{dz^2} + 2ik\frac{dA}{dz}\right)\mathrm{e}^{ik_n z} &= \end{aligned} \tag{7}$$

and perform the paraxial approximation to the Helmholtz equation, also known in this context as the slowly-varying envelope approximation:

$$\left|\frac{d^2A_n}{dz^2}\right| \ll \left|2k\frac{dA_n}{dz}\right| \rightarrow 2ik\frac{dA_n}{dz}\mathrm{e}^{ik_n z} \approx -\frac{\omega_n^2}{\varepsilon_0 c^2}P_n^{(\mathrm{NL})}. \tag{8}$$

Finally, P_{NL} is proportional to the products of these fields, and we must match terms appropriately according to frequency, to ensure energy conservation. For example, for a $\chi^{(2)}$ process we have:

$$P_n^{(\mathrm{NL})} \propto \sum_{\substack{i,j \\ \omega_i+\omega_j=\omega_n}} A_i A_j \mathrm{e}^{i(k_i+k_j)z} + \sum_{\substack{i,j \\ \omega_i-\omega_j=\omega_n}} A_i A_j^* \mathrm{e}^{i(k_i-k_j)z} \tag{9}$$

hence we obtain our coupled mode, or wave, equations:

$$\frac{dA_n}{dz} \propto i \sum_{\substack{i,j \\ \omega_i \pm \omega_j = \omega_n}} A_i A_j^{(*)} \mathrm{e}^{i(k_i \pm k_j - k_n)z} \tag{10}$$

$k_i \pm k_j - k_n = \Delta k$ is known as the phase mismatch, and must vanish for a nonlinear process to occur efficiently, i.e. without back-conversion. Therefore, it is often said that nonlinear wave-mixing processes must also conserve momentum.

In this thesis, we are most concerned with $\chi^{(2)}$ nonlinearities, as these allows the greatest control over wave mixing processes, and are the strongest nonlinear effects. Only non-centrosymmetric materials may have a finite second-order nonlinearity, as it requires a non-symmetric electronic potential. Hence, only certain classes of crystal possess this nonlinearity, but fortunately, in some materials this nonlinearity is associated with a ferroelectric effect – typically an atom in a crystal lattice with two possible locations. This allows us to flip the sign, or direction, of $\chi^{(2)}(z)$ by flipping the ferroelectric moment – or pole – at that location. This is used to spatially vary the sign of the nonlinearity and create ferroelectric gratings in the material, usually with a "poling" period of $2\pi/\Delta k$. This periodic nonlinearity adds the necessary momentum to eliminate the phase-mismatch and enable efficient wave conversion.

Finally, we need to introduce quantum mechanics to the wave mixing process, which so far has been described in a purely classical manner. It is first instructive to understand electromagnetic waves within the formalism of quantum harmonic oscillators. Here we give a brief, non-rigorous derivation. The Hamiltonian in linear electromagnetism is:

$$H = \frac{1}{2} \int d^3r \left(\frac{D^2}{\varepsilon} + \frac{B^2}{\mu} \right) \tag{11}$$

$$= \int d^3r \frac{|\tilde{D}|^2}{\varepsilon}. \tag{12}$$

We denote D, B as real displacement and magnetic fields, and $\tilde{D}$ as a complex field representation.

In the latter equation we use that the a propagating wave has equal average magnetic and electric energy density. (In the context of quantum nonlinear optics quantization with D is considered more appropriate than E.)

Consider plane-wave solutions with polarization $\hat{\epsilon}$ and wavevector $\vec{k}$:

$$D = \sum_{\vec{k},\hat{\epsilon}} A_{\vec{k},\hat{\epsilon}} \hat{\epsilon} D_{\vec{k},\hat{\epsilon}} \sin\left(\vec{k}\cdot r - \omega t\right) \tag{13}$$

$$B = \sum_{\vec{k},\hat{\epsilon}} A_{\vec{k},\hat{\epsilon}} \frac{\vec{k}\times\hat{\epsilon}}{\varepsilon c|k|} D_{\vec{k},\hat{\epsilon}} \cos\left(\vec{k}\cdot r - \omega t\right) \tag{14}$$

To perform quantization, we need to identify the coordinates of the system and their conjugate momenta, denoted here as q and p. In this case we can essentially pick the electric field components of the plane waves as the coordinates and the magnetic field components as the momenta. (In a rigorous treatment, the generalized coordinates should be the components of the vector potential and their conjugate momenta.) Normalizable wavepackets are superpositions of these plane wave harmonic oscillators.

Thus the Hamiltonian of the quantized variables becomes

$$H = \frac{1}{2}\sum_{\vec{k},\hat{\epsilon}} \int d^3r \left(\hat{q}^2_{\vec{k},\hat{\epsilon}} + \hat{p}^2_{\vec{k},\hat{\epsilon}}\right) \tag{15}$$

$$= \sum_{\vec{k},\hat{\epsilon}} \int d^3r \hbar\omega \left(\hat{a}^\dagger_{\vec{k},\hat{\epsilon}} \hat{a}_{\vec{k},\hat{\epsilon}} + \frac{1}{2}\right), \tag{16}$$

where we can now quantize the modes by treating them as an infinite set of independent harmonic oscillators, with corresponding creation and annihilation operators. We can treat the latter as the quantized operators of the complex field variable:

$$\tilde{D} = A\mathrm{e}^{i(kz-\omega t)} \rightarrow \sqrt{\hbar\omega}\mathrm{e}^{i(kz-\omega t)}\hat{a}. \tag{17}$$

This relation is exact if the field modes are normalized such that A has units of $\sqrt{\hbar\omega}$.

We can now introduce nonlinearities, as a perturbation to the linear Hamiltonian. The energy density is given by the polarization-field product, and, for example, if we consider the second-order susceptibility term $\chi^{(2)}_{ijk}$:

$$H_{\mathrm{NL}} = \int d^3r P_{\mathrm{NL}} \cdot \frac{D}{\varepsilon} \propto \sum_{i,j,k} \int d^3r \tilde{D}_i \tilde{D}_j^{(*)} \tilde{D}_k^{(*)} + c.c. + \dots \tag{18}$$

$$\rightarrow \sum_{i,j,k} \int d^3r \hat{a}_i \hat{a}_j^{(\dagger)} \hat{a}_k^{(\dagger)} + c.c. + \dots \tag{19}$$

The takeaway is that the higher-order susceptibilities act to create and annihilate photons, converting photons from some modes to others essentially by combination and splitting.

Lastly, we need to incorporate the quantized fields into the coupled wave equations. Procedurally, we can use Eq. 17 as-is, by simply performing the substitution in Eq. 10. We thus obtain:

$$\frac{d}{dz}\hat{a}_n \propto i \sum_{\substack{i,j \\ \omega_i \pm \omega_j = \omega_n}} \hat{a}_i \hat{a}_j^{(\dagger)} \mathrm{e}^{i(k_i \pm k_j - k_n)z}. \tag{20}$$

To recover the classical picture, we can interpret the above equation as the evolution of the expectation value of the field operators:

$$\frac{d}{dz}\langle \hat{a}_n(z) \rangle \propto i \sum_{\substack{i,j \\ \omega_i \pm \omega_j = \omega_n}} \langle \hat{a}_i(z) \rangle \left\langle \hat{a}_j^{(\dagger)}(z) \right\rangle \mathrm{e}^{i(k_i \pm k_j - k_n)z}. \tag{21}$$

Indeed, in the context of nonlinear optics, one field must be large enough to induce a nonlinearity. This pump or driving field is typically treated as a classical:

$$\frac{d}{dz}\hat{a}_n(z) \propto i \sum_{\substack{i,j \\ \pm\omega_i \pm \omega_j = \omega_n}} A_i^{(*)}(z) \hat{a}_j^{(\dagger)}(z) \mathrm{e}^{i(\pm k_i \pm k_j - k_n)z}. \tag{22}$$

This is the regime of Gaussian quantum optics, where the equations are linear in the quantum fields (in contrast to the case where a few photons could induce a nonlinearity).

Quantum mechanically, however, we are implicitly including a pair of evolution operators

C, S:

$$\hat{a}_i(z) = \sum_j C_{ij}(z)\hat{a}_j(0) + S_{ij}(z)\hat{a}_j^\dagger(0), \tag{23}$$

(a Bogoliubov transformation) whose own equations of motion are:

$$\frac{dC_{nl}}{dz} \propto i \sum_{\substack{i,j \\ \pm\omega_i \pm \omega_j = \omega_n}} A_i^{(*)} \mathrm{e}^{i(\pm k_i + k_j - k_n)z} \begin{cases} C_{jl}, & \hat{a}_j \\ S_{jl}^*, & \hat{a}_j^\dagger \end{cases} \tag{24}$$

$$\frac{dS_{nl}}{dz} \propto i \sum_{\substack{i,j \\ \pm\omega_i \pm \omega_j = \omega_n}} A_i^{(*)} \mathrm{e}^{i(\pm k_i - k_j - k_n)z} \begin{cases} S_{jl}, & \hat{a}_j \\ C_{jl}^*, & \hat{a}_j^\dagger \end{cases} \tag{25}$$

which generalizes to the Heisenberg and density-matrix pictures.

Appendix A in Chapter 1 expands on what was presented in this section to cover the fundamentals of multimode Gaussian quantum optics.

CHAPTER 1

HIGHLY MULTIMODE VISIBLE SQUEEZED LIGHT WITH PROGRAMMABLE SPECTRAL CORRELATIONS THROUGH BROADBAND UP-CONVERSION

This work was done together with Logan G. Wright, Shi-Yuan Ma, Tianyu Wang, Benjamin K. Malia, Tatsuhiro Onodera, and Peter L. McMahon [10].

Multimode squeezed states of light have been proposed as a resource for achieving quantum advantage in computing and sensing. Recent experiments that demonstrate multimode Gaussian states to this end have most commonly opted for spatial or temporal modes, whereas a complete system based on frequency modes has yet to be realized. Instead, we show how to use the frequency modes simultaneously squeezed in a conventional, single-spatial-mode, optical parametric amplifier when pumped by ultrashort pulses. Specifically, we show how adiabatic frequency conversion can be used not only to convert the quantum state from infrared to visible wavelengths, but to concurrently manipulate the joint spectrum. This near unity-efficiency quantum frequency conversion, over a bandwidth >45 THz and, to our knowledge, the broadest to date, allows us to measure the state with an electron-multiplying CCD (EMCCD) camera-based spectrometer, at non-cryogenic temperatures. We demonstrate the squeezing of >400 frequency modes, with a mean of approximately 700 visible photons per shot. Our work shows how many-mode quantum states of light can be generated, manipulated, and measured with efficient use of hardware resources – in our case, using one pulsed laser, two nonlinear crystals, and one camera. This ability to produce, with modest hardware resources, large multimode squeezed states with partial programmability motivates the use of frequency encoding for photonics-based quantum information processing.

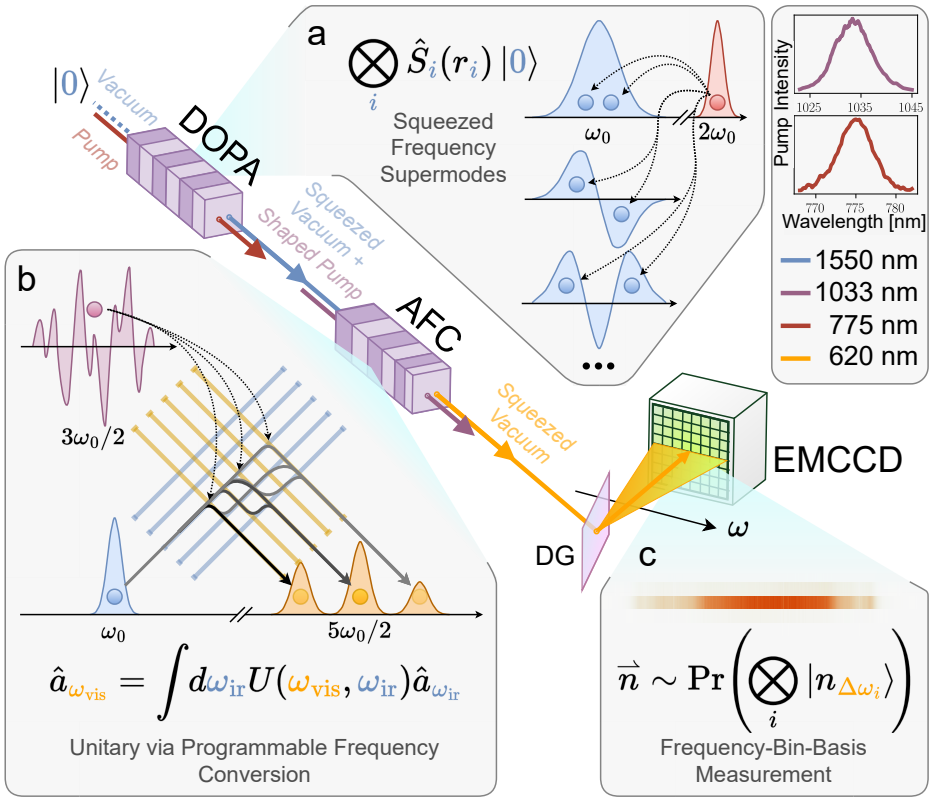

Figure 1.1: **Frequency domain, multimode, visible squeezed state preparation and detection. a.** Highly multimode squeezed vacuum is generated in the degenerate optical parametric amplifier (DOPA), at near infrared wavelengths. The squeezed modes occupy orthogonal frequency spectra. This may be represented by a set of squeezing operators $\hat{S}_i$ acting the vacuum state $|0\rangle$. Each operator squeezes a distinct frequency mode with some squeezing parameter r_i. The squeezing occurs around a central frequency ω_0 equal to half the pump central frequency $2\omega_0$. Concretely, these correspond to the wavelengths 1550 nm and 775 nm, respectively. **b.** Adiabatic frequency conversion (AFC) efficiently converts the squeezed light to visible wavelengths. The pump, a broadband pulse centered at 1033 nm ($3\omega_0/2$), combines with the broadband 1550 nm signal to yield 620 nm ($5\omega_0/2$) light. This transformation between the two sets of frequencies can be changed by varying the spectro-temporal profile of the pump. This operation may be represented as a linear unitary transformation U acting on the infrared and visible fields, represented by the operators $\hat{a}_{\omega_{\text{ir}}}$ and $\hat{a}_{\omega_{\text{vis}}}$. **c.** The final state, incident on a diffraction grating (DG), is split into frequency modes, and frequency-resolved photon counting is performed with an EMCCD camera. Each measurement yields some photon-number sequence, or vector, $\vec{n}$, whose probability distribution depends on the state (determined by $\hat{S}_i$ and U). The camera measures the spectrum in a discrete manner, as the pixels capture the photons within some frequency "bins," denoted $\Delta\omega_i$. Hence, the state's overlap with these bin-basis Fock states, $|n_{\Delta\omega_i}\rangle$, determines the probability distribution.

The generation, control, and measurement of entangled multimode Gaussian states of light are crucial elements of continuous-variable (CV) quantum information processing [11–14]. Most quantum technologies based on multimode quantum optics benefit from being able to use as many modes as possible. As an example, a Gaussian boson sampler (GBS) [15, 16] is a special-purpose quantum computer that can – at least in the ideal case – perform certain calculations that are believed to be intractable on a classical computer when the number of modes and number of photons in the GBS are sufficiently large [16, 17]. The recent demonstration of Gaussian boson sampling in the regime of quantum computational supremacy, with tens to hundreds of squeezed modes and detected photons per shot [18–21], was a milestone in the development of CV-based quantum systems that was achieved because of the success in pushing to large numbers of modes and photons. A GBS executes a sequence of three steps, which are common to many CV quantum-information-processing protocols: (1) generate squeezed states, (2) apply a unitary transformation to entangle them, and (3) measure the final state (by photon counting).

Optics gives us the choice of several possible degrees of freedom within which to encode information – most importantly: space, time and frequency (or any combination thereof). While large-scale GBS experiments have been realized using space [18–20] and time [21] encodings, the frequency domain remains to be explored. Frequency encoding offers important potential advantages over space or time encoding for both the generation and the manipulation (unitary control) of multimode squeezed light: reduced hardware resources and complexity, and reduced loss. The extremely broad bandwidth of light enables frequency-encoded systems to operate on many frequency modes in a compact system [22–28]. Many demonstrations of large-scale multimode squeezing, for example, use the frequency domain, e.g., in broadband frequency combs [26, 27, 29–41]. Linear unitary operations in the frequency domain, i.e., acting on the frequency modes, can be implemented in a hardware-efficient way, operating on all frequency modes in par-

allel [42, 43]. One approach is to use one or more electro-optic modulators [42–46] (although there are limitations on the unitary from the driving microwave bandwidth being $\lesssim$100 GHz); another is to use nonlinear wave mixing to convert photons in each frequency mode to photons in a combination of other frequency modes [47]. Unitaries based on nonlinear wave mixing mediated by a classical field, such as four-wave mixing [48], provide a route to realizing programmable unitaries that can operate over wide bandwidths, in compact hardware with low loss. The programming of the unitary can be done by shaping the classical field(s) used to control the wave mixing of the modes containing quantum light, and the wave mixing can be implemented compactly in a single-spatial-mode waveguide. However, a programmable, frequency-domain unitary working over optical ($>$1 THz) bandwidths for quantum light has yet to be realized at even moderate scale (more than 2 modes [48]).

The final step, state measurement by photon counting, is a challenge for many multimode architectures. Since the preferred nonlinear optical materials for generating squeezed vacuum work best at longer wavelengths, squeezing at wavelengths centered near 1550 nm is typical [18–21, 25–36, 41], also in part due to the convenience of being able to use optical components from telecommunications technologies. However, good (high quantum-efficiency, low dark-count) single-photon detectors at 1550 nm, namely superconducting nanowire detectors [49, 50], are very expensive and require cryogenic cooling. Silicon-based camera sensor technologies – both charge-coupled device (CCD) and complementary metal–oxide–semiconductor (CMOS) detectors – are well-established, comparatively inexpensive and compact, and each camera comprises 10^5–10^6 individual pixels, i.e., detectors. Cameras capable of detecting single photons with low noise have recently become available, and there is a growing literature of quantum-optics and sensing experiments that were performed with visible wavelengths and these cameras [51–56]. Electron-multiplying CCD (EMCCD) cameras are arguably the current state-of-the-art, and low-noise CMOS photon-number-

resolving cameras are also a promising tool within this domain [57, 58].

Here, we demonstrate how to use frequency conversion [59] to enable the use of these visible-light cameras in combination with techniques for strong squeezing possible at longer wavelengths. In addition, our demonstration is an improvement over existing methods of quantum frequency conversion: previous demonstrations are limited to either modest bandwidths or efficiencies [60–66]. However, adiabatic frequency conversion (AFC) essentially eliminates this trade-off [67, 68]. We show how this method allows us to obtain robust, efficient and broadband conversion over >45 THz (1390–1750 to 590–650 nm) and near-unity efficiency. Furthermore, it allows unitary control of the multimode entanglement (with, in principle, no additional loss) by manipulation of the complex profile of the broadband pump used to drive the conversion. This architecture provides the best of both worlds: squeezing at telecommunications wavelengths, and photon detection at visible wavelengths. We will show that we are able to generate strong squeezing in over 400 frequency supermodes, resulting in states having a measured mean photon number of nearly 700. By using AFC to efficiently convert the squeezed light to visible wavelengths, and using the highly parallel photon counting made possible by a modern EMCCD, we can directly measure these states. We will also show that we can control the entanglement between different modes by using different spectrally shaped classical fields as the pump of the AFC process, resulting in different measured correlations between photon detections across the frequency modes.

Results

The experimental setup is illustrated in Fig. 1.1; an overview is as follows. We use a waveguided degenerate optical parametric amplifier (DOPA) pumped with a pulsed laser: this pro-

vides squeezing in a single spatial mode and over many frequency modes (known as the "supermodes"). An adiabatic frequency conversion (AFC) crystal subsequently converts this near-infrared squeezed light to the visible. The temporal profile of the AFC pump pulse is shaped, which controls the conversion process – the linear transformation between infrared and visible light frequencies. Finally we detect the visible squeezed light with an electron-multiplying CCD (EMCCD) camera, serving as an array of high-quality photodetectors.

In the following section, we present characterizations of each of these stages. We first measure the properties of the squeezed light in the infrared, directly out of the DOPA. Our characterizations enable us to measure the bandwidth of the squeezed light, estimate the number of modes, and verify squeezing. We then demonstrate efficient conversion using AFC. In addition, with the camera, we are able to observe spectral photon-number correlations throughout the whole bandwidth at high resolution. With this ability, we generate qualitatively different joint spectra as a proof of concept of frequency-domain unitary transformations by pulse shaping. Finally, we discuss detection and the photon numbers generated by this architecture. Refer to the Methods section for details on the DOPA, AFC, pulse shaper, the photon-counting spectrometer, as well as specific experiments.

Highly multimode squeezing in the frequency domain

We begin by studying the degenerate optical parametric amplification (DOPA) process, and looking for behavior consistent with highly multimode squeezing. Three experiments were performed to verify numerical predictions: a spectrum measurement, a parametric gain measurement and a coincidence detection measurement. The purpose of the first is to verify that the bandwidth is indeed as broad as predicted. The second is to infer the number of modes, based on how the out-

put energy scales with pump energy. The third is to verify that this light is made up of squeezed states, through photon statistics.

The DOPA was first simulated, and the photon-number covariance is plotted in Fig. 1.2a, which has a notable "X" shape. The anti-diagonal is due to the non-classical frequency correlations of entangled photons (the joint spectral intensity, or "entanglement correlations") and energy conservation dictates its shape: down-converted photon pair energies must add up to the pump photon energy. The diagonal represents the photon-number variance, and the correlations are classical ("thermal correlations," as these statistics have the same properties as those of thermal states [69]): this has a finite width, given by the phase-matching function of the OPA (typically a sinc function for periodic poling). The Bloch–Messiah decomposition helps us interpret how the

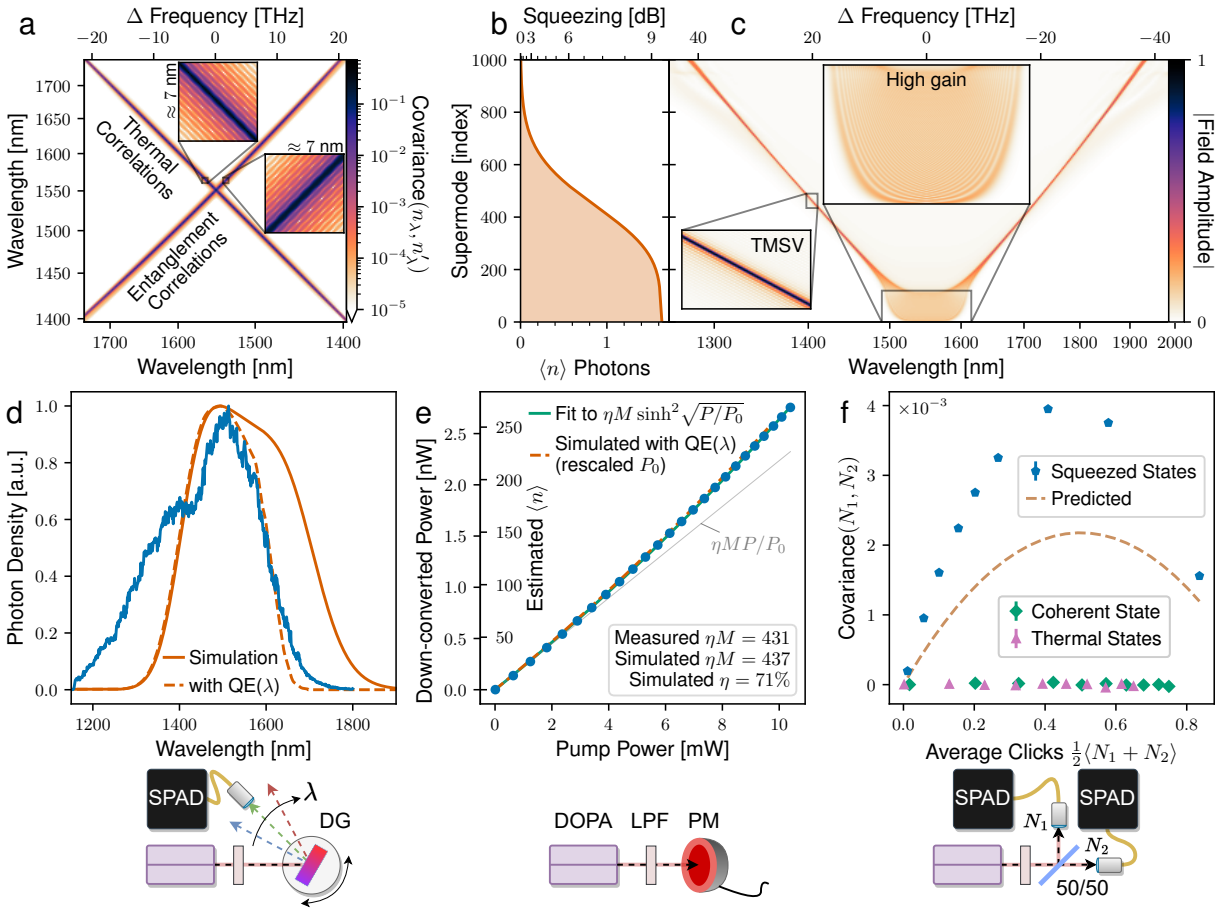

Figure 1.2: **Frequency-multimode squeezing in a lithium niobate waveguide optical parametric amplifier. a.** Simulated photon-number covariance matrix of the state produced in the degenerate optical parametric amplifier (DOPA). This is made up of classical "thermal" correlations (due to photon-number variance) and non-classical entanglement correlations. **b** and **c** show the decomposition of the simulated state into single-mode squeezed states, referred to as the supermodes. The plots share the vertical axis, which indexes these modes. **b.** Simulated average photon number ($\langle n \rangle$) and squeezing values of the first 1000 supermodes. **c.** Simulated supermode basis of the DOPA. Each row represents a mode and its spectrum is represented by the colormap. The high gain supermodes are approximately Hermite–Gauss functions while the weaker supermodes resemble two-mode squeezed vacuum (TMSV) states with two distinct frequency peaks. For **a-c**, the pump power is approximately equivalent to the highest used in the experiment. **d.** Measurement of the DOPA output spectrum and comparison to simulation. As the detector quantum efficiency (QE) vanishes at longer wavelengths, the simulation spectrum is also plotted multiplied by the nominal relative QE for comparison. **e.** Parametric gain of the DOPA, fit to the number of modes, and comparison to simulation. The photon number $\langle n \rangle$ is obtained by dividing the average power measurement by the repetition rate and the photon energy at the central wavelength. In the fit: M represents the number of modes; η the detection efficiency; P the pump power; P_0 the fitted scaling factor. **f.** Coincidence detection, comparing squeezed light, attenuated laser light (coherent) and broadband incandescent lamp (thermal). The prediction model is derived in Appendix C. Error bars represent standard error. Sketches of the experimental setups corresponding to **c–e** are shown below their respective plots. The DOPA output is measured with either a single-photon avalanche diode (SPAD) or a power meter (PM), after isolating the signal with a long-pass filter (LPF).

DOPA generates squeezing [70, 71], by reducing the output to a set of supermodes and their corresponding squeezing or anti-squeezing values. These are shown in Fig. 1.2b and c. For a 4 cm LN waveguide, and 775 nm 200 fs pulse pump, we predict $\sim$600 supermodes with substantial average photon numbers, spanning over 50 THz, or over 400 nm. The weakly squeezed supermodes (indices above 200) resemble two-mode squeezed vacuum (TSMV) states, occupying two sinc peaks on opposite sides of the central wavelength. The highly squeezed supermodes (indices below 200) appear to approximately be the typical Hermite–Gauss functions [70]. The supermodes are not constant with respect to the pump power, and tend to transition from TMSV to Hermite–Gauss as the parametric gain increases.

The spectrum measurement, whose outcome is shown in Fig. 1.2d, confirms that the spectrum is broad, spanning hundreds of nanometers. The spectrum could not be measured past about 1700 nm due to the detector response cut-off. The spectrum may be thought of as the incoherent sum of the supermodes, scaled by average photon number.

The parametric gain experiment (Fig. 1.2e) measures the output power of the DOPA at varying pump powers. The number of down-converted photons scales linearly with the number of supermodes M and the detection efficiency η, while each mode responds nonlinearly, containing on average $\langle n \rangle = \sinh^2 \sqrt{P/P_0}$ photons, for pump power P and scaling factor P_0. We may estimate the number of modes by fitting to $\eta M \sinh^2 \sqrt{P/P_0}$, which assumes equally squeezed modes (not truly the case, as shown in Fig. 1.2b, hence this is a lower bound). From this measurement we infer the presence of at least $M \geq \eta M = 431$ squeezed modes – on the order of 650 squeezed modes accounting for average detector responsivity, $\eta \approx 71\%$. In order to achieve a sufficently high – measurable – average output power, this experiment requires different operating conditions (a higher repetition rate pump laser), and we estimate that we would measure a slightly lower number of modes, 386 (465 corrected), under the usual conditions (Appendix I).

The coincidence experiment (inspired by Ref. [72]) is shown in Fig. 1.2f. The DOPA output beam is evenly split and the photon-number covariance between the two beams is measured. The coincidences depend on the photon statistics of the state, and at low photon numbers, only the coincidence rate of highly-multimode squeezed light is expected to scale linearly with respect to the average photon number. We performed coincidence detection with the DOPA output, attenuated 1550 nm laser light, and broadband incandescent lamp light; indeed only the former was nonzero.

These three experiments verify our predictions that the DOPA is a source of highly multimode squeezed light, spanning hundreds of frequency modes. A more thorough discussion of these re-

sults, including explanations of the experiment-theory discrepancies, is presented in the Methods.

Adiabatic frequency conversion (AFC) of squeezed light

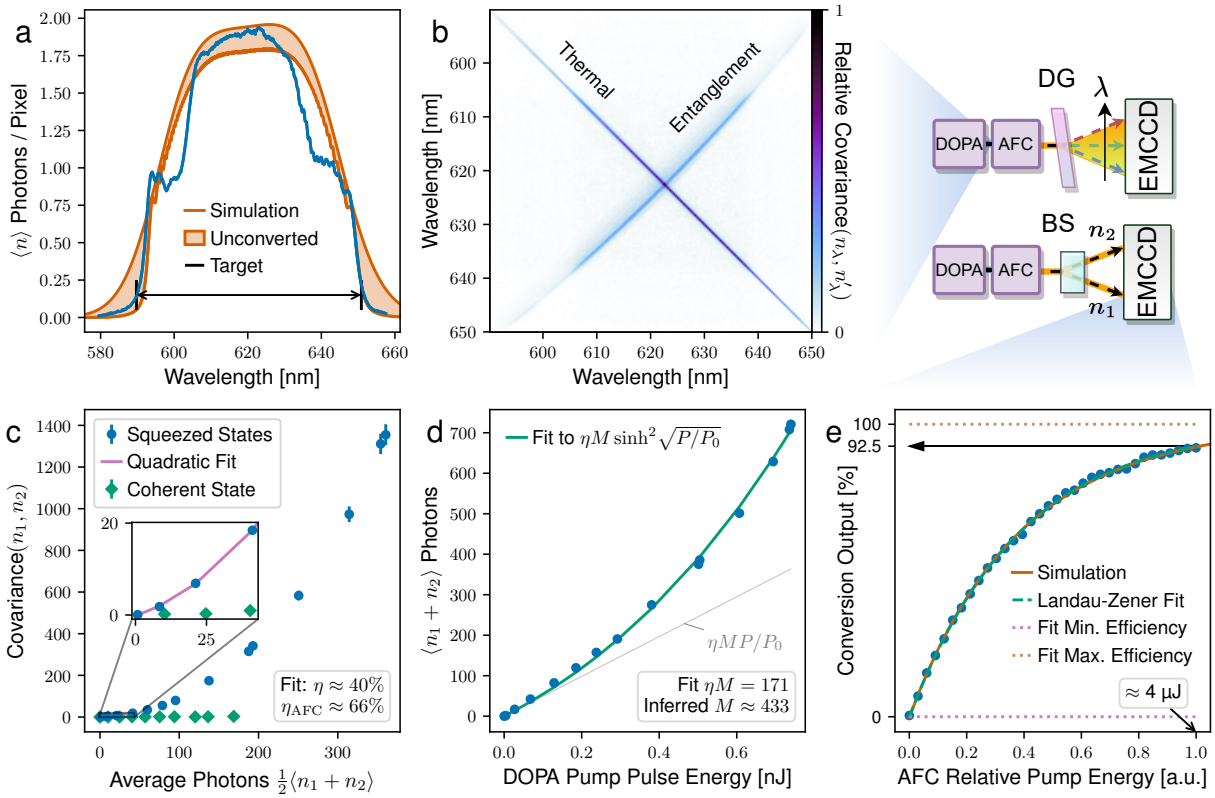

Figure 1.3: **Broadband, adiabatic frequency conversion (AFC) of squeezed light.** Experiments corresponding to plots **a** and **b** use a diffraction grating (DG) to use the EMCCD camera as a spectrometer. Experiments corresponding to plots **c–e** use a Wollaston prism configured as a 50:50 beamsplitter (BS). **a.** Converted spectrum measurement. This is compared to simulation under similar conditions and with 92% conversion within the conversion bandwidth. The shading in the simulation curve indicates the unconverted energy, to show that the conversion profile should be approximately flat within the target bandwidth. **b.** Measured, wavelength-resolved photon-number covariance matrix. The diagonal and anti-diagonal features can be recognized as the thermal (classical) and entanglement (non-classical) correlations. **c.** Coincidence detection after conversion. This experiment measures the transmission of the state (the effective fidelity or purity) as 40%. Error bars represent standard error. **d.** Parametric gain measured after conversion. The fit to this curve estimates the number of squeezed modes present in the converted state as 433, accounting for loss. **e.** Conversion as a function of pump power. A fit to the saturation curve estimates the conversion efficiency as 92.5%.

The next part of the experiment involves frequency conversion of the squeezed light. The infrared squeezed light, centered around 1550 nm, is up-converted with a pulsed 1033 nm laser, to a central wavelength of 620 nm, by sum frequency generation. This ultra-broadband nonlinear process is possible through AFC [67, 68], which acts as a unitary transformation in the frequency domain, and most importantly allows us to measure highly squeezed light with a sensitive, silicon-based camera. (See Appendix G for the crystal quasi-phase-matching design used in this experiment.)

In this section we demonstrate frequency conversion of squeezed light, show that it remains squeezed and measure the overall system fidelity, and provide estimates of the conversion efficiency and the number of converted modes. To this end, two experiments are presented in this section: one based on our visible light, single photon spectrometer (Fig. 1.3a-b); and one based on two-mode coincidence detection (Fig. 1.3c-d). The spectrometer uses a diffraction grating to separate the squeezed light into its wavelength components, which are imaged onto the EMCCD camera. The coincidence experiment also uses the camera, but a with prism, functioning as a 50:50 beamsplitter, replacing the grating. The two beams are imaged onto the camera, which emulates two detectors via two small regions of interest on the CCD.

The spectrum measured with the EMCCD camera visible light spectrometer is shown in Fig. 1.3a. The converted spectrum matches the designed conversion band. The shoulders in the spectrum (roughly between 590–600 and 640–650 nm), which differ from the simulation, are consistent with Fig. 1.2c (around 1400 nm): these features are from the original spectrum, not the conversion. The intensity implies that, on average, the most brightly-illuminated pixels receive almost 2 photons per pulse.

The photon-number covariance matrix is shown in Fig. 1.3b. Shot-by-shot intensities are ob-

tained by triggering the camera to capture individual pulses. The camera is used in "analog" mode (not thresholded) due to the high photon numbers per pixel (see Appendix B). For this experiment, the AFC is pumped in such a way as to maximize the conversion and to perform a transformation as close as possible to the identity, although the pump bandwidth causes some broadening (see Appendix G; an identity would require a monochromatic pump). The photon covariance matrix has the "X" shape we expect from Fig. 1.2a, with both classical and non-classical correlations.

The results of the coincidence experiment, similar to the one presented in the previous section, are shown in Fig. 1.3c. We can now use this experiment to measure the effective fidelity purity or of the state: where the photon statistics lie between those of pure squeezed vacuum and thermal noise, as parametrized by an effective loss or transmission. For few photons in each supermode, $\langle n \rangle \ll 1$, we expect linear scaling; at intermediate photon numbers, where $\langle n \rangle = \sinh^2 \sqrt{P/P_0} \approx P/P_0$, we expect the covariance to scale quadratically; and at greater photon number we cannot predict the scaling without precise knowledge of the supermodes (see Appendix C). In the first two cases, the coefficient of the linear component gives us an estimate of the overall transmission (a weighted average over all modes). Hence, we perform a quadratic fit to the lowest photon number portion of the data. The fit implies a 40% overall effective transmission for all the modes.

The same data is used for Fig. 1.3d, to quantify the parametric gain. By assuming the 40% overall (effective) transmission, the scaling implies the presence of over 430 squeezed modes. Some parasitic second harmonic generation is observed in the DOPA at higher pump energies, which could reduce the pump energy available for squeezing and possibly cause this value to be slightly underestimated.

The conversion as a function of AFC pump power is used as an estimate of the conversion efficiency, which is shown in Fig. 1.3e. Conversion efficiency (saturation) is described by the Landau–

Zener formula: unconverted signal follows an exponential decay with respect to the pump power. The fit implies 92.5% conversion; this is a reasonable upper-bound estimate on the conversion efficiency. We have been careful to make the pump beam much larger than the signal, and have verified that it has minimal spatial chirp, as a fit to the Landau–Zener formula may overestimate the efficiency if there is substantial mismatch in the spatio-temporal overlap in the pump and signal. Nonetheless, we can obtain a lower bound estimate from the 40% total fidelity or effective transmission. By measuring the transmission of each optical element in the squeezed light beam path and taking into account the camera quantum efficiency (QE), we estimate the end-to-end passive optical transmission to be at least 60% (excluding AFC). This bounds the conversion efficiency from below to at least $\sim$66%. This is a fairly loose bound, as the fidelity figure includes non-loss decoherence (e.g. detector excess noise; weakly converted photons at wavelengths outside the conversion band) and the combined linear loss in the beam path probably exceeds 40%. Finally, we point out that the conversion efficiency is pump-power limited, meaning that achieving close to 100% over these bandwidths is realistic without requiring phase-locking.

Upconversion as a frequency-domain unitary transformation

Most quantum sensing or computing protocols require unitary operations to be performed on the overall state, because each application requires some specific entanglement structure. Here we demonstrate how the covariance matrix can be transformed by implementing frequency unitaries through the broadband sum frequency generation process. The unitary is applied during the conversion; shaping the AFC pump pulse affects the nonlinear dynamics, changing which wavelengths convert to which. This means that, within certain constraints, we can program the pulse to achieve a desired transformation.

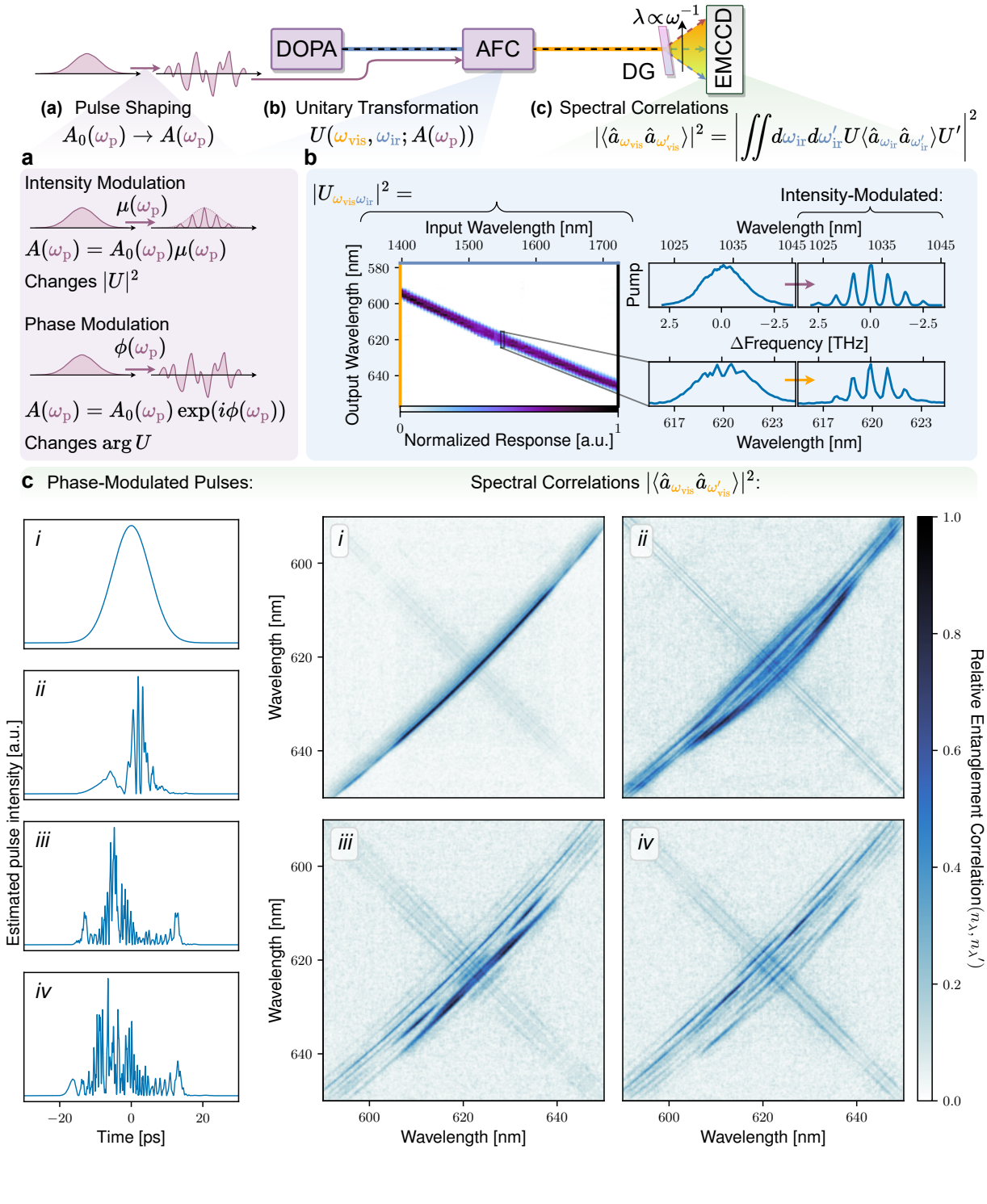
DOPA
AFC
DG
EMCCD
$\lambda \propto \omega^{-1}$
(a) Pulse Shaping
$A_0(\omega_p) \rightarrow A(\omega_p)$
(b) Unitary Transformation
$U(\omega_{vis}, \omega_{ir}; A(\omega_p))$
(c) Spectral Correlations
$|\langle \hat{a}_{\omega_{vis}} \hat{a}_{\omega'_{vis}} \rangle|^2 = \left| \iint d\omega_{ir} d\omega'_{ir} U \langle \hat{a}_{\omega_{ir}} \hat{a}_{\omega'_{ir}} \rangle U' \right|^2$
a
Intensity Modulation
$\mu(\omega_p)$
$A(\omega_p) = A_0(\omega_p)\mu(\omega_p)$
Changes $|U|^2$
Phase Modulation
$\phi(\omega_p)$
$A(\omega_p) = A_0(\omega_p)\exp(i\phi(\omega_p))$
Changes $\arg U$
b
$|U_{\omega_{vis}\omega_{ir}}|^2 =$
Input Wavelength [nm]
Output Wavelength [nm]
Normalized Response [a.u.]
Intensity-Modulated:
Wavelength [nm]
Pump
ΔFrequency [THz]
c Phase-Modulated Pulses:
Spectral Correlations $|\langle \hat{a}_{\omega_{vis}} \hat{a}_{\omega'_{vis}} \rangle|^2$:
Estimated pulse intensity [a.u.]
Time [ps]
Wavelength [nm]
Relative Entanglement Correlation $(n_\lambda, n_{\lambda'})$

Figure 1.4: **Preparing the joint spectrum via frequency conversion.** By pulse shaping the AFC pump $A(\omega_p)$, we can modify the linear unitary transformation U performed by the AFC process, hence the state and the measured spectral photon-number correlations. The pump spectral intensity and phase both play a role in the transformation. **a.** Pulse shaping involves two operations: intensity and phase modulation. The former ($\mu(\omega_p)$) changes the spectral intensity of the pump, which in turn mainly affects the magnitude of elements of U, and the latter ($\phi(\omega_p)$) changes the spectral phase of the pump, which mainly affects the complex phase of the elements of U. **b.** The phase-averaged linear transformation performed by the AFC. The rows of the unitary strongly resemble the pump spectrum, as shown in the subplots: the first pair shows how it compares to the original spectrum, and the second is an example of how it changes given an intensity-modulated pump. The frequency-difference axis is shared among the pump and unitary-row subplots. **c.** These plots show how a phase-modulated pump affects the conversion process and produces more complicated correlation structure. Example spectral intensity correlations are plotted on the right, and the corresponding (inferred) pump intensity profiles on the left. Specifically, we plot the entanglement contribution to photon correlation matrices (correlation matrices with thermal-like components subtracted). The first shows the same data in Fig. 1.3b, for reference, with no pulse shaping. The next three are the result of random pulse shaping. The corresponding pump intensities, plotted on the right, are not measured directly, but estimated based on the phase modulation applied and the pulse shaper calibration.

Intuitively, the relative phase of a pump frequency affects the phase of a signal it converts, thereby constructive and destructive interference may promote or suppress the conversion of a signal from one frequency to another, effectively forming a frequency-domain interferometer network. This is illustrated in Fig. 1.4a-b. We discuss this further in Appendix D.

Some examples of this process and how it influences the covariance matrix are shown in Fig. 1.4c. Phase modulations are applied with the pulse shaper, on top of a fixed quadratic phase (chirp) to guarantee a certain pump pulse duration. The predicted pulse shapes (inferred from the applied phase modulation) are shown for each example. For clarity, we show the correlation rather than covariance matrices, and we subtract a fit to the thermal (classical) part in order to show only the entanglement contribution (the joint spectrum). For reference, Fig. 1.4a is derived from the same data as Fig. 1.3b. As we do not measure the relative phases in the covariance, we

focus on transformations in the joint intensity.

In our experiment the bandwidth of the pump (<5 THz) is much smaller than the bandwidth of the squeezed light (∼47 THz), which prevents all-to-all coupling (the pump frequencies mediate the change in signal frequency). Additionally, the AFC pump peak intensity is reduced by pulse-shaping, therefore reducing the efficiency. Despite these limitations, it is possible to achieve qualitatively different joint spectra by simply changing the pulse shape.

Multimode quantum state sampling at visible wavelengths

The final ingredient in any quantum-optical computing or sensing protocol is measurement, and in this work we focus on photon-counting measurements. Any quantum advantage for computing or sensing typically scales with the number of photons detected so high average photon numbers and high detection efficiency are crucial. Here we demonstrate sampling of the photon-count distribution of our generated states using an EMCCD camera.

We used 5 rows and all 512 columns of a 512×512 pixel EMCCD camera, whose CCD sensor has a QE of ∼95% at 620 nm [73]. The receiver operating characteristic (ROC) curve for thresholding for this camera is shown in Fig. 1.5a: this characterizes the false click rate against the photon-detection efficiency (PDE), parametrized by the threshold value (Appendix B). The green marker indicates the threshold used to generate the subsequent plots, resulting in a competitive photon-detection efficiency of ∼80%.

Fig. 1.5b shows a histogram of the number of photons detected per shot. Blue (left) is prior to thresholding, green (right) is with thresholding. The gain noise in EMCCDs is large, which makes it practically impossible to distinguish between photon numbers ≥1 incident on one pixel.

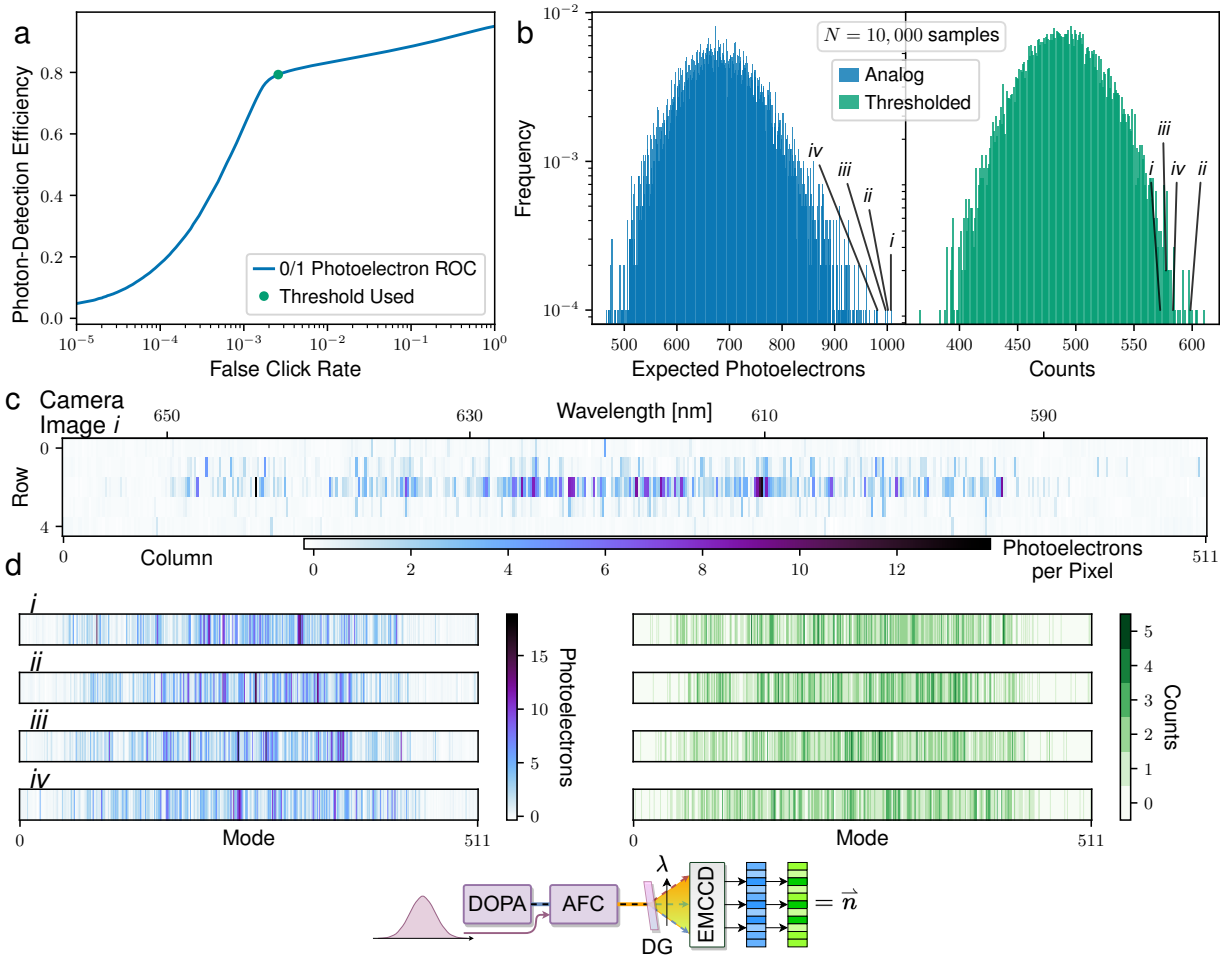

Figure 1.5: **Parallel single-photon detection for multimode-quantum-state measurement: sampling the many-mode, many-photon distribution.** **a.** Receiver operating characteristic (ROC) curve for the EMCCD camera's detectors. This quantifies the trade-off between false click rate and photon-detection efficiency (PDE). **b.** Histogram of the total photon number per event: analog (noisy) and thresholded. We use the term photoelectrons to refer to the amplified charge on the CCD divided by the gain. Some example, high-photon-number events, are labeled on the histogram with callouts *i*–*iv*; these are referenced in the subsequent subfigures. **c.** Example unprocessed camera image from one sampled event. **d.** Samples integrated vertically (left) and thresholded then summed vertically (right). The experimental schematic (bottom) refers to the experimental configuration for collecting the data shown in **b**–**d**. The data in **a** consists of dark frames collected with a closed shutter (see Appendix B and H.)

However, statistical averages tend to be accurate, as this is zero mean noise [74] (see Appendix B). Henceforth, we use the term photoelectrons to refer to the amplified charge on the CCD divided by the gain: since the gain is a noisy process, this is not quantized. The first histogram implies an average of almost 700 photons per shot; with thresholding the average number of clicks is just under 500 per shot. The discrepancy is due to both the effective QE and the high rate of multiple photons incident on one pixel. In Appendix G we analyze the contribution of dark counts and photons from parasitic processes: these are not significant in number compared to the squeezed light photons.

For these frequency-resolving experiments we use more than one pixel-rows of the camera. This is done in order to capture all the photons, due to the spectrometer's point spread function occupying a space larger than one pixel (Gaussian width of $\sigma_{\mathrm{PSF}} \approx 0.6$ pixels). An example of a raw sample is shown in Fig. 1.5c, in units of photoelectrons. With this configuration we could sample at a rate of just over 800 Hz. Using a single row would allow an average sampling rate of 15.7 kHz, which is limited by data readout times. Fig. 1.5d shows samples integrated vertically, for each frequency bin mode. The point spread function in the vertical direction can allow a thresholding camera to act as a pseudo-photon-number resolving detector, by illuminating more pixels (via astigmatic focus) (an established method [75–77] used e.g. in Refs [20]). The point spread function in the horizontal dimension, however, acts as an effective decoherence and must be carefully engineered to fit within the dimensions of a pixel (see Appendix E).

Discussion

The creation, manipulation, and detection of highly squeezed, highly multimode entangled states are important ingredients of many continuous-variable (CV) schemes for quantum computing, sensing, and communication using photonics. When compared to space or time encoding, frequency encoding has significant advantages for integration and scalability, but it is not always practical to perform unitary transformations on frequency modes without substantial loss. We have experimentally demonstrated efficient, broadband, quantum frequency conversion of highly multimode squeezed light generated in the near infrared into the visible using adiabatic frequency conversion (AFC). This simultaneously allows efficient, parallel photon counting across over 400 squeezed and 500 detection modes using CCD-based photon-detector arrays, and the programming of frequency correlations in the multimode squeezed light. Our approach requires no active phase locking, uses a single optical beam path for the quantum light, and the number of modes and shot rates should be scalable well beyond what we have demonstrated. The frequency-domain unitary is programmed by shaping a classical pump pulse before it interacts with the quantum light; the spectro-temporal shaping of the AFC pump pulse can be lossy and so long as the pulse energy is sufficient to fully drive the AFC process, this loss will not affect the quantum light. This is in contrast to the methods for realizing programmable unitaries with space or time encodings, which typically involve a tradeoff between programmability and loss.

To the best of our knowledge, the quantum-optical states we produced are the largest partially programmable, photon-counted, multimode squeezed states produced by a moderate factor (about 2–4 times larger than previous results, albeit with different limitations and caveats), and by an order of magnitude the largest in the frequency domain (see Appendix J). Our work provides a path to constructing large-scale Gaussian boson samplers using frequency encoding.

Our experiment has limitations on the connectivity and programmability of the unitary transformation realized by AFC, as well as limited detection resolution and speed. We explain these limitations and present prospects to overcome them in Appendix K.

We will conclude with some thoughts on future research that could build on what we have already shown. First, engineering the bandwidth of the squeezed light to be compatible with the bandwidth of the pump will enable all-to-all correlations. Second, there are many opportunities for improvements using integrated, on-chip, devices [78, 79]. For example, one could implement the combined DOPA and AFC source on a single chip, with single-spatial-mode waveguiding. This could: eliminate detrimental spatio-temporal effects in AFC; allow for longer interaction lengths than in free space (limited by Rayleigh length) and allow for high intensities with less power, both resulting in more powerful unitary control; and eliminate most interface losses of the quantum light prior to detection. Using integrated photonics would also allow the engineering of dispersion to optimize the squeezing bandwidth, the number of modes in the DOPA, and the interaction complexity imparted by AFC pump. Frequency-encoded squeezed light is not restricted to using supermodes of a continuous basis: quantum states can be engineered to inhabit a (more conventional) basis of (ultrafast) frequency combs lines or discrete frequency bins [30, 80–83]. Shaping the DOPA pump (and possibly the domain poling) to engineer the DOPA joint spectrum [30, 80–82, 84] provides additional avenues for programmability, including the squeezing level of each individual supermode. Finally, understanding how to program the AFC unitary, e.g. through the development of more quantitative models and better calibration procedures, is a valuable avenue of research; it is also important to understand what parts of the state (Hilbert) space can be reached through DOPA and AFC pulse shaping, as well as potentially incorporating additional frequency-domain operations (Appendix D discusses the theory of AFC transformations). Overall we hope our work will enable more widespread study of many-mode, many-photon entangled

quantum states, and provide a useful building block for large-scale frequency-encoded CV quantum technologies.

Methods

Highly multimode squeezing in the frequency domain: details

To study the squeezing process, the DOPA is first simulated with a split step-based partial differential equation solver, based on material properties of LN, and the pump laser (such as dispersion and nonlinearity; pulse duration and energy). The Green's function, which describes how the DOPA acts on the vacuum, is computed with this solver. The Bloch–Messiah decomposition is then applied: this helps us interpret how the DOPA generates squeezing [70, 71], by reducing the Green's function to a set of supermodes and corresponding squeezing or anti-squeezing values. These are shown in Fig. 1.2a and b. For a 4 cm LN waveguide, and 775 nm 200 fs pulse pump, we predict $\sim$600 supermodes with substantial average photon numbers, spanning over 50 THz, or over 400 nm. Refer to Appendix A for the DOPA equations of motion and the relationship between the Green's function and the Bloch–Messiah supermodes.

Three experiments were subsequently performed to verify the numerical predictions: a spectrum measurement, a parametric gain measurement and a coincidence detection measurement. The purpose of the first is to verify that the bandwidth is indeed as broad as predicted. The sec-

ond is to infer the number of modes, based on how the output energy scales. The third is to verify that this light is made up of squeezed states, through photon statistics. The spectrum may be thought of as the incoherent sum of the supermodes, scaled by average photon number, while for the parametric gain, we measure the total photon number as a function of pump power.

The spectrum is measured by monochromation of the DOPA output beam to 1 nm resolution and detecting with a single-photon avalanche diode (SPAD). The spectrum could not be measured past about 1700 nm, due to the SPAD's InGaAs detector response cutoff. As predicted by simulation, the output is broad, spanning hundreds of nanometers (see Fig. 1.2c). The spectrum is in fact broader than simulation, with a shoulder appearing and extending beyond the prediction around 1400 nm: we believe this might be due to pump higher order spatial modes phase-matching the OPA process at the outer wavelengths. The 775 nm pump, unless otherwise specified, is generated from a 200 fs, 1033 nm laser by nonlinear frequency conversion.

The parametric gain experiment involves measuring the output power of the DOPA with a power meter at varying pump powers (see Fig. 1.2d). A high repetition rate laser is necessary to obtain a sufficiently high average output power, hence an 80 MHz Ti:S laser is used to pump the DOPA. The data is fit to the function $\eta M \sinh^2 \sqrt{P/P_0}$, where η represents overall transmission, M number of modes, P pump power, and P_0 power scaling factor (a single squeezed state has $\langle n \rangle = \sinh^2 r$, with squeezing parameter $r \propto \sqrt{P}$). This fit assumes M equally squeezed modes each contributing the same number of photons (thus, a lower bound). Remarkably, the simulation, which includes the responsivity of the detector as a function of wavelength, scales ostensibly the same (albeit with a different nonlinear efficiency P_0). From this measurement we can infer the presence of at least 430 squeezed modes – on the order of 650 modes if accounting for detector responsivity. The Ti:S pulses, 100 fs, have more bandwidth than the 200 fs upconverted 775 nm.

This is accounted for in simulation, which predicts that the squeezing bandwidth will be moderately broader, hence a marginally larger M than in the 200 fs case, but the central squeezed modes are not significantly affected. If a 200 fs experiment were possible at a lower repetition rate, we predict a slightly lower measurement of ηM (see Appendix I for comparisons).

The coincidence experiment (inspired by Ref. [72]) involves splitting the DOPA output beam with a broadband 50:50 beamsplitter. Each beam is detected by a gated SPAD, with the goal of measuring the photon-number covariance between the two beams. The coincidences depend on the photon statistics of the state (namely the bunching, which may also be thought of in terms of $g^{(2)}$ or Mandel Q). Fig. 1.2e shows the covariance between SPAD clicks against the average click rate (as these are threshold detectors). At low photon numbers, only the coincidence rate of highly-multimode squeezed light is expected to scale linearly with respect to the average photon number (see Appendix C for details). To verify this, we performed coincidence detection with the DOPA squeezed light, attenuated 1550 nm laser light, and broadband incandescent lamp light. Indeed, only the squeezed light has nonzero, linear covariance where $\langle n \rangle \ll 1$. As the thresholding detectors yield Bernoulli random variables, the covariance between the two is restricted to a parabola, hence the covariance curves back down around $\langle n \rangle = 1/2$. The slope of the function depends on the transmission (loss). In the next section we use this method as one way to estimate the purity of the detected visible light, but due to the significantly inhomogeneous responsivity of the detectors, this is not possible in the infrared. We can, however, compare to theory ("Predicted" in Fig. 1.2e): a simple model (see Appendix C) can approximately predict the output, based on the spectrum in Fig. 1.2c and the detector QE, assuming biphotons centered around 1550 nm. It predicts a similar scaling to the one measured. As this coincidence measurement is quite sensitive to wavelength-dependent loss, the prediction estimates a decoherence amounting to 98% effective loss while we measured 96%, hence the factor of two between measurement and prediction. This

deviation is due to inaccuracies in the QE and spectrum measurement. We emphasize that this decoherence is due to the limited spectral range and QE of the detector, and not due to the purity of the squeezed states.

These three experiments verify our predictions that the DOPA is a source of highly multimode squeezed light, spanning hundreds of frequency modes.

DOPA Waveguide

The DOPA waveguide consists of 4 cm MgO-doped LN ridge waveguide (Covesion WG-1550-40 WGCK40), poled for second harmonic generation of 1550 to 775 nm and designed to be single-mode at near-IR wavelengths. The LN device is mounted in an oven (Covesion PV40). The oven is mounted with a V-shaped mount (Thorlabs VC3C) and a 3D-printed sleeve to ensure horizontal orientation. The oven and objective lenses (Newport 5726-B-H, 5726-C-H) are mounted on linear axes stages (Newport 562-XYZ, 561D-XYZ-LH, 561D-XYZ respectively). Prior to the waveguide input, a dichroic mirror is used to merge the 775/1550 nm pump and alignment beams (Layertec 109068). A custom mirror (Layertec) is used following the output to separate the pump and signal. The output pump beam is imaged onto a camera (Basler acA800-510um) to view and optimize the pump's spatial profile in the waveguide.

AFC

The crystal used for AFC is a 3 cm poled KTP crystal (Raicol Crystals). The poling profile is designed such that the spatial frequency (inverse of the poling period) varies linearly over the length of the crystal, except at the facets of the crystal. The poling spatial frequency is designed

to phase match the conversion of all the target wavelengths. The front and back 0.25 mm of the crystal are poled with a rapidly varying tanh profile. This improves the rapid passage of the wavelengths that convert near the ends of the crystal. See Appendix G for more details. The crystal is designed for use at 48°C and held in an oven (Eksma Optics HP30), mounted on a 7-axis mount (Thorlabs K6XS, SM1P1).

To optimize the conversion efficiency, bright CW laser light is sent through the DOPA: it thus has same spatial mode as the squeezed light. This alignment beam is used to optimize the spatial overlap of the pump with the signal. The conversion efficiency of the squeezed light is then optimized by maximizing the temporal overlap. This consists of a sweep of the time delay, followed by a sweep of the pump pulse chirp (i.e. duration). As AFC is phase-insensitive, there is no need for phase stabilization. The delay line, a motorized stage with a retro-reflecting right-angle mirror, adjusts the timing of 775 nm pump prior to the DOPA waveguide. The chirp is programmed by adjusting the spectral phase profile of the pulse shaper. See the spectrometer section below for more details.

To mitigate spatio-temporal effects in the AFC, we designed the pump to have a beam waist of 300 µm, and the signal beam to have a waist of approximately 70 µm when focused in the crystal.

To measure the phase-averaged response of the AFC process, monochromated super-continuum (NKT Origami, Thorlabs HN1550, and the infrared monochromator described below) is sent through the AFC, one wavelength at a time, and the resulting visible spectrum measured on the EMCCD camera spectrometer (described below).

775 nm generation from 1033 nm

Pulsed 775 nm light is generated by cascading a second harmonic generation (SHG) and OPA process. Both processes use lithium triborate (LBO; Newlight Photonics). Both crystals are temperature tuned and non-critically phase matched (the optical polarization are aligned to the crystal axes, to avoid spatial walk-off). The lengths are designed to match the temporal walk-off of the 200 fs pulses. The first crystal, 6 mm long, held at 182.6°C, generates 517 nm (y-axis polarized) from 1033 nm (z-axis). The second, 10 mm long, held at 145.4°C, carries out the 517 nm (y) $-$ 1548.5 nm (z) $\rightarrow$ 775 nm (z) process. The 1548.5 nm seed is generated by a diode laser (ILX Lightwave 79800C), amplitude-modulated by a stabilized (Oz Optics MBC-SUPER-PD-3A) electro-optic modulator (EOM) (Eospace AZ-DS5-10-PFA-PFA-LV-LR), to generate 10 ns square pulses. These seed pulses are optically amplified (Pritel PMFA-20), following an isolator. The EOM pulsing is triggered by the Amplitude Satsuma 1033 nm laser, with an appropriate time delay (IDQuantique ID900). The EOM is driven by a pulse/function generator (HP-8116A).

Parametric gain measurements

For this measurement, the DOPA is pumped with a 775 nm, 80 MHz Ti:S laser (Spectra-Physics Tsunami). (All other experiments use the 775 nm pump generated from a 1033 nm laser.) The high repetition rate ensures a sufficiently high average power of squeezed light. The 1550 nm output beam power is measured with a pW-sensitive power meter (Thorlabs S150C), after coupling into multimode fiber (Thorlabs FG200LEA), which is about 95% efficient. The DOPA pump power is removed with a dichroic mirror (Layertec) and measured concurrently (Thorlabs S130VC/S130C). The squeezed light is filtered further with long-pass filters (Thorlabs FELH1150).

At visible wavelengths, the 620 nm power is measured on the camera by integrating the signal on all illuminated pixels, after appropriate filtering of the pump (Thorlabs DMLP900; Semrock FF01-632/148).

Single photon spectrometers

The infrared wavelength spectrometer is based on a diffraction grating on motorized rotation stage (Thorlabs GR25-0616; K10CR1). The first order reflection couples into SMF-28 single mode fiber (Thorlabs F260APC-1550), which monochromates the input. The fiber coupling efficiency is approximately 35%. For single photon detection, this coupled into a InGaAs SPAD (IDQuantique ID Qube NIR Gated), set to the nominal 15% QE. The wavelength-angle correspondence is calibrated using tunable lasers (JDSU mTLG-C1C1L1) between 1527 nm and 1609 nm and fitting to the grating equation, $m\lambda = d(\sin(\theta_{i0}+\Delta) - \sin(\theta_{ir}-\Delta) = 2d\cos[(\theta_{i0}+\theta_{r0})/2]\sin[(\theta_{i0}-\theta_{r0})/2+\Delta]$, where d is the grating constant, θ_{i0}, θ_{r0} are some reference incidence and reflection angles, and Δ is the rotation angle of the grating. The extrapolation to uncalibrated wavelengths is deemed correct as the spectrum stops sharply at 1150 nm, which matches the long pass filter cutoff (Thorlabs FELH1150). However, the coupling efficiency as a function of wavelength uncalibrated.

The visible light spectrometer is based on a diffraction grating (Ibsen PCG-1908/675-972) imaged by an objective lens (Olympus UPLFLN4x) onto the NüVü HNü 512 IS EMCCD camera. See Appendix H for more details. The wavelength-pixel correspondence is calibrated by monochromating supercontinuum (NKT Origami, Thorlabs HN1550) with the infrared monochromator, and converting this light through AFC. The AFC pump is amplitude-modulated to a narrow bandwidth, thus also effectively monochromated. The monochromated supercontinuum wavelength-to-angle is calibrated with an optical spectrum analyzer (Ando AQ6317B). An EM gain of 3000 is

used on the camera.

The SPAD and camera are triggered by the Amplitude Satsuma laser, with an appropriate time delay (IDQuantique ID900).

Coincidence detection

In the infrared, the beam out of the DOPA is split with a broadband beamsplitter and achromatic waveplate (Thorlabs UFBS50502, AHWP10M-1600). The two beam paths are coupled into two SPADs (IDQuantique ID Qube NIR Gated) using fixed collimators (Thorlabs F260APC-1550). The SPADs are set to the nominal 15% QE. The fiber coupling efficiency is approximately 85%. Data acquisition and triggering is configured with an IDQuantique ID900 time controller. This includes feedback for enforcing a global dead time after either of the SPADs fired, and reducing the triggering rate to 2 MHz (maximum SPAD response rate) when using the 80 MHz Spectra-Physics Tsunami Ti:S.

The coincidence detection of visible light is performed with the NüVü EMCCD camera. The diffraction grating is replaced with a Wollaston prism (Thorlabs WP10-A) rotated to achieve 50:50 in the two output beams, at around 45°. The beams are focused with a 30 mm lens (Thorlabs AC254-030-A-ML). The camera is configured to detect in two separate regions of interest (opposite corners of the CCD). The signal from these two 16×16 pixel regions are integrated to obtain the overall power. An EM gain of 500 is used on the camera, which is used in analog mode.

The SPADs and camera are triggered by the Amplitude Satsuma 1033 nm laser, with an appropriate time delay (IDQuantique ID900).

Refer to Appendix C for a theoretical motivation for these experiment.

Temporal pulse shaper

Light diffracted by a transmission grating (Ibsen Photonics PCG-1765-808-981) is focused by a 150 mm cylindrical lens (Thorlabs LJ1629L2-B) onto an spatial light modulator (SLM; Meadowlark P1920-0600-1300-PCIe). A vertically-oriented blazed grating is written on the SLM (orthogonal to the direction that frequency components are dispersed). The SLM is oriented such that the light reflected in the 1st order travels back through the cylindrical lens and grating, following the same path except for a slight downward angle, such that backward-traveling beam is separated by a pick-off mirror. The spatial phases (vertical translations) of the blazed grating along the wavelength axis impart spectral phases to the pulses. Amplitude modulation is also possible by reducing the grating amplitude at a given wavelength, thereby reducing the diffraction efficiency.

The pixel-column-to-wavelength calibration is performed by writing narrow Gaussian-shaped amplitude modulation patterns along the wavelength axis of the SLM. The beam is then measured with an optical spectrum analyzer (Ando AQ6317B) to determine the transmitted wavelength.

The distance between the three optics is optimized by rounding the ellipticity in the beam shape, as viewed on a camera, and minimizing the pulse duration, measured with an autocorrelator (APE Pulsecheck). The orientations of the SLM, grating, and input mirrors are tuned to eliminate the spatial chirp after the initial alignment. The spatial chirp as a function of the transverse directions of the beam is measured by translating the end of a multimode fiber connected to an optical spectrum analyzer (Ando AQ6317B).

The pulse shaper is about 60% efficient without any phase modulations. Phase modulations

can reduce the efficiency if the features are smaller than the imaging resolution of one wavelength onto the SLM.

This pulse shaper is based on the design in Ref. [85].

EMCCD camera operation

The NüVü HNü EMCCD camera is water-cooled by a thermo-electric chiller (Solid State TCube Edge), and the camera operates with a CCD temperature of -60°C, cooled by the built-in TEC. The camera is mounted on one rotation and two linear stages (Newport RS65; Thorlabs PT1A). One linear stage is used to center the camera with respect to the beam. The other two are actuated by motorized micrometers (Thorlabs Z812B; Newport TRA25CC), in order to align the camera to the objective's focal plane, such that the entire spectrum is in focus when used as a spectrometer. These two degrees of freedom are optimized by minimizing the point spread function of two different wavelengths, alternating until convergence.

The laser repetition rate of the Satsuma is chosen to match the maximum frame-rate of the camera (under a given experimental configuration), and the camera is triggered by the laser (IDQuantique ID900 is used to adjust the delay). The blanking and exposure times are generally set to 0.1 ms, as these values do not adversely affect the frame-rates within the experimental configurations reported.

The camera digital readout ("pixel value", p) is converted to photo-electrons, $\langle n_e \rangle$, by subtracting the bias b and dividing by the total gain. The latter is comprised of the electron multiplication (EM) gain and the analog-to-digital conversion factor k (here 21.43 photoelectrons per pixel unit). Hence $\langle n_e \rangle = kp/g - b$. Bias subtraction is calibrated per pixel where possible, as these exhibited

small variations. See Appendix B for an explanation of the measurements performed with an EM-CCD.

See Appendix F for photographs. Fig. 1.6 shows a experimental diagram of the experiment.

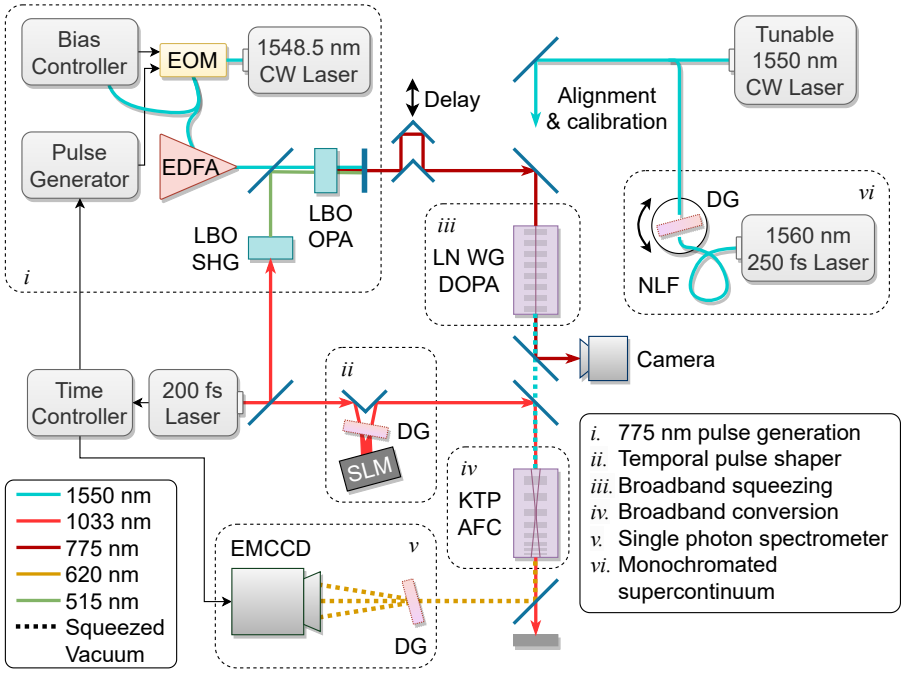

Figure 1.6: **Simplified experimental diagram.** EDFA: erbium doped fiber amplifier. WG: waveguide. NLF: nonlinear fiber. CW: continuous wave.

A Photon statistics in multimode Gaussian quantum optics

The aim of this section is to provide a working knowledge of the physics of multimode Gaussian quantum optics, especially as it relates to our experiments. We provide an explanation of the

underlying theory in our preferred formalism, show how to apply the nonlinear optics equations, and how to predict the supermodes and squeezing values. Finally, we describe the photon number properties of Gaussian states.

We refer to as "Gaussian" the class of states that are fully described by the first two moments of its field operators, or, equivalently, whose phase space distribution is a Gaussian. These states are the most typical in experimental quantum optics (this is a consequence of weak optical nonlinearities and the large – classical – driving fields that are required to achieve them). Furthermore, while multimode or multivariable quantum-mechanical states have generally exponentially large representations, Gaussian states have efficient phase-space representations. This makes working with large multimode Gaussian states tractable.

The bosonic covariance matrix

To fully characterize a zero-mean Gaussian state, we must know the squeezing, the thermal noise, the loss and the correlations between all modes; all this information is encoded in the covariance matrix. In typical convention [86, 87]:

$$\sigma = \frac{1}{2}\left\langle \left\{ \hat{\xi}, \hat{\xi}^\dagger \right\} \right\rangle - \left\langle \hat{\xi} \right\rangle \left\langle \hat{\xi}^\dagger \right\rangle, \; \hat{\xi}^\intercal = \left[\hat{a}_1, \ldots, \hat{a}_M, \hat{a}_1^\dagger, \ldots, \hat{a}_M^\dagger \right], \tag{1.1}$$

where $\hat{a}_i^\dagger$ and $\hat{a}_i$ are the bosonic creation and annihilation operators for some mode i, defined in the usual manner. σ is Hermitian and, for later convenience, we can write it in terms of the submatrices:

$$\sigma = \begin{pmatrix} V + I_M/2 & U \\ U^* & V^\intercal + I_M/2 \end{pmatrix} \tag{1.2}$$

such that V is Hermitian and U is symmetric; I_M is the $M \times M$ identity. As we shall see, $V \sim \langle \hat{a}_i^\dagger \hat{a}_j + h.c. \rangle$ contains the information pertaining to the state's classical properties and thermal

correlations, and $U \sim \langle \hat{a}_i^\dagger \hat{a}_j^\dagger + h.c. \rangle$ encodes the entanglement and higher-order-correlation physics.

Note that it is more common in the quantum optics and information literature to see the quadrature covariance matrix, which use the real-valued canonical variables $\hat{x} \propto \hat{a} + \hat{a}^\dagger$ and $\hat{p} \propto \hat{a} - \hat{a}^\dagger$. The quadrature basis has the advantage of being a real-valued symplectic space. However, the $\hat{a}$-basis is a more natural convention for photon-number properties of the field.

Overall, the Gaussian states defined by σ have $2M^2$ free parameters (real numbers), plus an additional M local phase degree of freedom that may be ignored, as they have no effect on the photon number statistics.

Constructing and decomposing the covariance matrix

Here we summarize some of the body of work pertaining to the matrix representations of multi-mode Gaussian systems. For more depth, see Refs. [13, 70, 71, 86–89].

In this formalism, the space of Gaussian states is closed under Gaussian operations, some of which are represented as linear transformations. We call the transformation a Green's function if it represents the outcome of a process described by a linear differential equation. In a discrete basis of $\hat{a}$-operators, any lossless Gaussian operation can be represented as:

$$\hat{a}_{\text{out}} = C\hat{a}_{\text{in}} + S\hat{a}_{\text{in}}^\dagger \tag{1.3}$$

$$\hat{\xi}_{\text{out}} = \begin{pmatrix} C & S \\ S^* & C^* \end{pmatrix} \hat{\xi}_{\text{in}} = G\hat{\xi}_{\text{in}} \tag{1.4}$$

or in a continuous basis parametrized by ω:

$$\hat{a}_{\text{out}} = \int C(\omega, \omega')\hat{a}_{\text{in}}(\omega') + S(\omega, \omega')\hat{a}_{\text{in}}(\omega')^\dagger d\omega'. \tag{1.5}$$

S may only be nonzero only if there is squeezing (if the Hamiltonian contains an $\hat{a}^\dagger\hat{a}^\dagger + c.c.$ term).

In our experiment, specifically, we are interested in the Green's function of the OPA process, a combination of parametric amplification and dispersion described by the differential equation:

$$\frac{d\hat{a}}{dz}(\Delta\omega) = iD(\Delta\omega)\hat{a} + iA(z, \Delta\omega) * \hat{a}^\dagger \tag{1.6}$$

where D represents the dispersion (phase matching, group velocity difference, and higher order dispersion), and the coupling term A represents the classical pump field, convolved with the quantum field. This equation is the same as you would find in classical nonlinear optics, but with the operator $\hat{a}$ replacing the classical field term. Classically, we could interpret this as the expectation value of the field operator and its evolution; quantum mechanically, we should think of this as the evolution of C, S that act on the operator. In our experiment, we expect S to be predominantly anti-diagonal due to energy conservation, and C to depend on the phase-matching function.

Such a Green's function can be decomposed by the Bloch–Messiah decomposition, which informs us of how much squeezing there is and over what modes. To take advantage of standard computational methods, this is performed in the quadrature basis of $\hat{x}, \hat{p}$ (denote this Green's function by G'). This matrix decomposition returns canonically conjugate squeezed and anti-squeezed "supermodes." Concretely: [1]

$$G' = O_{\text{out}}\Sigma O_{\text{in}}^{\mathsf{T}} \tag{1.7}$$

$$\Sigma = \tfrac{1}{2}\text{diag}(\{s_i\}_{i=1}^{M}, \{s_i^{-1}\}_{i=1}^{M}) = \tfrac{1}{2}\text{diag}(\{\mathrm{e}^{r_i}\}_{i=1}^{M}, \{\mathrm{e}^{-r_i}\}_{i=1}^{M}) \tag{1.8}$$

where s_i are the symplectic eigenvalues, related to the squeezing parameters r_i, and orthogonal matrices O contain the "input" and "output" symplectic eigenvectors or supermodes, which come in pairs (squeezed and anti-squeezed). The input supermodes are not important if the initial

[1] Note: this assumes the convention $\hat{x} = \hat{a}^\dagger + \hat{a}$ and $\hat{p} = i(\hat{a}^\dagger - \hat{a})$.

state is vacuum, as the squeezed vacuum only depends on the output supermodes. Intuitively, Bloch–Messiah may be thought of as a singular value decomposition that preserves commutation relations. These bases diagonalize the Green's function into single mode squeezing operations. Fig. A.7 illustrates the process. Each s_i represents an independent squeezed mode, and a source of photons with $\langle n \rangle = \sinh^2 r_i$ distributed over the mode $O_{\text{out},i}$, or from a quantum noise perspective, a $20 \log_{10} s_i$ dB noise reduction in the mode $O_{\text{out},i}$. A change of basis from $\hat{x}, \hat{p}$ back to $\hat{a}$ transforms the orthogonal matrices into unitary, and the diagonal matrix into a matrix where the quadrants are diagonal:

$$\sigma = \begin{pmatrix} \text{diag}(\{\cosh r_i\}_{i=1}^M) & \text{diag}(\{\sinh r_i\}_{i=1}^M) \\ \text{diag}(\{\sinh r_i\}_{i=1}^M) & \text{diag}(\{\cosh r_i\}_{i=1}^M) \end{pmatrix}. \tag{1.9}$$

With vacuum input, a covariance matrix can be generated as follows:

$$\sigma_{ij} = \tfrac{1}{2}\{G_{ik}\hat{\xi}_k, G_{jk}\hat{\xi}_k\} \Rightarrow \sigma = \tfrac{1}{2} G G^\dagger. \tag{1.10}$$

Additional operations can be similarly applied to the covariance matrix:

$$\sigma \to G \sigma G^\dagger. \tag{1.11}$$

Note that vacuum $\sigma = I_{2M}/2$.

As previously mentioned, (going back to the $\hat{x}, \hat{p}$ basis) the input supermodes cancel out in the vacuum case:

$$\tfrac{1}{2} G' G'^\intercal = \tfrac{1}{2} O_{\text{out}} \Sigma O_{\text{in}}^\intercal O_{\text{in}} \Sigma O_{\text{out}}^\intercal = \tfrac{1}{2} O_{\text{out}} \Sigma^2 O_{\text{out}}^\intercal \tag{1.12}$$

and we see that the Bloch–Messiah decomposition is also valid on the the covariance matrix, although one must account for squared diagonal matrix (however, we note that the Williamson decomposition must be used when the state is not pure: in the case of loss, thermal noise, or if the state has been partially traced out).

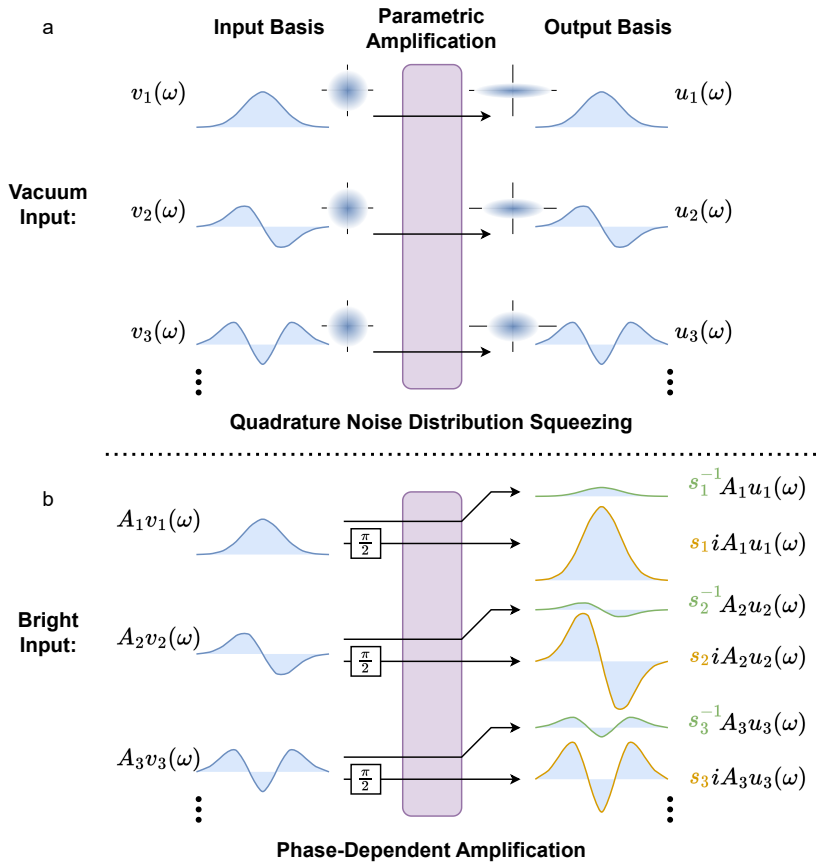

Figure A.7: **Parametric amplification and the Bloch–Messiah decomposition.** The Bloch–Messiah decomposition reduces the parametric amplification to a phase-dependent amplification of an orthogonal set of modes. Each input mode is transformed to an output mode during this process: these modes are generally not the equal due to other effects in the OPA that may alter the signal (e.g. dispersion). **a.** In the case of vacuum input, squeezed vacuum is generated in each output mode independently. **b.** In the case of bright input, a signal may be decomposed into input modes, mapped to output modes, and each component is (de)amplified depending on the phase.

We can observe that:

$$\begin{aligned}\sigma = \tfrac{1}{2}GG^\dagger &= \frac{1}{2}\begin{pmatrix} SS^\dagger + CC^\dagger & CS^\intercal + SC^\intercal \\ C^*S^\dagger + S^*C^\dagger & S^*S^\intercal + C^*C^\intercal \end{pmatrix} \\ &= \begin{pmatrix} SS^\dagger + I/2 & (CS^\intercal + SC^\intercal)/2 \\ (C^*S^\dagger + S^*C^\dagger)/2 & S^*S^\intercal + I/2 \end{pmatrix} = \begin{pmatrix} V + I/2 & U \\ U^* & V^\intercal + I/2 \end{pmatrix}. \end{aligned} \tag{1.13}$$

Note that for the U quadrants to be nonzero, a squeezing operation must be involved through a nonzero S. No unitary C applied to any thermal state can populate U. On the other hand, the squeezing contributes to "thermal" components V, as it adds photons to the field, thus increasing

the photon-number variance.

The formalism introduced so far – where all the operations are unitary or symplectic and preserve commutation relations – cannot account for losses or inefficiencies that must be considered during the frequency conversion and detection steps of our experiment. In both cases, the state occupies unobserved modes, that are traced out. Tracing out modes in a covariance matrix is simply equivalent to removing the corresponding rows and columns, in other words, taking a principal submatrix that omits the traced out modes. For example, this is used to derive the action of a lump loss or noise on a covariance matrix (modeled as passing through a fictitious beamsplitter and tracing out the second port):

$$\sigma \to \sqrt{\eta\eta^{\intercal}} \circ \sigma + (1-\eta) \circ \nu \circ I \tag{1.14}$$

where η is the transmission, $\nu = \bar{n} + 1/2$ represents any thermal noise added ($1/2$ for vacuum). Both are vectors in the general case. The $\circ$ operator is the element-wise or Hadamard product.

We now use these results to describe the physics relevant to our experiment: we convert the infrared squeezed light to visible, but do not detect the remaining infrared light. For notational simplicity let $\hat{\xi} = [\hat{\bar{a}}_{\text{vis}}, \hat{\bar{a}}^{\dagger}_{\text{vis}}, \hat{\bar{a}}_{\text{ir}}, \hat{\bar{a}}^{\dagger}_{\text{ir}}]$. The initial state is:

$$\sigma_{\text{tot}}(z=0) = \begin{pmatrix} \sigma_{\text{vis}} & \sigma_{\text{vis,ir}} \\ \sigma^{\dagger}_{\text{vis,ir}} & \sigma_{\text{ir}} \end{pmatrix} = \begin{pmatrix} I_{2M}/2 & 0 \\ 0 & \sigma_{\text{ir}}(0) \end{pmatrix}. \tag{1.15}$$

The AFC (over crystal length L) acts as a unitary on the entire state:

$$\sigma_{\text{tot}}(z=L) = \begin{pmatrix} G_{\text{vis,vis}} & G_{\text{vis,ir}} \\ G_{\text{ir,vis}} & G_{\text{ir,ir}} \end{pmatrix} \begin{pmatrix} I_{2M}/2 & 0 \\ 0 & \sigma_{\text{ir}} \end{pmatrix} \begin{pmatrix} G_{\text{vis,vis}} & G_{\text{vis,ir}} \\ G_{\text{ir,vis}} & G_{\text{ir,ir}} \end{pmatrix}^{\dagger}. \tag{1.16}$$

Expanding and tracing out the infrared modes we obtain the covariance matrix of the observed visible modes:

$$\sigma_{\text{vis}}(L) = G_{\text{vis,ir}}\sigma_{\text{ir}}(0)G^{\dagger}_{\text{vis,ir}} + G_{\text{vis,vis}}G^{\dagger}_{\text{vis,vis}}/2. \tag{1.17}$$

As the conversion tends to unity, $G_{\text{vis,ir}}$ becomes unitary and $G_{\text{vis,vis}}$ vanishes.

The sum frequency generation equations that yield the Green's function in this case are:

$$\begin{aligned}\frac{d\hat{a}_{\text{vis}}}{dz}(\Delta\omega) &= iD_{\text{vis}}(z,\Delta\omega)\hat{a}_{\text{vis}} + iA(z,\Delta\omega) * \hat{a}_{\text{ir}} \\ \frac{d\hat{a}_{\text{ir}}}{dz}(\Delta\omega) &= iD_{\text{ir}}(z,\Delta\omega)\hat{a}_{\text{ir}} + iA^*(z,\Delta\omega) * \hat{a}_{\text{vis}}\end{aligned} \tag{1.18}$$

where, again, A is the pump field and D is the dispersion, which is notably a function of z, due to aperiodic poling.

Photon number properties of zero-mean Gaussian states

For convenience, in the context of photon number statistics, we can make the covariance matrix symmetric and complex-valued, by defining the transformation X, as first introduced in [16]:

$$\begin{gathered}\sigma' = \sigma - I_{2M}/2, \quad X\sigma' = \begin{pmatrix} U & V^{\intercal} \\ V & U^* \end{pmatrix}, \\ X = \begin{pmatrix} 0 & I_M \\ I_M & 0 \end{pmatrix}.\end{gathered} \tag{1.19}$$

σ' defined in this manner is useful, because we can use it to find any of the following photon number expectation values:

$$\left\langle \prod_i \hat{n}_i^{m_i} \right\rangle = \left\langle \prod_i \left(\hat{a}_i^\dagger \hat{a}_i\right)^{m_i} \right\rangle = \text{Haf}(X\sigma'_{\vec{m}}),\ \vec{m} \in \{0,1\}^M. \tag{1.20}$$

using the conventional definition of the Hafnian (Haf). $\sigma'_{\vec{m}}$ indicates the principal submatrix with indices given by $\vec{m}$. Suffice to say, the Hafnian function is central to the (Gaussian or perturbative) multimode physics of bosons, since it can be thought of as an implementation of Wick's theorem for Gaussian integrals; for zero-mean Gaussian variables x_{i_j}:

$$\langle x_{i_1} \dots x_{i_{2m}} \rangle = \sum_{\mathcal{P}} \langle x_{k_1} x_{k_2} \rangle \dots \langle x_{k_{2m-1}} x_{k_{2m}} \rangle \tag{1.21}$$

where the sum is over all pairings $\mathcal{P}$ – all possible ways to group the i-indices into m pairs of k-indices – hence the Hafnian, a function defined for this very purpose [2]. And of course the operators $\hat{a}_i$ are jointly Gaussian (in their quasi-probability distributions).

The general case with $\vec{m} \in \mathbb{N}^M$ is more complicated, as it requires more careful consideration of operator ordering. Indeed, we were being hasty: $\hat{a}$ is not a random variable, it is an operator. However, Wick's theorem tells us that this was allowed as long as the state and operator have compatible representations. For example, one way to "treat our operators as though random variables" is by converting our expression to Weyl ordering (denoted by $:\ldots:_W$). This requires a prescribed order of $\hat{a}$'s and $\hat{a}^\dagger$'s, and once we have this expression, we may move the operators within without incurring a commutation relation, e.g. $:\hat{a}^\dagger\hat{a}:_W = :\hat{a}\hat{a}^\dagger:_W$. The correct procedure is to expand out the operator expression into Weyl-ordered expressions, and replace each one with the corresponding Hafnian, i.e.:

$$\begin{aligned}
\langle \hat{n}_1^{m_1}\hat{n}_2^{m_2}\ldots\rangle &= \langle (\hat{a}_1^\dagger\hat{a}_1)^{m_1}(\hat{a}_2^\dagger\hat{a}_2)^{m_2}\ldots\rangle \\
&= \sum_{\text{orderings}} c_{\text{order}} \langle :\hat{a}_1^{\dagger\, m_{\text{order1}}}\hat{a}_1^{m_{\text{order2}}}\ldots:_W\rangle \\
&= \sum_{\text{orderings}} c_{\text{order}} \left[\sum_{\mathcal{P}(\text{order})}\prod_{(k_1,k_2)} \langle :\hat{a}_{k_1}\hat{a}_{k_2}:_W\rangle\right] \\
&= \sum_{\text{orderings}} c_{\text{order}} \text{Haf}(X\sigma_{\bar{m}_{\text{order}}}).
\end{aligned} \tag{1.22}$$

It is well known how to relate normal (operator expressions where all the $\hat{a}^\dagger$ precede the $\hat{a}$, denoted by $:\ldots:$) and Weyl forms [87, 90], in our case:

$$:\hat{a}^{\dagger m}\hat{a}^m: = \sum_{k=0}^{m} k!\binom{m}{k}^2\left(-\frac{1}{2}\right)^k :\hat{a}^{\dagger m-k}\hat{a}^{m-k}:_W \tag{1.23}$$

and all modes are treated separately. Additionally, the normal form of $(\hat{a}^\dagger\hat{a})^m$ can be obtained by repeatedly applying commutation relations. This can be generalized to a sum represented by

Stirling numbers S [91]:

$$(\hat{a}^\dagger \hat{a})^m = \sum_{i=1}^{m} S(m,i) \hat{a}^{\dagger i} \hat{a}^i. \tag{1.24}$$

In the case of $\vec{m} \in \{0,1\}^M$, as above, $\hat{a}^\dagger \hat{a} = :\hat{a}^\dagger \hat{a}:_W - 1/2$, and we can subtract the constant directly from the covariance matrix as we did for σ' (σ is conventionally defined as above, with the anticommutator, such that it is conveniently in Weyl form). [2] Similarly, for the second order case,

$$\langle \hat{n}^2 \rangle = \langle (\hat{a}^\dagger \hat{a})^2 \rangle = \langle :\hat{a}^{\dagger 2} \hat{a}^2 + \hat{a}^\dagger \hat{a}: \rangle = \langle :\hat{a}^{\dagger 2} \hat{a}^2 - \hat{a}^\dagger \hat{a}:_W \rangle \Rightarrow \text{Haf}(X\sigma^{(2)}) - \text{Haf}(X\sigma). \tag{1.25}$$

In this example we use $\sigma^{(2)}$ to denote a larger covariance matrix where we repeat the rows and columns of σ for this mode.

These equations involving Hafnians will look familiar to the reader familiar with the recent Gaussian Boson Sampling literature. Indeed, for multimode Gaussian states, calculating the probabilities is largely the dual of calculating the expectation values. The photon number distribution is essentially a generalized Bose–Einstein distribution that incorporates modes, interference and entanglement. To quote the result proven in [15, 16], the probability of a given measurement, $\vec{n} \in \mathbb{N}^M$, has the form:

$$\begin{aligned} P(\vec{n}) &= \frac{1}{\vec{n}! |\sigma + I_{2M}/2|^{1/2}} \text{Haf}\left(X A_{\vec{n}}\right) \\ A &= I_{2M} - (\sigma + I_{2M}/2)^{-1}, \quad \vec{n}! = \textstyle\prod_i n_i! \end{aligned} \tag{1.26}$$

where the Hafnian's argument refers to the principal submatrix with indices given by $\vec{n}$. To gain some intuition, one may notice the Bose–Einstein resemblance via $\sigma_{ii} = \langle \hat{a}_i^\dagger \hat{a}_i + h.c. \rangle / 2 = \langle n_i \rangle + 1/2$, so $(\sigma + I/2)_{ii} = \langle n_i \rangle + 1$, thus in some limiting cases:

$$|\sigma + I/2|^{-1/2} \to \frac{1}{\langle n \rangle + 1}, \quad I - (\sigma + I/2)^{-1} \to \frac{\langle n \rangle}{\langle n \rangle + 1} \tag{1.27}$$

[2] Note, however, that because in this case $\hat{n}^1 = \hat{a}^\dagger \hat{a}$ is already normal ordered, we end up implicitly converting σ to normal ordering by subtracting $I/2$ (i.e. $\sigma'_{ii} = \langle :\hat{a}_i^\dagger \hat{a}_i: \rangle = \langle \hat{a}_i^\dagger \hat{a}_i \rangle$ from $\sigma_{ii} = \langle :\hat{a}_i^\dagger \hat{a}_i:_W \rangle = \langle \{\hat{a}_i^\dagger, \hat{a}_i\} \rangle$).

More precisely, the Bose–Einstein distribution, which is simply geometric, can be thought of as stemming from the recurrence relation:

$$P_{\text{BE}}(n) = P_{\text{BE}}(n-1)a = P_{\text{BE}}(0)a^n = \frac{1}{\langle n\rangle + 1}\left(\frac{\langle n\rangle}{\langle n\rangle + 1}\right)^n \tag{1.28}$$

while this general version follows the similar, yet more complex, Hafnian (Wick's theorem) recursive property:

$$\forall i \text{ s.t. } n_i > 0, P(n_1,\ldots,n_M) = \frac{P(0,\ldots,0)}{\vec{n}!}\sum_{\substack{j=1\\ j\neq i}}^{2N} a_{ij}\text{Haf}(XA_{\overrightarrow{n-\{i,j\}}}), \quad N = \sum_i \vec{n}_i \tag{1.29}$$

where the notation $A_{\overrightarrow{n-\{i,j\}}}$ denotes the subtraction of rows and columns i, j from the matrix $A_{\overrightarrow{n}}$ (note e.g. with $j = i + N$, $\text{Haf}(A_{\overrightarrow{n-\{ij\}}}) \propto P(n_1,\ldots,n_i-1,\ldots,n_M)$, $a_{ij} = P(0,\ldots,n_i=1,\ldots,0)$).

From the quantum computing and complexity theory perspective, the Hafnian is of interest as it belongs to #P, a class of classically intractable functions [4, 16, 17].

A brief sketch of a derivation of the probabilities is as follows; it is perhaps a bit more cumbersome than using phase space formalism (which abstracts away the use of operators and orders) but it is hopefully more transparent. We use the normal form, as this allows us to use a convenient representation of the photon-number Fock state projection operator: the vacuum projection is known to be

$$|0\rangle\langle 0| = :\exp(-\hat{a}^\dagger\hat{a}): \tag{1.30}$$

(see, for example, [92] Eqns. 17–19 for a short proof), and it follows that [87]:

$$\begin{aligned} |\vec{n}\rangle\langle\vec{n}| = |n_1,\ldots,n_m\rangle\langle n_1,\ldots,n_m| &= \prod_i (\hat{a}_i^\dagger)^{n_i}|0\rangle\langle 0|\prod_i \hat{a}_i^{n_i}/n_i! = :\prod_{i=1}^M \exp(-\hat{a}_i^\dagger\hat{a}_i)\frac{\left(\hat{a}_i^\dagger\hat{a}_i\right)^{n_i}}{n_i!}: \\ P(\vec{n}) = \langle|\vec{n}\rangle\langle\vec{n}|\rangle &= \frac{1}{\vec{n}!}\left\langle :\prod_{i=1}^M \exp(-\hat{a}_i^\dagger\hat{a}_i)\left(\hat{a}_i^\dagger\hat{a}_i\right)^{n_i}:\right\rangle = \left\langle :\prod_{i=1}^M \frac{\mathrm{e}^{-\hat{n}_i}\hat{n}_i^{n_i}}{n_i!}:\right\rangle. \end{aligned} \tag{1.31}$$

Since the operator is normal-ordered, we must also use the normal-ordered covariance matrix, which is σ' as defined above (since, e.g. for the first matrix quadrant, $\sigma'_{ij} = \langle:\hat{a}_i^\dagger\hat{a}_j:\rangle = \langle\hat{a}_i^\dagger\hat{a}_j\rangle =$

$\langle\{\hat{a}_i^\dagger, \hat{a}_j\}\rangle - \delta_{ij} = \langle :\hat{a}_i^\dagger \hat{a}_j:_W \rangle - \delta_{ij} = \sigma_{ij} - \delta_{ij}$). Lastly, notice that we can set

$$|0\rangle\langle 0| = :\exp\left(-\tfrac{1}{2}\hat{\xi}^\dagger \hat{\xi}\right): \tag{1.32}$$

so that the notation is compatible with that of the state's covariance matrix.

Hence, the problem is reduced once more to calculus; multivariate Gaussian integrals. We first find $P(0)$, and the rest of the probabilities follow from Wick's theorem, with a modified covariance matrix due to the above $|0\rangle\langle 0|$ Gaussian. The former can be solved with the usual tricks. Let $Z \sim \mathcal{N}(\vec{0}, I)$ be a vector of standard normal random variables. By affine transformation, we can transform it to a vector of arbitrary jointly Gaussian variables: $\sigma'^{1/2} Z + \mu$. Since we are only interested in the case of zero displacement, let the means $\mu = 0$. We thus simplify our calculation by computing the expectation over the multivariate standard normal distribution:

$$\left\langle \exp\left(-\tfrac{1}{2}(\sigma'^{1/2} Z)^\dagger \sigma'^{1/2} Z\right)\right\rangle = (2\pi)^{-M} \int_{\mathbb{R}^{2M}} dZ \exp\left(-\tfrac{1}{2} Z^\dagger (\sigma' + I) Z\right) = |\sigma' + I|^{-1/2}. \tag{1.33}$$

This is the zero-photon probability. We note that $\sigma' + I = \sigma + I/2$ corresponds to the anti-normal covariance matrix (all the $\hat{a}$ precede the $\hat{a}^\dagger$).

Finally, we can include monomial terms in the integral to calculate other probabilities, using Wick's theorem once more, after solving for the effective covariance matrix, A – since the distribution and operator Gaussians combine:

$$\exp\left(-\tfrac{1}{2} Z^\dagger Z - \tfrac{1}{2} Z^\dagger \sigma'^{-1} Z\right) = \exp\left(-\tfrac{1}{2} Z^\dagger A^{-1} Z\right). \tag{1.34}$$

A can be found by invoking the matrix inversion lemma:

$$\begin{aligned} A^{-1} &= \sigma'^{-1} + I \\ A &= (\sigma'^{-1} + I)^{-1} \\ &= I - \sigma'^{-1}(\sigma^{-1} + I)^{-1} \\ &= I - (\sigma' + I)^{-1}, \end{aligned} \tag{1.35}$$

as per convention. We have not been completely rigorous, however, since σ' may not be invertible (if, in a diagonal basis, sigma has some $\langle :\hat{a}_i^\dagger \hat{a}_i: \rangle = 0$, [3] in which case the Gaussian tends towards a delta function); hence, besides for the last line, the above equalities may not be strictly valid. Nonetheless, the moments exist, which is what we need for the moment expansion in Wick's theorem.

Photon number expectation values

We can solve for some lower order photon number moments in terms of σ's elements. To eliminate local phase degrees of freedom, we set all diagonal U_{ii} terms to be real and positive. Here, wherever relevant, we have $i < j < k$ (switching order requires taking complex conjugates of

[3] The field can never be a pure vacuum at finite temperature, although for all intents and purposes it is at optical frequencies, since the photon energy $\hbar\omega \gg k_B T$ (the Boltzmann constant temperature product) at room temperature.

some terms and can therefore introduce inconsistencies).

$$
\begin{aligned}
\langle n_i \rangle &= \text{Haf}(X\sigma'_i) = V_{ii} \\
\langle n_i n_j \rangle &= \text{Haf}(X\sigma'_{ij}) = |U_{ij}|^2 + |V_{ij}|^2 + \langle n_i \rangle \langle n_j \rangle \\
\langle n_i^2 \rangle &= \text{Haf}(X\sigma_{ii}) - \text{Haf}(X\sigma_i) = |U_{ii}|^2 + 2\langle n_i \rangle^2 + \langle n_i \rangle \\
\langle n_i n_j n_k \rangle &= \text{Haf}(X\sigma'_{ijk}) \\
&= \langle n_i \rangle \langle n_j n_k \rangle + \langle n_j \rangle \langle n_i n_k \rangle + \langle n_k \rangle \langle n_i n_j \rangle - 2\langle n_i \rangle \langle n_j \rangle \langle n_k \rangle \\
&\quad + 2\mathcal{R}\left(U_{ij}^* (V_{ik} U_{jk} + V_{jk} U_{ik}) + V_{ij} (U_{ik}^* U_{jk} + V_{ik}^* V_{jk}) \right) \\
\langle n_i^2 n_j \rangle &= \text{Haf}(X(\sigma_{iij} - \tfrac{1}{2}\delta_{jj}) - \text{Haf}(X(\sigma_{ij} - \tfrac{1}{2}\delta_{jj})) \\
&= \langle n_i n_j \rangle (4\langle n_i \rangle + 1) + \langle n_j \rangle (|U_{ii}|^2 - 2\langle n_i \rangle^2) + 2U_{ii}(U_{ij}^* V_{ij} + U_{ij} V_{ij}^*) \\
\langle n_i n_j^2 \rangle &= \text{Haf}(X(\sigma_{ijj} - \tfrac{1}{2}\delta_{ii}) - \text{Haf}(X(\sigma_{ij} - \tfrac{1}{2}\delta_{ii})) \\
&= \langle n_i n_j \rangle (4\langle n_j \rangle + 1) + \langle n_i \rangle (|U_{jj}|^2 - 2\langle n_j \rangle^2) + 2U_{jj}(U_{ij} V_{ij} + U_{ij}^* V_{ij}^*) \\
\langle n_i^2 n_j^2 \rangle &= \text{Haf}(X\sigma_{iijj}) + \text{Haf}(X\sigma_{ij}) - \text{Haf}(X\sigma_{iij}) - \text{Haf}(X\sigma_{ijj}) \\
&= \langle n_i^2 n_j \rangle (4\langle n_j \rangle + 1) + \langle n_i n_j^2 \rangle (4\langle n_i \rangle + 1) - \langle n_i n_j \rangle (4\langle n_i \rangle + 1)(4\langle n_j \rangle + 1) \\
&\quad + 4(\langle n_i n_j \rangle - \langle n_i \rangle \langle n_j \rangle)^2 + (2\langle n_i \rangle^2 - |U_{ii}|^2)(2\langle n_j \rangle^2 - |U_{jj}|^2) \\
&\quad + 2U_{ii} U_{jj} (V_{ij}^2 + U_{ij}^2 + V_{ij}^{*2} + U_{ij}^{*2}) + 8|U_{ij}|^2 |V_{ij}|^2.
\end{aligned}
\tag{1.36}
$$

A few important observations. The equations for the statistics can be separated into a trivial component (composed of lower order statistics) and an interference term, due to complex-valued U and V terms. If the U terms are zero, there are no nontrivial higher order correlations: everything can be described by second- or first-order statistics. Hence why thermal states do not have interesting higher order correlations.

Relatedly, where $U = 0$, there are a vast number of states that have the same photon number

distribution, as there is no information beyond photon number mean and covariance. Measurements carry no information about the underlying supermodes.

The value of $U_{ii} \in [0, \langle n_i \rangle (\langle n_i \rangle + 1)]$, and the two extremes correspond to two-mode and single-mode squeezing respectively. States that have intermediate values can be thought of as a multimode generalization of these two concepts, where the value of U_{ii} represents the locality of the entanglement. When $U_{ii} = 0$, certain higher order correlations also lose interference terms. Therefore, measurements of two-mode squeezed vacuum also lack certain information about the underlying state.

Finally, for a state with sufficient information encoded in U, the inverse problem of retrieving the state and modes from observations is possible, within some limitations. This is within the realm of possibility and future experiments should seek to achieve this.

Returning to the experiment, the photon covariance matrix in Fig. 1.3b (and the simulation in Fig. 1.2a) consists of contributions from both the V (diagonal) and U (anti-diagonal) components.

B EMCCD camera statistics

The electron-multiplying (EM) gain process used in EMCCD cameras is what makes these instruments highly sensitive: by magnifying the charge of a few photoelectrons to macroscopic levels, the camera is capable of detecting single photons. However, the nature of the gain process is stochastic, which introduces noise. Here we introduce the model for the gain process, and discuss how it influences the measurements we are interested in.

Photon statistics after EM gain

The EM gain process adds a high amount of noise, which typically precludes the possibility of resolving the exact photon numbers in EMCCD cameras. When n photons are captured as photoelectrons on the CCD sensor and amplified with EM gain g, the conditional probability of yielding x amplified electrons follows a gamma (Erlang) distribution [74]:

$$P(x;n) = \frac{x^{n-1}\exp(-x/g)}{g^n(n-1)!}. \tag{1.37}$$

To estimate the statistics of the EM gain output x, let P_n be the photon-number distribution incident on a pixel. We are first able to calculate the conditional moments of x with respect to n, use these to calculate (unconditional) moments of x, and finally calculate the photon number moments:

$$\begin{aligned} \langle x^k \rangle_n &= \int_0^\infty x^k P(x;n)dx = g^k \frac{(n+k-1)!}{(n-1)!}, \\ \langle x^k \rangle &= \sum_{n\geq 0} P_n \langle x^k \rangle_n, \\ g^{-k}\langle x^k \rangle &= \sum_{n\geq 0} P_n \prod_{i=0}^{k-1} n+i = \left\langle \prod_{i=0}^{k-1} n+i \right\rangle. \end{aligned} \tag{1.38}$$

This can be extended to correlations between multiple variables, e.g.:

$$\langle x_i^k x_j^l \rangle = \sum_{n_i,n_j\geq 0} P_{n_i n_j} \langle x_i^k \rangle_{n_i} \langle x_j^l \rangle_{n_j} = g^{k+l} \left\langle \left(\prod_{m=0}^{k-1} n_i + m \right) \left(\prod_{m=0}^{l-1} n_j + m \right) \right\rangle. \tag{1.39}$$

We may then solve for the photon number moments by inverting the above equations. Hence we can write down the formulae for our photon statistics of interest (omitting the gain term g):

$$\begin{aligned}
\langle n \rangle &= \langle x \rangle \\
\langle n_i n_j \rangle &= \langle x_i x_j \rangle \\
\langle n_i n_j n_k \rangle &= \langle x_i x_j x_k \rangle \\
\langle n^2 \rangle &= \langle x^2 \rangle - \langle x \rangle \\
\langle n_i^2 n_j \rangle &= \langle x_i^2 x_j \rangle - \langle x_i x_j \rangle \\
\langle n_i^2 n_j^2 \rangle &= \langle x_i^2 x_j^2 \rangle - \langle x_i^2 x_j \rangle - \langle x_i x_j^2 \rangle + \langle x_i x_j \rangle.
\end{aligned} \tag{1.40}$$

Finally, the electronic stages between the EM gain process and a digitized pixel value will introduce additional noise, such as readout noise. However this noise is independent of the signal x, hence it does not affect the above our ability to estimate the photon number.

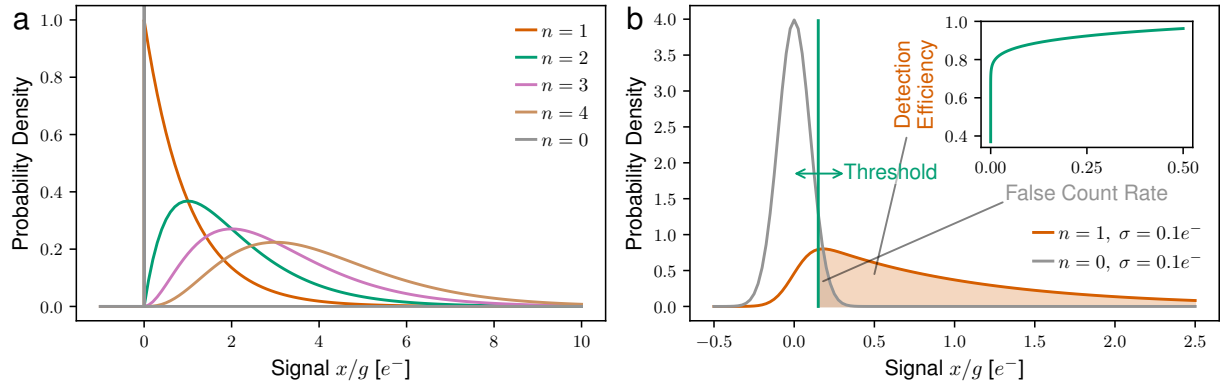

Figure A.8: **Electron multiplying gain model and thresholding. a.** The probability distribution of an amplified signal for a given number of photoelectrons, prior to additional noise. We model this with the Erlang distribution. The signal x is measured in electrons (e^-) divided by the gain g (the expected value of this is the original number of photelectrons). **b.** The probability distribution of the signal with Gaussian readout noise. Although the two probability distributions begin to overlap, in this example, thresholding can be used to distinguish between 0 and 1 (or more) photons with some degree confidence, incurring a tradeoff between the photon-detection efficiency and false count rate. The readout noise has standard deviation σ. The inset shows the analytical (ideal) ROC curve for this example.

Thresholded operation

As discussed above, the electronic signal x, ensuing an EM process with a gain of g, follows a random distribution parametrized by the number of photons captured n – this is shown in Fig. A.8. Due to the stochastic nature of the EM gain process, it is impossible to resolve the original number of photoelectrons n on the CCD sensor from the number of amplified electrons x. However, if there are no photons absorbed by the CCD sensor during the detection window, there is no signal (no electrons) to amplify in the gain process. Hence, there is no excess noise from the EM process, and the variance of the output signal depends solely on the readout noise σ. With a high EM gain, the effective readout noise, $\sigma \ll 1\, e^-$, we can set a threshold on the output signal to discriminate between the absence or presence of photoelectrons with a high degree of confidence.

We evaluate the EMCCD camera in the single-photon detection mode using a threshold to detect the absence or presence of a photon. The threshold value will determine the photon-detection efficiency (PDE) and the false click rate. In general, a lower threshold increases the effective PDE but increases the false click rate, and vice versa. See Fig. A.8b. By varying the threshold value, we obtain a receiver operating characteristic (ROC) curve to characterize the performance of the photon counter (Fig. A.8b inset). The ROC curve quantifies the trade-off in the effective quantum efficiency and dark count rate. In practice, we obtain the false click rate as a function of the threshold by obtaining dark frames – images from the sensor with no illumination – and count how many times a given threshold is exceeded. We obtain the PDE by determining the readout noise from this data, and computing the PDE through the model by comparing g and e, multiplied by the quantum efficiency (QE) of the CCD sensor.

C Coincidence detection

In this section we explain how coincidence detection may be used as a tool to distinguish between different pulsed photonic states, as well as measure the purity of the state.

Derivation

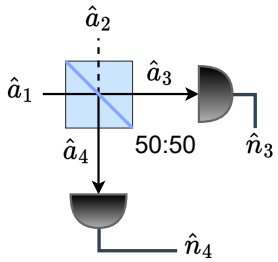

Figure A.9: **Toy model for the coincidence detection experiment.**

Consider a beam of squeezed light incident on a balanced beamsplitter, which is followed by two detectors on each side of the output (Fig. A.9). The first arm of the beamsplitter, with operator $\hat{a}_1$, has some $\langle\hat{n}\rangle$ and $\mathrm{Var}(\hat{n}) = 2\langle\hat{n}\rangle(\langle\hat{n}\rangle + 1)$, in the lossless case ($\eta = 1$). The second input port, with operator $\hat{a}_2$ has vacuum input.

The third and fourth ports, defined by operators $\hat{a}_3, \hat{a}_4$, have $\langle\hat{n}_3\rangle = \langle\hat{n}_4\rangle = \langle\hat{n}\rangle/2$. Evaluating their statistics:

$$\begin{aligned}
\langle\hat{n}_3\hat{n}_4\rangle &= \left\langle \hat{a}_3^\dagger\hat{a}_3\hat{a}_4^\dagger\hat{a}_4 \right\rangle \\
&= \frac{1}{4}\left\langle (\hat{a}_1+\hat{a}_2)^\dagger(\hat{a}_1+\hat{a}_2)(\hat{a}_1-\hat{a}_2)^\dagger(\hat{a}_1-\hat{a}_2) \right\rangle \\
&= \frac{1}{4}\left\langle \hat{n}_1^2 - \hat{a}_2\hat{a}_2^\dagger\hat{n}_1 \right\rangle \qquad (1.41) \\
&\Rightarrow \frac{1}{4}\left(\langle\hat{n}_1^2\rangle - \langle\hat{n}_1\rangle\right), \eta = 1 \qquad (1.42)
\end{aligned}$$

We can now compute the covariance of the number measurements on each detector.

$$\begin{aligned}
\mathrm{Cov}(\hat{n}_3, \hat{n}_4) &= \langle \hat{n}_3 \hat{n}_4 \rangle - \langle \hat{n}_3 \rangle \langle \hat{n}_4 \rangle \\
&= \frac{1}{4} \left(\langle \hat{n}_1^2 \rangle - \langle \hat{n}_1 \rangle \right) - \frac{1}{4} \langle \hat{n}_1 \rangle^2 \\
&= \frac{1}{4} \left(\mathrm{Var}(\hat{n}_1) - \langle \hat{n}_1 \rangle \right) \qquad (1.43) \\
&\Rightarrow \frac{1}{4} \langle \hat{n} \rangle (2\langle \hat{n} \rangle + 1\rangle), \ \eta = 1 \qquad (1.44)
\end{aligned}$$

Note that for coherent states, with $\mathrm{Var}(\hat{n}) = \langle \hat{n} \rangle$, and for thermal states, with $\mathrm{Var}(\hat{n}) = \langle \hat{n} \rangle (\langle \hat{n} \rangle + 1)$, the covariances are 0 and $\langle \hat{n} \rangle^2 / 4$, respectively. Similarly, Fock states with $\mathrm{Var}(\hat{n}) = 0$, have negative covariance; this is the well-known anti-bunching behavior. These different scaling behaviors allow us to experimentally distinguish these different photonic states.

To account for loss, we introduce a fictitious unbalanced beamsplitter operation such that $\langle n_1' \rangle = \eta \langle n_1 \rangle$:

$$\begin{aligned}
\mathrm{Var}(\hat{n}_1') &= \Big\langle \left(\sqrt{\eta} \hat{a}_1 + \sqrt{1-\eta} \hat{a}_0 \right)^\dagger \left(\sqrt{\eta} \hat{a}_1 + \sqrt{1-\eta} \hat{a}_0 \right) \\
&\qquad \left(\sqrt{\eta} \hat{a}_1 + \sqrt{1-\eta} \hat{a}_0 \right)^\dagger \left(\sqrt{\eta} \hat{a}_1 + \sqrt{1-\eta} \hat{a}_0 \right) \Big\rangle - \eta^2 \langle \hat{n}_1 \rangle^2 \\
&= \eta^2 \left\langle \hat{n}_1^2 \right\rangle + \eta(1-\eta) \langle \hat{n}_1 \rangle - \eta^2 \langle n_1 \rangle^2 \\
&= \eta^2 \, \mathrm{Var}(\hat{n}_1) + \eta(1-\eta) \langle \hat{n}_1 \rangle
\end{aligned} \qquad (1.45)$$

So the covariance will simply change by a factor η^2:

$$\begin{aligned}
\mathrm{Cov}(\hat{n}_3, \hat{n}_4) &= \frac{1}{4} \left(\mathrm{Var}(\hat{n}_1') - \langle \hat{n}_1' \rangle \right) \\
&= \frac{\eta^2}{4} \left(\mathrm{Var}(\hat{n}_1) - \langle \hat{n}_1 \rangle \right) \qquad (1.46) \\
&\Rightarrow \frac{\eta^2}{4} \left(2\langle \hat{n}_1 \rangle^2 + \langle \hat{n}_1 \rangle \right) \qquad (1.47)
\end{aligned}$$

If we consider the case of asymmetric loss, it can be shown that the transmission efficiency can

be replaced by the individual efficiencies of the left and right arms, $\eta^2 \to \eta_L \eta_R$.

Finally, in the multimode case, the total covariance is simply the sum of the covariances of all the individual modes (as a consequence of mode independence/commutation). Therefore, a lossy multimode squeezed state has:

$$\mathrm{Cov}(\hat{n}_3, \hat{n}_4) = \sum_i \frac{\eta_{Li}\eta_{Ri}}{4} \left(\mathrm{Var}(\hat{n}_i) - \langle \hat{n}_i \rangle\right) \tag{1.48}$$

$$\Rightarrow \sum_i \frac{\eta_{Li}\eta_{Ri}}{4} \left(2\langle \hat{n}_i \rangle^2 + \langle \hat{n}_i \rangle\right) \tag{1.49}$$

In the case where all modes have $\langle \hat{n}_i \rangle \ll 1$, the covariance is a linear function of the photon number

$$\mathrm{Cov}(\hat{n}_3, \hat{n}_4) \approx \sum_i \frac{\eta_{Li}\eta_{Ri}}{4} \langle \hat{n}_i \rangle \tag{1.50}$$

Notably, the slope is determined by the overall transmission efficiency, $\eta/2$ (assuming a constant transmission), since the average number of photons per detector is

$$\langle N \rangle = \sum_i \frac{\eta_i}{2} \langle \hat{n}_i \rangle \tag{1.51}$$

Therefore, in addition to being a test for squeezing, this experiment may also serve as a measurement of loss.

To measure loss at slightly larger photon numbers, a quadratic fit may be used:

$$\mathrm{Cov}(\hat{n}_3, \hat{n}_4) \approx \frac{\eta}{2}\langle N \rangle + \frac{\eta}{2} C \langle N \rangle^2, \quad C \approx \sum_i \left(\frac{\eta_i \langle n_i \rangle}{\langle N \rangle} \right)^2 \tag{1.52}$$

so long as $\langle n_i \rangle / \langle N \rangle \approx$ const. In other words, the photon numbers in the state must scale linearly. This requires that the squeezed modes remain in the region where $\langle n \rangle = \sinh^2 r_i \approx r_i^2$. Once again, the transmission is given by the linear coefficient.

Threshold detection

Finally, we must consider the case of threshold detectors, where the detector only provides "clicks," if it registers any number of photons. This reduces the two observables to Bernoulli variables. While the total number of photons $\langle N \rangle \ll 1$, the physics remains the same. However, the covariance of Bernoulli variables is bound by a parabola, therefore the photon covariance will behave as such:

$$\begin{aligned} \mathrm{Cov}(n_3, n_4) &= \langle n_3 n_4 \rangle - \langle n_3 \rangle \langle n_4 \rangle \\ &= P(n_3 = 1 | n_4 = 1) P(n_4 = 1) \\ &\quad - \left(P(n_3 = 1 | n_4 = 1) P(n_4 = 1) + P(n_3 = 1 | n_4 = 0) P(n_4 = 0) \right) \langle n_4 \rangle \\ &= \left(P(n_3 = 1 | n_4 = 1) + P(n_3 = 1 | n_4 = 0) \right) (1 - \langle n_4 \rangle) \langle n_4 \rangle \end{aligned} \tag{1.53}$$

where we expect the probabilities to be constant in the many mode, $\langle \hat{n}_i \rangle \ll 1$, scenario, where coincidences are predominantly due to biphotons.

This explains the parabolic curvature in the measurements in Fig. 1.2e.

Predicting coincidence experiment outcomes with wavelength-dependent detector quantum efficiency

The above treatment of coincidence detection assumes a uniform quantum efficiency. However, in our infrared-wavelength experiment, we have that $\eta_{Li}, \eta_{Ri} \to \eta_{Li}(\lambda), \eta_{Ri}(\lambda)$. This thermalizes the state further than uniform loss. Because the QE cutoff is 1700 nm, any photon above this wavelength will never be detected, it is traced out and its sister photon therefore effectively becomes a thermal photon. In addition, the spectrum measured in experiment is far broader than in simulation. Therefore, while it is straightforward to derive the covariance expected for a given QE for

the simulated state, the simulation is not representative of experiment in this case.

To account for this, we derive a simple model to estimate the photon number vs covariance scaling we expect in the experiment (Fig. 1.2e), using the spectrum measured experimentally. In addition, we use the specified detector quantum efficiency.

Assume that the number of modes $M \gg \langle N \rangle$, the total number of photons, and therefore the probability of any given mode yielding photon pairs, $P_m \ll 1$, where m indexes the mode. We truncate the wavefunction of each mode in the photon number basis, as per the biphoton approximation:

$$|\psi\rangle_m \approx \sqrt{1-P_m}|0\rangle_m + \sqrt{P_m}|2\rangle_m + \mathcal{O}(P_m) \tag{1.54}$$

Furthermore assume that the probability of producing more than two photons per event is negligible. Then we can define the probability $\mathcal{P}_m$ that detected photons arise from any given mode:

$$\begin{aligned} \langle N \rangle &= 2\sum_m P_m \\ \sum_m \mathcal{P}_m = 1 \Rightarrow \mathcal{P}_m &= \frac{2}{\langle N \rangle} P_M \end{aligned} \tag{1.55}$$

The covariance is a sum over all covariances, which depend on the coincidence of two photons on the two different detectors:

$$\begin{aligned} \mathrm{Cov}(\hat{n}_3, \hat{n}_4) = \sum_m \mathrm{Cov}_m(\hat{n}_3, \hat{n}_4) &\approx \sum_m \frac{1}{2} P_m \eta_L \eta_R \mathrm{QE}(\omega_{m,1}) \mathrm{QE}(\omega_{m,2}) + \mathcal{O}(P_m^2) \\ &= \sum_m \langle N \rangle \mathcal{P}_m \eta_L \eta_R \mathrm{QE}(\omega_{m,1}) \mathrm{QE}(\omega_{m,2}) + \mathcal{O}(P_m^2) \end{aligned} \tag{1.56}$$

By switching to the continuous frequency basis and parametrizing by $\Delta\omega$ about the central wavelength ω_0, we can obtain the expression:

$$\begin{aligned} \mathrm{Cov}(\hat{n}_3, \hat{n}_4) &\approx \langle N \rangle \eta^2 \int_0^{\Delta\omega_{\max}} d\Delta\omega \mathcal{P}(\Delta\omega) \mathrm{QE}(\omega_0 - \Delta\omega) \mathrm{QE}(\omega_0 + \Delta\omega) \\ &= \langle N \rangle \eta^2 \int_{\lambda_0}^{\lambda_{\min}} \frac{d\lambda}{\lambda^2} \left[\mathcal{P}(\lambda) \mathrm{QE}(\lambda) \mathrm{QE}\left(\frac{2}{\lambda_0} - \frac{1}{\lambda} \right) \right] \Big/ \int_{\lambda_0}^{\lambda_{\min}} \frac{d\lambda}{\lambda^2} \mathcal{P}(\lambda) \end{aligned} \tag{1.57}$$

where $\mathcal{P}(\lambda)$ is now the spectral density (corresponding to Fig. 1.2c in the experiment). As expected, the covariance is linear in $\langle N \rangle$.

For simplicity, it is assumed above that the biphotons are perfectly correlated in frequency, which for a finite bandwidth pump and finite number of supermodes is not physically correct, but a reasonable approximation for a narrow phase-matching bandwidth (with respect to $d\mathrm{QE}/d\omega$).

D Multimode AFC

The aim of this section is to provide some theoretical background and insight into the adiabatic frequency conversion process. Mainly, we are interested in the frequency linear transformations realized by the AFC.

The Landau–Zener grid problem

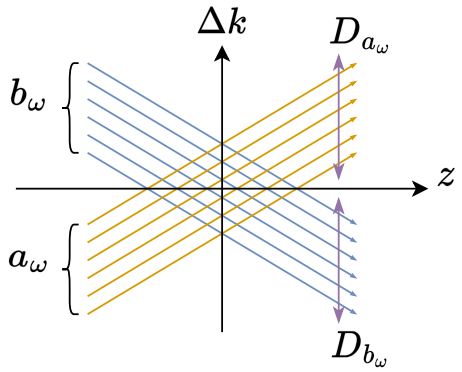

Figure A.10: **Multistate Landau–Zener grid in AFC.** The diagonal lines give the diabatic states. There is some probability of a transition when these coupled states cross.

AFC is often modeled as a two-level system, to which the Landau–Zener formula applies. Energy and time in the canonical system correspond to momentum and space in this nonlinear-optical analog: instead of the energy separation of the states varying with time, the wavenumber

difference between the two frequencies varies with propagation distance.

However, when there are many frequency components at play, the equations for broadband AFC can be generalized to a bipartite system of modes:

$$\frac{d}{dz}\begin{pmatrix} a_\omega \\ b_\omega \end{pmatrix} = i\begin{pmatrix} D_{a_\omega} + \beta_0 z & K(A_\omega) \\ K(A_\omega)^\dagger & D_{b_\omega} - \beta_0 z \end{pmatrix}\begin{pmatrix} a_\omega \\ b_\omega \end{pmatrix} \tag{1.58}$$

where, in the rotating frame, $2\beta_0$ is the rate of change in the quasi-phase matching (QPM) wavenumber (e.g. such that the central wavelengths are phase matched at $z = 0$), the matrices $D = \text{diag}(\Delta\beta_1\Delta\omega + \frac{1}{2}\beta_2\Delta\omega^2 + \frac{1}{6}\beta_3\Delta\omega^3 + \ldots)$ represent the dispersion, and $K(A_\omega)$ represents the coupling between modes. $K(A_\omega)$ is the pump convolution matrix, i.e. Toeplitz matrix of the pump spectrum A. States in a couple to states in b through the pump A, but there is no intra-band coupling (unless unrelated nonlinear-optical processes such as cross-phase modulation come into play).

This kind of bipartite system is sometimes referred to as the Landau–Zener grid, due to the system's graphical representation, shown in Fig. A.10. This general problem is mostly unsolved [93–98], but the concept is straightforward: each level crossing has some transition probability, and the state can effectively perform a random walk, where amplitudes through different paths may interfere [99, 100]. Only certain scattering probabilities, or special cases of the system, have been solved analytically.

The following is an explanation of Fig. A.10. The horizontal axis represents the propagation distance, and the vertical axis the momentum. The diagonal lines, the diabatic states, represent frequency modes. When two lines cross they are phase-matched (equal momentum) and it is possible to have conversion between the modes. The entire process is coherent, hence paths may interfere. This is why applying a phase profile to the pump results in different transformations.

Linear transformations on bipartite systems

Consider a bipartite system of discrete modes – without loss of generality: frequency (e.g. a comb) – such as the one illustrated above in Fig. A.10. An infinite number of modes, and a constant spacing in D – no higher order dispersion – will result in translational invariance in frequency: that is, any shift in the input frequencies would result in the same trajectory and a shifted, but otherwise identical, output. Therefore, up to finite size effects due to a finite length in z, this symmetry implies that the linear transformations must be Toeplitz.

However, dispersion – uneven spacing between modes represented by D – can break that symmetry. With appropriately different spacings, the diabatic levels of the modes will cross at unique points along z, so in principle each crossing may be addressed individually. This could potentially allow arbitrary transformations, if we extend the model to allow A to not be fixed, but a function of propagation, $A(z)$. Slowly changing D – as a function of z – may also help to achieve this.

In the context of ultrafast AFC the pump is fixed: once it is prepared and released, it cannot be changed as it propagates. This limits the control over the dynamics, which impacts the programmability. Nonetheless, dispersion at the pump wavelengths will impart relative spectral phases, and self-phase modulation may occur, hence A may still be as a function of z, even if it is not controllable.

Programming the AFC pump to alter the transformation

In order to alter the AFC dynamics and produce a variety of linear transformations, we are able to perform intensity and phase modulations. We can represent the shaped pump as:

$$A(\omega) = A_0(\omega)\sqrt{\mu(\omega)}\mathrm{e}^{i\phi(\omega)}, \tag{1.59}$$

where $A_0(\omega)$ is the original pump spectrum, $0 \leq \mu(\omega) \leq 1$ is the spectral intensity modulation, and $\phi(\omega)$ is the phase modulation. With a discrete representation, control of $\mu(\omega)$ and $\phi(\omega)$ allows us to modify the Toeplitz coupling matrix as follows:

$$K(A_\omega) = \begin{pmatrix} \ddots & \vdots & \vdots & \\ \cdots & A_j & A_{j-1} & \cdots \\ \cdots & A_{j+1} & A_j & \cdots \\ & \vdots & \vdots & \ddots \end{pmatrix} \rightarrow \begin{pmatrix} \ddots & \vdots & \vdots & \\ \cdots & A_j\sqrt{\mu_j}\mathrm{e}^{i\phi_j} & A_{j-1}\sqrt{\mu_{j-1}}\mathrm{e}^{i\phi_{j-1}} & \cdots \\ \cdots & A_{j+1}\sqrt{\mu_{j+1}}\mathrm{e}^{i\phi_{j+1}} & A_j\sqrt{\mu_j}\mathrm{e}^{i\phi_j} & \cdots \\ & \vdots & \vdots & \ddots \end{pmatrix}. \tag{1.60}$$

E Spectrometer POVM and spectral discretization

A natural question for our experiment is how to reconcile the fact that we have a continuous basis (frequency), but a discrete set of measurement modes: the spectrometer pixels. Indeed, it is common practice in theory and numerics to discretize fields in the manner:

$$\hat{a}_i = \frac{1}{\omega_i - \omega_{i-1}} \int_{\omega_{i-1}}^{\omega_i} \hat{a}(\omega) d\omega \tag{1.61}$$

for sufficiently small intervals such that the outcome converges. However, the experimental implications of this procedure are less obvious, especially if the intervals happen to be too large with respect to the spectral features. The correct procedure is to consider the field in the continuous limit and classically accumulate the statistics or probabilities. This coarse-binning effect can therefore be an effective source of decoherence. The discrete case is recovered in the limit where the field properties are constant within the bins.

Additionally, the point spread function when imaging one wavelength onto the pixelated detector must be much smaller than one pixel. This "pixel-arrival" error is otherwise a source of additional decoherence from a classical process.

F Photographs of the Experiment

Photographs of notable parts of the experiment are shown in Fig. A.11. Important components are labeled and the beam paths are shown as colored overlays. The apparatus is described in the Methods. Fig. A.11a shows the pulse shaper, made up of a diffraction grating and spatial light modulator; b shows the DOPA waveguide and surrounding optics; c shows the AFC crystal; d shows the spectrometer, composed of a diffraction grating and EMCCD camera; e shows the LBO crystals used to generate 775 nm pulses from the 1033 nm source; f shows the characterization setups of 1550 nm squeezed light, separated by flip mirrors, including the parametric gain ("to power meter"), the coincidence detection ("to SPAD"), and the monochromator, also used with the supercontinuum source; g shows the DOPA and AFC in succession, the two central components of the setup.

G Adiabatic frequency conversion design and operation

AFC Design

Fig. A.12a shows the AFC poling period design. The poling spatial frequency is varied linearly throughout the length of the crystal. As a result, the propagating light experiences a linearly changing phase mismatch (detuning), which allows rapid adiabatic passage. The front and back

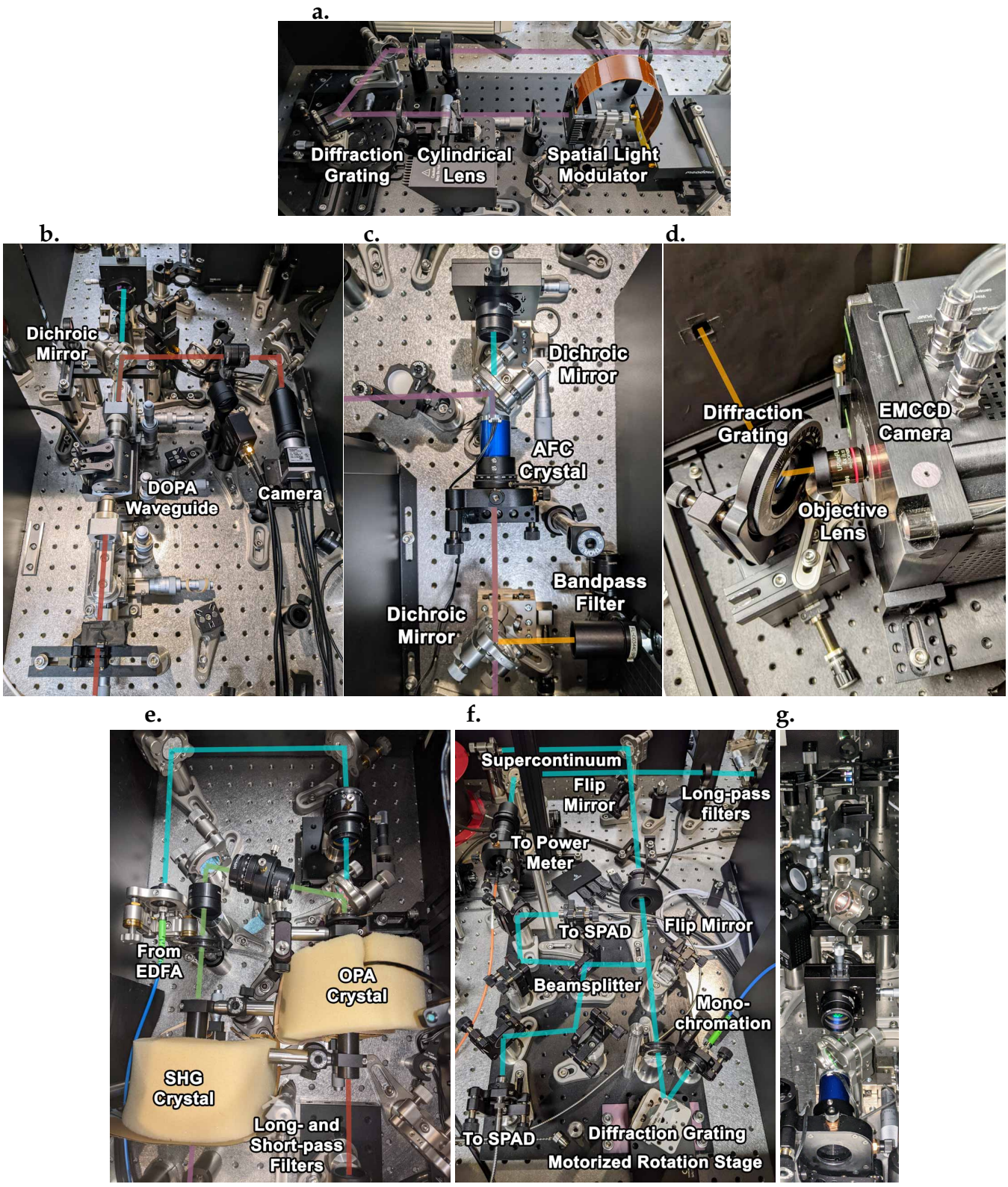

Figure A.11: **Photographs of the Experiment.** The beam paths are overlaid. Beam color to wavelength legend: 1550 1033 775 620 516 nm. **a.** Pulse shaper. **b.** DOPA. **c.** AFC. **d.** Spectrometer. **e.** 775 nm pump generation. **f.** Monochromation and coincidence detection. **g.** DOPA and AFC path.

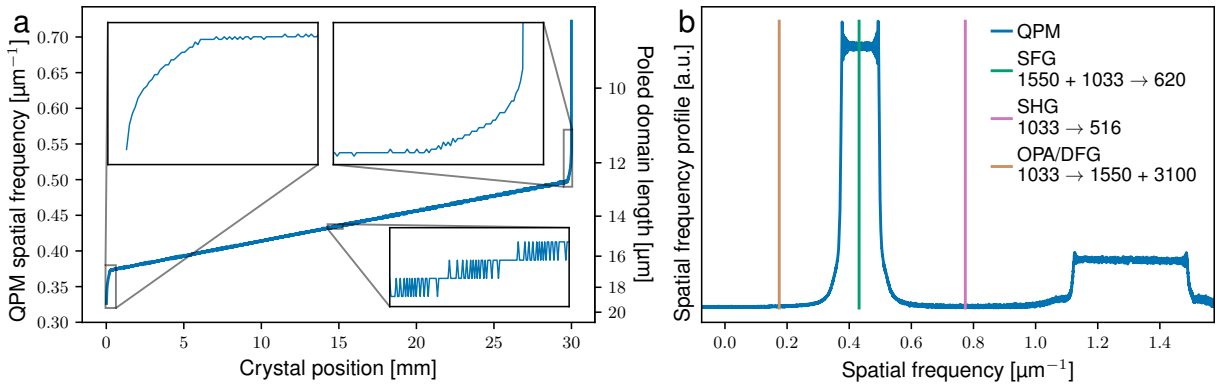

Figure A.12: **AFC design. a.** Crystal domain poling; the spatial frequency and domain length are plotted against position throughout the crystal. **b.** Spatial frequency distribution of the AFC crystal. This is compared to the quasi-phase matching frequencies of desired and undesired nonlinear processes.

of the crystal sweep through poling periods more rapidly, with a tanh profile, to provide the frequencies which convert at the front and back with some propagation distance with detuning. The domain lengths are quantized to multiples of 0.025 μm.

Engineering the poling period is a matter of finding the instantaneous phase $\phi(z)$ for a given varying spatial frequency $\Delta k(z)$, and quantizing the sinusoid of the phase into domains $\chi(z) : [0, L] \to \{-1, +1\}$:

$$\chi(z) = \text{sign}(\sin(\phi(z))), \quad \frac{d\phi}{dz} = \Delta k(z) \tag{1.62}$$

in our case, for example, we need some linear $\Delta k(z) \in [\beta_i, \beta_f]$, hence we use:

$$\Delta k(z) = \beta_i + \frac{(\beta_f - \beta_i)}{L} z, \quad \chi(z) = \text{sign}\left(\sin\left(\beta_i z + \frac{(\beta_f - \beta_i)}{2L} z^2\right)\right) \tag{1.63}$$

The straightforward implementation of this experiment would use the same wavelength to pump both the DOPA and the AFC. Unfortunately, a quick analysis will reveal that the poling spatial frequencies required to quasi-phase match (QPM) the SFG process overlap with those of undesirable nonlinear processes, in both LN and KTP (the two best ferroelectric $\chi^{(2)}$ materials

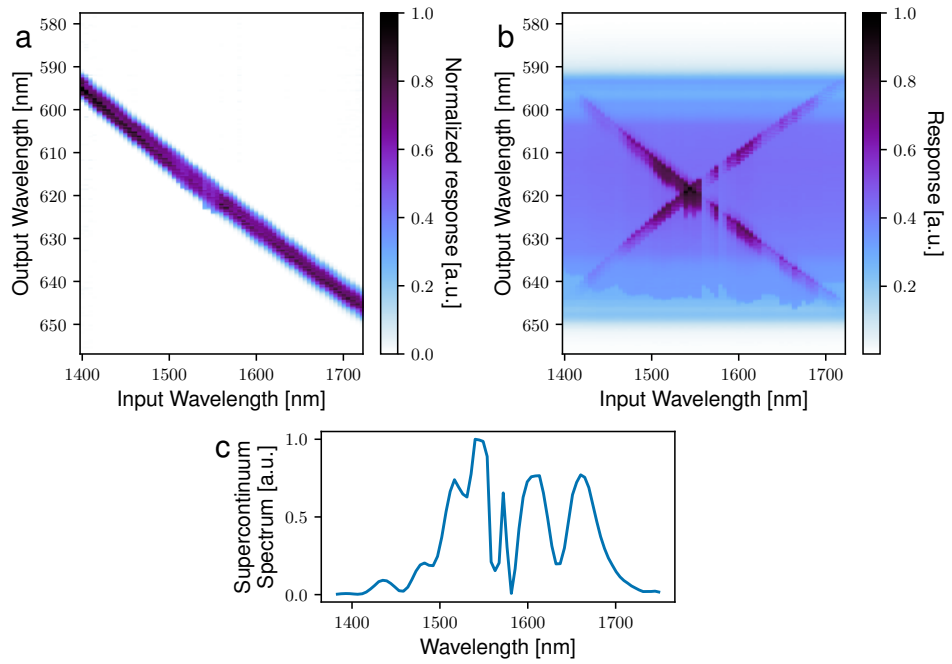

Figure A.13: **AFC input-output transformation.** We measure the intensity (phase-averaged) transformation imparted by the AFC for a given pump, with classical light input. **a.** The visible output transformation matrix of the AFC for single-wavelength inputs. The individual output measurements are normalized. **b.** The same measurement while also pumping the DOPA (unnormalized). The squeezed vacuum light constitutes the constant background spectrum. **c.** Spectrum of the supercontinuum source used as an input, prior to monochromation.

with domain poling). Specifically, we would expect phase-matched second harmonic generation, which would be highly detrimental to the experiment: the pump could lose a majority of its energy to the second harmonic, possibly also causing damage to the crystal. This problem is avoided by using the two different pump wavelengths, 775 nm and 1033 nm. Fig. A.12b shows the spatial frequencies of the AFC poling in relation to possible parasitic processes.

To model the dispersion in KTP we used the z-axis Sellmeier and temperature-dependence equations from Refs. [101, 102].

As an independent verification that the AFC works correctly, we measure the classical, frequency, intensity input-output relation of the AFC (phase-averaged Green's function), as shown

in Fig. A.13a. Monochromated supercontinuum is sent through the AFC, and the resulting visible spectrum measured on the camera. (As described in the Methods section, this also serves as a calibration procedure for the camera pixel-to-wavelength correspondence, by amplitude-modulating the 1033 nm laser to monochromate it.) Fig. A.13b shows the transformation with the inclusion of the DOPA.

Influence of pump shape on frequency conversion

Fig. A.13a shows the (phase-insensitive) experimental measurement of a linear transformation performed by AFC, where the pump is a simple chirped pulse. Observe that a slice of this transformation function (i.e. for a given input; a column of the matrix) resembles a simple Gaussian: the pump spectrum. Indeed, in this regime, to good approximation, the pump intensity profile directly determines the magnitude of the transformation function.

Fig. A.14 demonstrates this effect: by intensity-modulating the pump spectrum (with a fixed phase), for a fixed monochromatic input, we observe that the output signal closely matches the pump profile. However, by virtue of reducing the overall pump energy, the efficiency is affected. In addition, a shift in the input signal ostensibly produces an the same, but shifted, output signal.

While the pump imparts its intensity to the magnitude, the spectral phase of the pump determines the phase in the transformation, which is why we observe that pump phase modulation can generate non-trivial differences in the squeezed-light covariance matrices, in Fig. 1.4.

Fig. A.15 shows the simulated conversion process for a broadband signal. The conversion process under an unshaped pump converts fairly uniformly, while the process under a shaped pump is influenced by interference effects, strongly altering the shape of the output. Fig. A.16 shows a

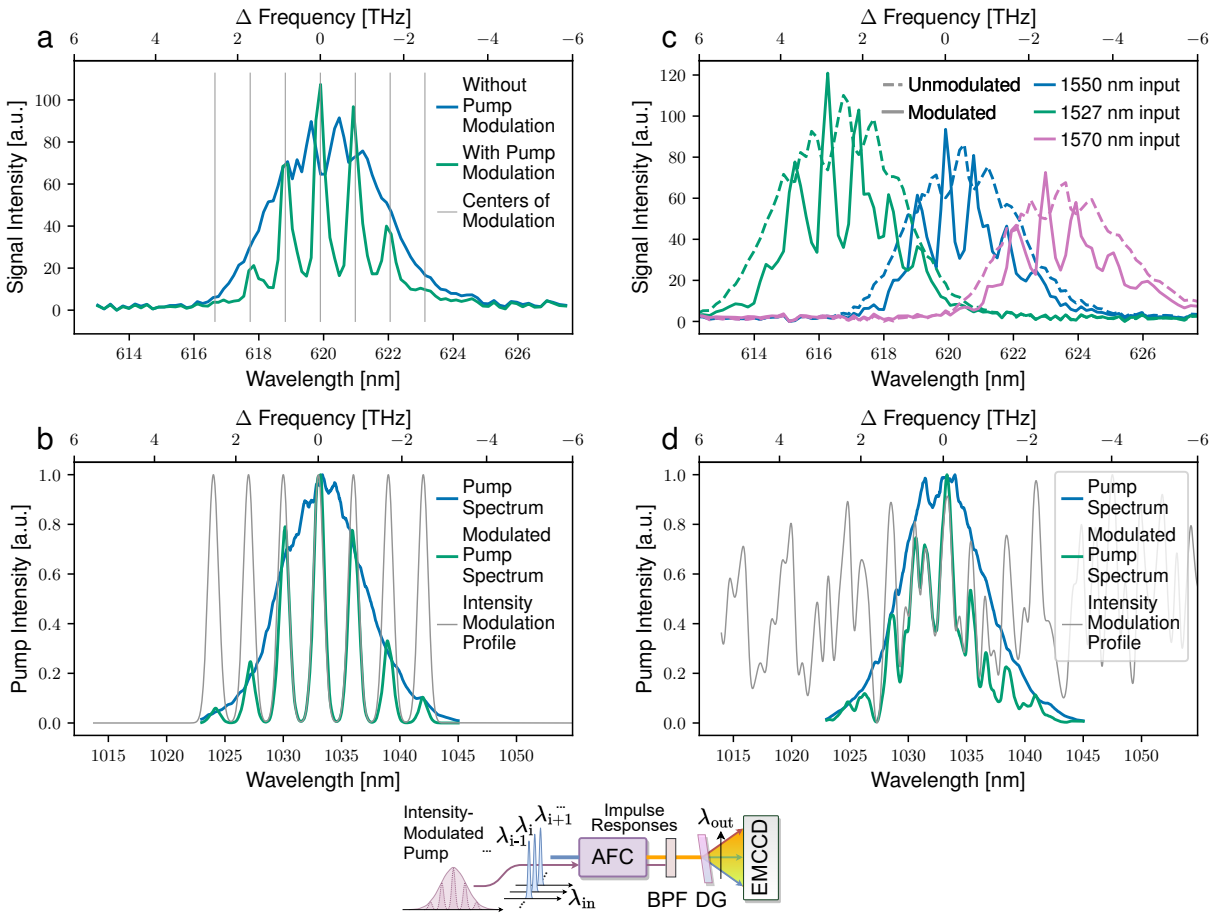

Figure A.14: **Programming the unitary transformation by programming the pump shape: the effect of the pump spectrum shape on the transformation.** Example of how the pump spectrum affects the frequency conversion profile and linear transformation. **a.** The converted signal spectral profiles, under unmodulated and modulated pumps. **b.** The pump spectra for **a**, unmodulated and under intensity modulation. The conversion profile of the signal closely matches the pump spectrum. **c.** The converted signal spectral profiles, unmodulated and modulated, with three different wavelength inputs. The measured signal intensities are essentially translated in frequency. **d.** The modulated and unmodulated pump spectra for **c**. A random intensity modulation pattern is applied. λ_{in} indicates a monochromatic, infrared input light, and λ_{out} indicates the wavelengths measured by the spectrometer.

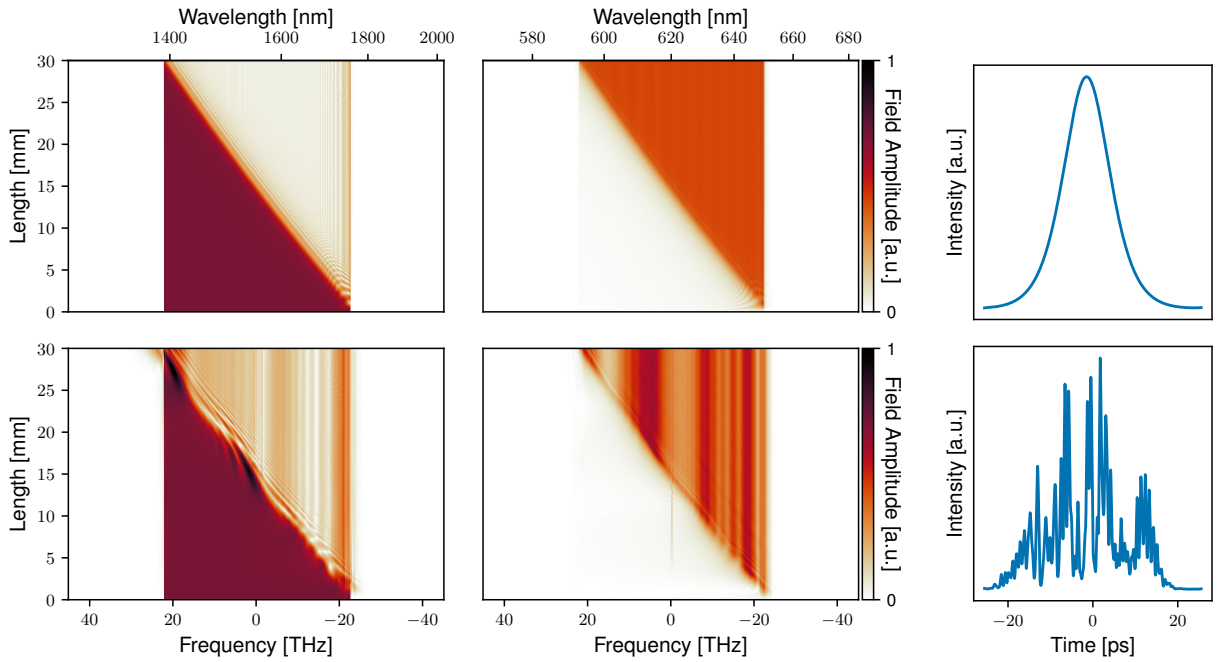

Figure A.15: **Example conversion dynamics in AFC.** The left panel represents the input modes centered around 1550 nm, the center panel represents the converted modes centered around 620 nm, and the right panel represents the pump profile used in the simulation. **Top:** conversion of a single broadband input with an unshaped pump. **Bottom:** conversion of a single broadband input with an shaped pump. The conversion yields a non-uniform spectrum in the converted wavelength due to interference effects.

series of experimentally-obtained photon spectral correlation matrices as the phase modulation of the AFC pump is gradually varied.

Fluorescence in KTP

We have noticed that the 1033 nm pumped KTP crystal generates a spectrum centered around 600 nm. This has been previously observed (see [103] and citing articles; [104]). This fluorescence behavior is likely due to the absorption of green 517 nm second-harmonic light by crystal defects. The green light is generated parasitically in the crystal.

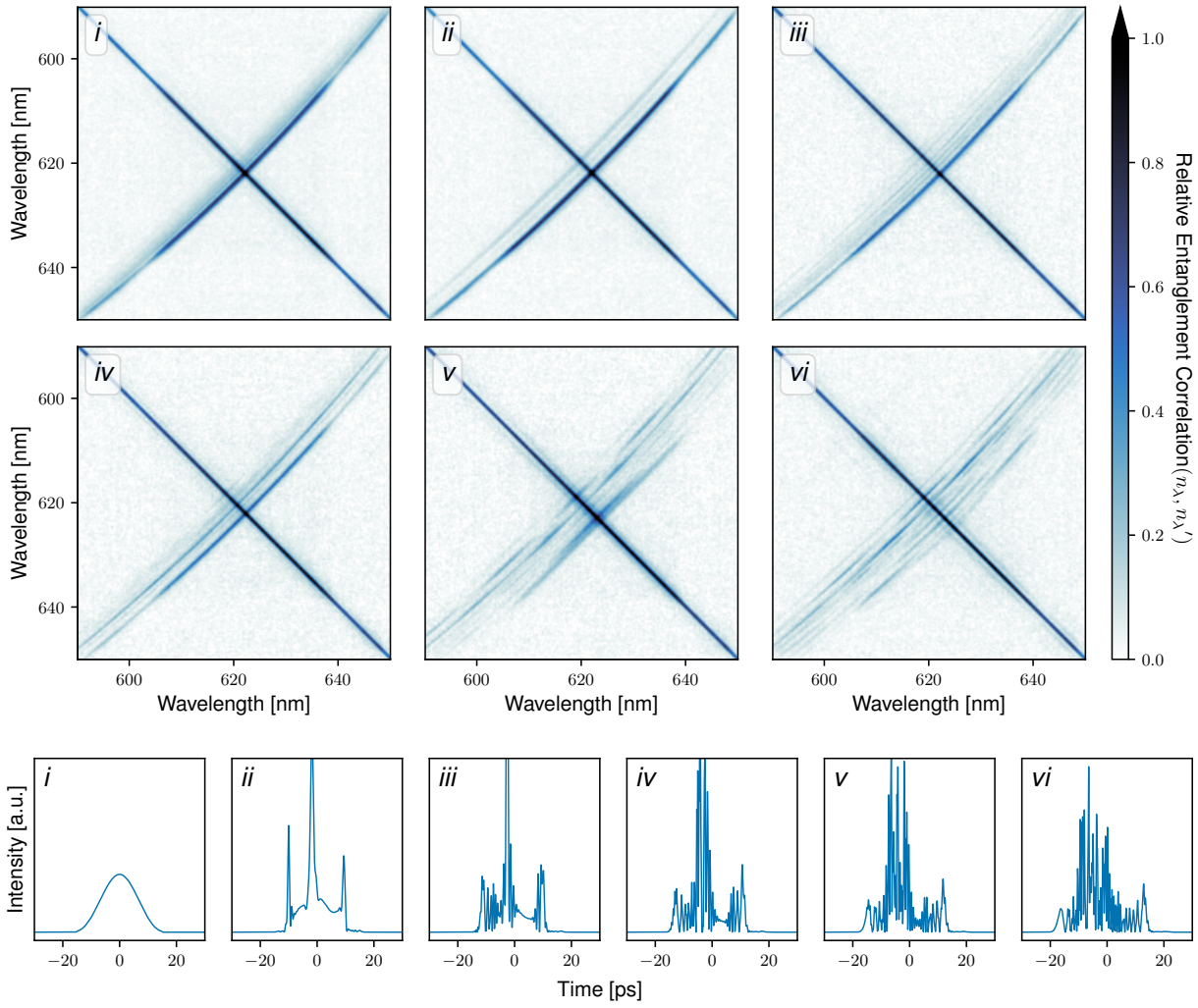

Figure A.16: **Photon spectral correlations while varying the AFC pump phase modulation.** The top panels are photon number correlation plots, where *i* is the state generated by AFC with a chirped pulse, *vi* with the shaped pulse in Fig. 1.4*iv*, and the panels in between are with intermediately-spaced phase modulations of the AFC pump. These six panels show the evolution of the correlation structure as the phase profile varies. The corresponding temporal profiles of the pumps, estimated based on the spectral phase modulations, are shown in the bottom panels. In contrast to Fig. 1.4, the diagonal portion of the correlation matrix has not been subtracted.

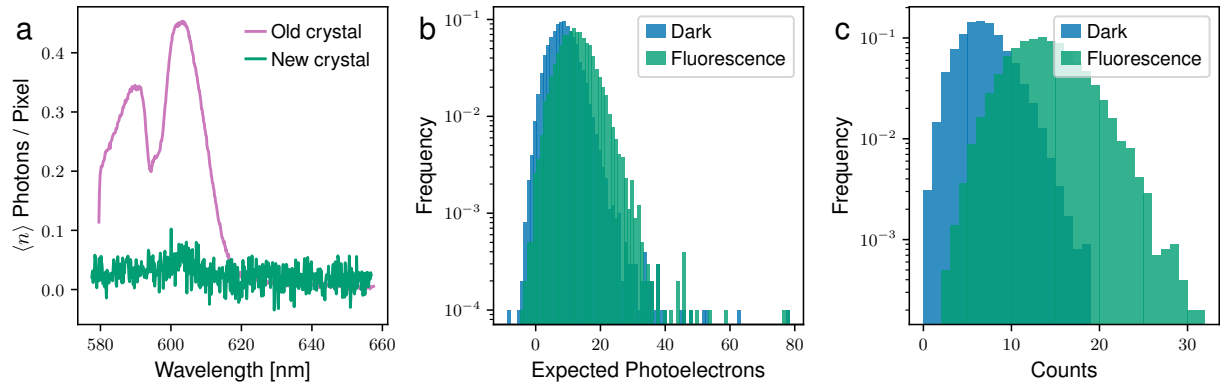

Figure A.17: **KTP fluorescence.** **a.** Spectrum of the fluorescence background emanating from KTP. The old crystal (regularly exposed to a high fluence of green light) emits a distinct spectrum around 600 nm. Fluorescence from the new crystal is low and almost indistinguishable from camera noise. **b.** Cumulative analog signal with dark frames and fluorescence background. **c.** Thresholded counts with dark frames and fluorescence background. Experiments **b-c** were performed with 5×512 pixels.

We also observe that the fluorescing appears to worsen with crystal use. The fluorescence in a new crystal is practically undetectable, but becomes gradually brighter as it is subjected to high peak-power green light.

Ref. [103] reported that different growth methods can suppress this behavior in KTP, however, a different material may have to be considered for future experiments, as this is a problem inherent to KTP.

Fig. A.17a shows the fluorescence spectrum for a strongly fluorescing crystal, which had been subjected to a high fluence of green light over time through use as an AFC crystal (compare to Fig. 1.3a). Below this curve is the background measured in the experiments in Fig. 1.5, performed with a relatively new crystal. Fig. A.17b and c compare the fluorescence signal accumulated by the camera, in analog and thresholded mode respectively. For comparison, dark frames are plotted together (camera shutter closed). On average, fluorescence and background light account for fewer than 10 additional photons per shot.

Dark counts can be reduced by using fewer rows of pixels, at the cost of pseudo-photon number resolving (if thresholding). This experiment used 5 rows of pixels (see Fig. 1.5c).

H Spectrometer design and validation

Design

In order to verify the correlation structure between frequency modes generated by our quantum light source, we design a spectrometer that has a uniformly high spectral resolution and low loss around $\lambda_0 = 620$ nm, the central wavelength. Here we outline the design considerations to achieve the desired spectral resolution.

The number of frequency modes we can resolve is ultimately limited by the number of pixels in each row of the EMCCD camera. We choose an EMCCD camera with a sensor size of 512 by 512, instead of a larger one (e.g., 1024 by 1024), because the better signal-to-noise ratio that would likely preserve more information on our light source (see below for considerations in the choice of camera). The spectrometer is designed for a 60 nm bandwidth (a spectrum between 590 nm and 650 nm). The ideal spectral bin width in each EMCCD pixel is thus $\Delta\lambda = 60/512 \approx 0.12$ nm. The design of the optics must satisfy the following two conditions to provide this resolution:

1. The spatial resolution of the lens must be finer than the pixel size of the EMCCD camera, which is $x_p = 16$ µm. The focal length of the objective lens we chose (Olympus UPLFLN4x) is 45 mm. To match the focal spot size ($1/\mathrm{e}^2$ diameter) to the pixel size, the $1/\mathrm{e}^2$ beam diameter at the back aperture of the objective lens should be at least $2f\lambda_0/(\pi x_p/2)) = 2 \times 45$ mm $\times$ 620 nm/($\pi\times$ 8 µm) $\approx$ 2.22 mm, which is smaller than the back aperture diameter (11.7 mm).

2. The angular resolution of the grating must exceed $\Delta\lambda$, which requires the beam to cover at least $\lambda_0/\Delta\lambda = 620\,\text{nm}/0.12\,\text{nm} \approx 5300$ grating lines. Since the grating (Ibsen PCG-1908/675-972) has a line density of 1908 lines per mm, this means the minimum $1/\mathrm{e}^2$ diameter of the beam on the grating should be at least (5300 lines)/(1908 lines/mm) $\approx$ 2.8 mm. The grating has an area of 20 mm $\times$ 10 mm, sufficiently large for a beam of this size.

In conclusion, to achieve both high spatial and spectral resolution, the beam size must be at least 2.8 mm, which is well within the clear aperture size of the grating and objective lens. The target beam size was designed to be approximately 8 mm, and the actual beam size was slightly smaller than that.

To maximally preserve the quantum properties of the light, all the optics, including routing mirrors, grating, and focusing lens, should have uniformly low loss around 620 nm. The overall quantum efficiency of the spectrometer, including the EMCCD camera quantum efficiency, is measured to be around 75% at 633 nm.

Imaging resolution

As mentioned in the Discussion, there are imperfections with the detection setup. As may be seen in Fig. 1.3a, we do not make full use of the number of pixels: between 10–20% of the spectrometer measures wavelengths outside the target bandwidth. Ideally, customized optics would allow the focal length of the objective lens to match the range of the diffraction angles from the grating to the width of the sensor. As is, the number of detection modes and squeezed modes are close, a possible cause of decoherence.

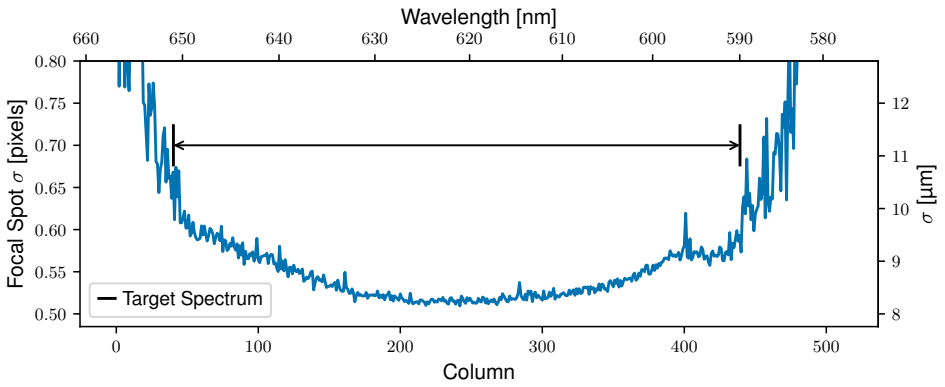

Figure A.18: **Focal spot size throughout the image plane.** Results of a Gaussian fit to the intensity spread at every column; the standard deviation σ is plotted. The intensity drops outside the target spectrum region, hence the sharp transitions in the fits.

Relatedly, the monochromatic focus should be well sub-pixel (16 µm), however, in this experiment we achieved a focus spot with standard deviation $\sigma \approx 0.6$ pixels (Gaussian fit) – on the order of the size of a pixel. We believe the spatial mode quality of the beam is reduced when it is converted, reducing the tightness of the focus. This is also a cause of decoherence because it becomes more difficult to measure the frequency of each photon, and correlations become blurred (Appendix E).

The focal spot size of the spectrometer is shown in Fig. A.18, throughout the wavelength axis (columns) of the camera. The average intensity distribution along the 5 vertical pixels of each column is fit to a Gaussian. The point spread function is a radially symmetric Gaussian in these experiments. It is fairly constant over the image plane (where illuminated), but higher than expected.

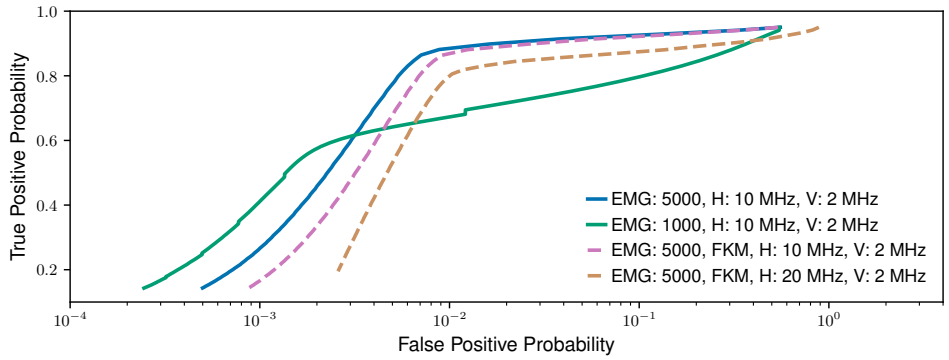

Figure A.19: **Camera performance. a.** ROC curves for different cameras and operational modes. EMG, EM gain; H, horizontal line rate; V, vertical line rate; FKM, fast kinetic mode.

Evaluation of EMCCD camera settings

In order to quantify the performance of the different configurations of the EMCCD camera, we consider their ROC curves. As discussed in Appendix B, these represent the trade-off between the photon-detection efficiency (PDE) and the dark count rate: true positive and false positive probabilities. These are shown in Fig. A.19.

I Squeezing with the Ti:Sapphire pump laser

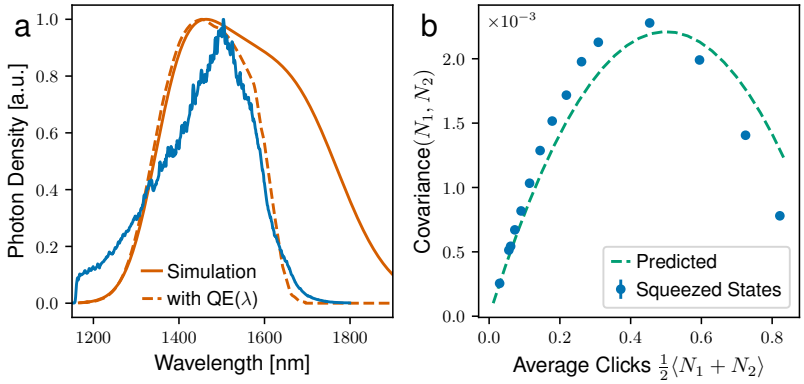

Figure A.20: **Squeezing with the 100 fs Ti:S.** (See Fig. 1.2c and e for comparison.) **a.** Measured and simulated squeezed light spectrum. **b.** Coincidence detection.

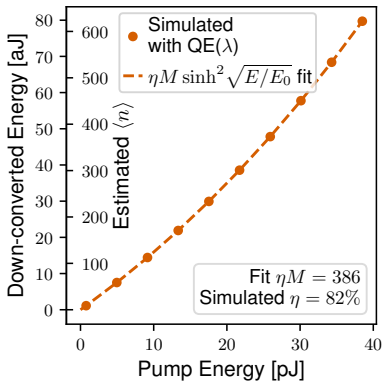

Figure A.21: **Simulated parametric gain with the 200 fs pump.** (See Fig. 1.2d for comparison.)

Fig. 1.2d shows the parametric gain measured with the DOPA pumped by the 775 nm, 100 fs, Ti:S laser, while the other plots in Fig. 1.2 are measured with pumping from the 775 nm converted from the 200 fs, 1033 nm laser. Due to the larger bandwidth of the Ti:S pulses, the DOPA output is slightly different in both cases. Here we show the two other experiments from Fig. 1.2 performed with the Ti:S, for comparison. These results are shown in Fig. A.20.

Similarly, the simulations of the parametric gain we would expect for the 200 fs pump of the DOPA are shown in Fig. A.21. These correspond to the simulated spectrum in Fig.1.2c.

J Comparison to previously published multimode squeezing systems

Table A.1 lists previously published results of experiments demonstrating multimode squeezing, in particular the number of modes and detected photons, where applicable. A subset of these figures of merit are plotted in Fig. A.22. (As we only include references which use some form of squeezed light, this excludes experiments using single-photon emitters.)

Table A.1: **Published results in multimode squeezing.**

Ref.	Domain	# Squeezed Modes	# Photon Detection Modes	Average Total # of Detected Photons	Reprogrammability	Notes
[37]	Frequency	15	-	-	Fixed	4 dB squeezing
[105]	Space	4	4	3	Fixed	Post-selected
[106]	Space	2	6	3	Fixed	Post-selected
[107]	Space	4	4	4	Fixed	Post-selected
[108]	Time	10,000	-	-	Fixed	6 dB squeezing
[38]	Frequency	60	-	-	Fixed	3.4 dB squeezing
[109]	Space	4	9	3	Fixed	Post-selected
[110]	Space	4	13	4	Fixed	
[111]	Space	4	6	6	Programmable	Post-selected
[39]	Frequency	9	-	-	Fixed	
[26]	Frequency	10	-	-	Fixed	
[112]	NA	2	2	80	NA	Single two-mode squeezer
[113]	Time	1,200,000	-	-	Fixed	4.3 dB squeezing
[33]	Frequency	6	-	-	Fixed	6.6 dB squeezing
[114]	Space	24	24	5	Fixed	
[115]	Space	6	12	5	Fixed	
[116]	Space	4	16	4	Fixed	
[117]	Time	1,000	-	-	Partial	1-dimensional connectivity; 5 dB squeezing
[118]	Time & Space	24,960	-	-	Fixed	>4.5 db squeezing
[119]	Time & Space	30,000	-	-	Fixed	4.7 db squeezing
[18]	Space	50	100	43	Fixed	
[40]	Time	61	-	-	Fixed	
[35]	Frequency	40	-	-	Fixed	3.1 dB squeezing
[30]	Frequency	2	-	-	Fixed	
[120]	Space	8	8	11	Programmable	Bipartite connectivity
[19]	Space	50	144	70	Fixed	Programmable phases

[121]	Time	10	20	6	Partial	1-dimensional connectivity
[21]	Time	216	216	125	Programmable	3-dimensional connectivity
[20]	Space	50	144	100	Partial	Programmable phases
[34]	Frequency	20	-	-	Fixed	2.5 dB squeezing
[122]	Time	32	32	1	Programmable	Full connectivity
[123]	Space	32	32	2	Programmable	
This work	Frequency	433	512	680	Partial	500 photons thresholding

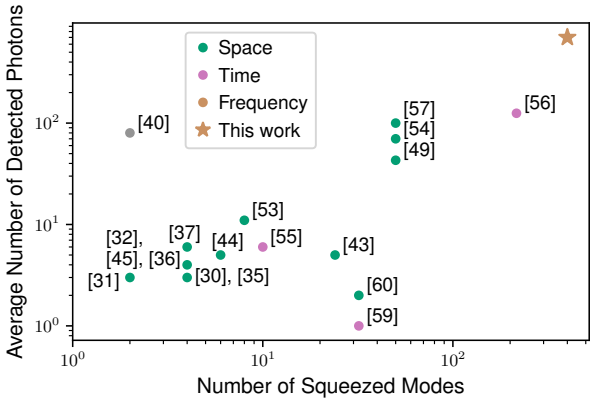

Figure A.22: **Published results in multimode squeezing.** Graphical representation of the experiments collected in Table A.1 in which single-photon detection (as opposed to homodyne detection) was performed. The plot axes represent the number of modes that are initially squeezed (before the application of a unitary, if applicable) and the average total number of photons detected (over all modes).

K Prospects for quantum advantage

Discussion on improvements to the experiment

Here we expand the discussion on the limitations of our experiment and potential improvements.

As previously mentioned in the Discussion, there are currently limitations to our source, (the combination of our generator of multimode squeezed light, followed by the AFC, which performs

a unitary). The class of unitaries we could experimentally realize were limited to fairly local connectivity (approximately to 10% of the nearest frequency modes): hence we could programmably entangle each mode to at most $\sim$20% of the rest (Fig. 1.4b-c). Ideally we would like to be able to realize unitaries with all-to-all connectivity. This may be possible with broader AFC pump bandwidths and higher pump intensities (as shown in simulations presented in Appendix K). In addition, although we have shown control of the joint spectral probability distributions of the state, we currently lack a prescription for what pattern we should program on the pulse shaper for the AFC pump pulse to realize a specific unitary. In principle, this is achievable if our experimental setup were to have a sufficiently fast means to characterize the realized unitary, allowing us to optimize the pulse-shape patterns to realize a given unitary. This can be resolved in the future by building a different characterization setup, for example involving two in-phase, fast-wavelength-sweeping continuous-wave lasers: this would allows to perform fast, phase-sensitive measurements of our source.

There are also imperfections with the detection setup, as discussed in Appendix H. Most importantly, the frequency binning is suboptimal, which may be a cause of decoherence. As mentioned in the Discussion this could be resolved by: waveguided AFC, to avoid spatio-temporal effects that can prevent diffraction-limited spectrometer resolution; using custom imaging optics to optimize the resolution; and switching to a discrete frequency-bin basis rather than a continuous basis.

A disadvantage of using an EMCCD camera instead of, for example, an array of superconducting nanowire single-photon detectors for measurement is speed: the camera's frame rate of 800 Hz is slow. However, the EMCCD camera we used has a linerate of 2 MHz (up to 3.33 MHz with higher noise), which is in principle the relevant speed when only using a single row (or few rows)

of pixels, as is the case for our measurements. However, there is currently a practical bottleneck to reading out the data, which is limited to line readouts at up to 15.7 kHz on our camera model. Several modern EMCCD cameras, including ours, allow reading out bursts of frames (or regions of whole frames, including lines) at up to MHz rates for short time windows; this could allow fast detection for a limited number of shots in the future. Finally, the photon-number sampling we demonstrated used threshold detection or pseudo-photon-number-resolving measurements; ideally, future implementations could be capable of true photon-number-resolving measurements up to high photon numbers per mode (e.g., using ultra-low-noise CMOS cameras [57, 58]).

Influence of pump bandwidth on frequency conversion and entanglement structure

As previously explained in Appendix D, the pump spectrum defines the coupling matrix between the bipartite set of frequency modes. Specifically, the bandwidth determines the range of output signal frequency modes that one input frequency mode may be converted to. The pump bandwidth is relatively narrow in our experimental realization – compared to the signal bandwidth – which limited the connectivity within the state's entanglement structure. However, this is only a practical constraint, and a broader bandwidth pump, which can be achieved through spectral broadening methods, can realize far more complex states.

Fig. A.23a shows, in simulation, the influence of the pump bandwidth (Fig. A.23b) on the state's covariance matrix, for the same temporal intensity profile (Fig. A.23c). The bandwidth directly influences the connectivity. The supermode conversion profile (Fig. A.23d, with reference to Fig. 1.2a), however, becomes less sharp, due to the wider phase matching. The AFC phase-matching bandwidth would have to be redesigned appropriately for different pump bandwidths to mitigate this effect.

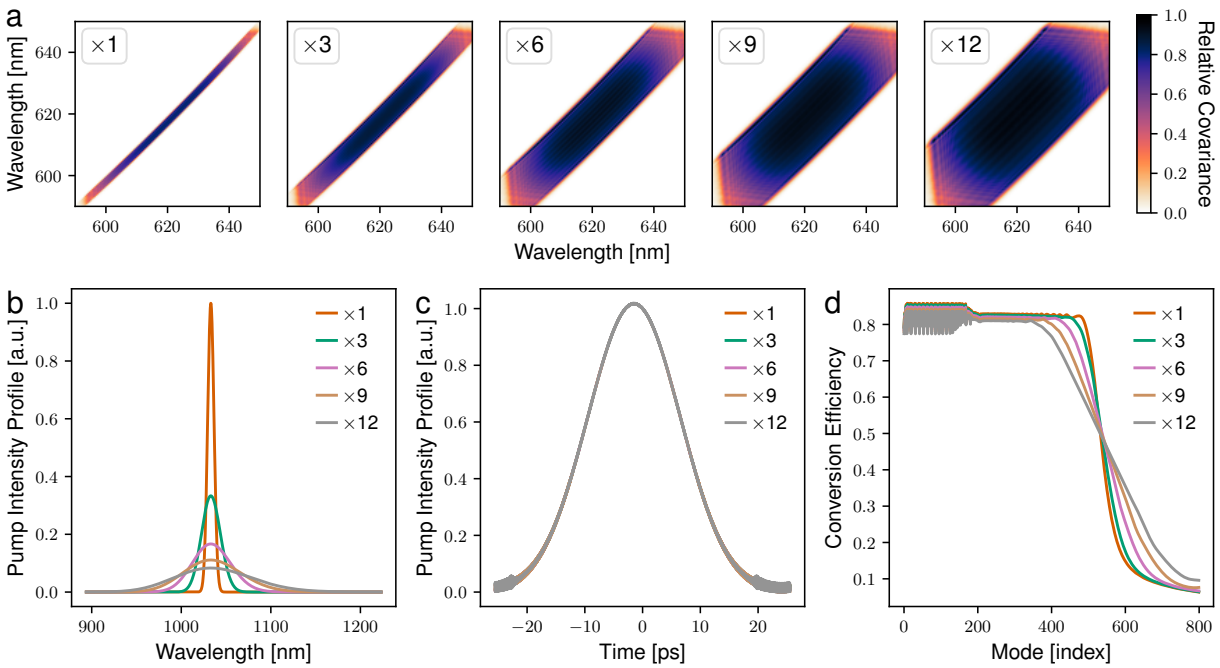

Figure A.23: **Effect of pump bandwidth on the covariance matrix.** These simulations show the AFC driven with pumps of different bandwidths. The chirp is inversely proportional to the bandwidth such that the intensity envelope is the same. The $\times 1$ indicates the bandwidth for a 200 fs 1033 nm pulse, and larger multiples indicate pulses with proportional larger bandwidths. **a.** The covariance matrices. **b.** Corresponding pump spectra. **c.** Corresponding pump temporal pulse profiles, chirped appropriately in order to maintain the same profile throughout. **d.** Conversion efficiency for the major supermodes (see Fig. 1.2).

Validation of photon-counting cameras for quantum advantage

Boson sampling is an intermediate model of linear optical quantum computation [4]. Realizing boson sampling with a level of post-classical computational complexity requires high performance quantum light sources: a large-scale, low-loss photonic circuit; and high-efficiency single-photon detectors – all of which are essential building blocks for universal quantum computation using photons. Gaussian boson sampling (GBS), a variation on this protocol, exploits squeezed vacuum states as input non-classical light sources. For GBS, two main strategies for classical simulation exist. The first uses the non-negativity of quasi-probability distributions (QPD) (generalizations

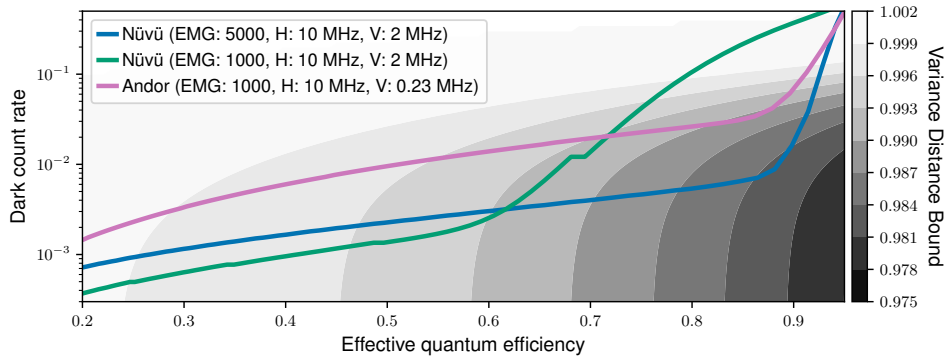

Figure A.24: **Camera performance vs simulability bound.** EMG, EM gain; H, horizontal line rate; V, vertical line rate. **b.** Comparison to the variance distance assuming an overall transmission of $\eta = 40\%$ and squeezing parameter $r = 1$.

of the Wigner function) as a strategy for simulation. The second uses the fact that in GBS, the marginal distributions of photon numbers (i.e., the probabilities to observe some subset of detection events irrespective of the others) are informative about the complete probability distribution.

For the QPD based simulations, an inequality exists that that demarcates the "regime of simulability." Thus, any finite-sized experiment must pass this inequality to show that it is not simulable by this strategy. The inequality is given in Ref. [124]:

$$\operatorname{sech}\left\{\frac{1}{2}\Theta\left[\ln\left(\frac{1-2p_D/\eta_D}{\eta e^{-2r}+1-\eta}\right)\right]\right\} > e^{-\epsilon^2/4K}, \tag{1.64}$$

where r is the squeezing parameters, η is the overall photon transmission rate, K is the number of squeezed sources, ϵ is the total variance distance of the experimental GBS samples compared to the ideal cases, Θ is the Heaviside function, η is the transmission, η_D is the photon detector efficiency and p_D is the dark count rate.

In order to quantify the simulability of the experiment with different photon-counting cameras, we consider the bound for total variance distance ϵ as a function of the parameters determined by the cameras: photon detector efficiency (η_D) and dark count rate (p_D) (as discussed in

Appendix B). We estimate the total optical transmission rate to be $\eta \approx 40\%$. In Fig. A.24 we then compare these (η_D, p_D)-plane trajectories to the left-hand side of the above simulability criterion equation. We consider two EMCCD cameras: the NüVü HNü 512 IS and the Andor iXon Ultra 888.

CHAPTER 2

SPECTRO-TEMPORAL OPERATIONS FOR QUANTUM OPTICS USING FREQUENCY CONVERSION: UNITARY GATES, SQUEEZING AND TRAPS

This work was done together with Ryotatsu Yanagimoto and Peter L. McMahon.

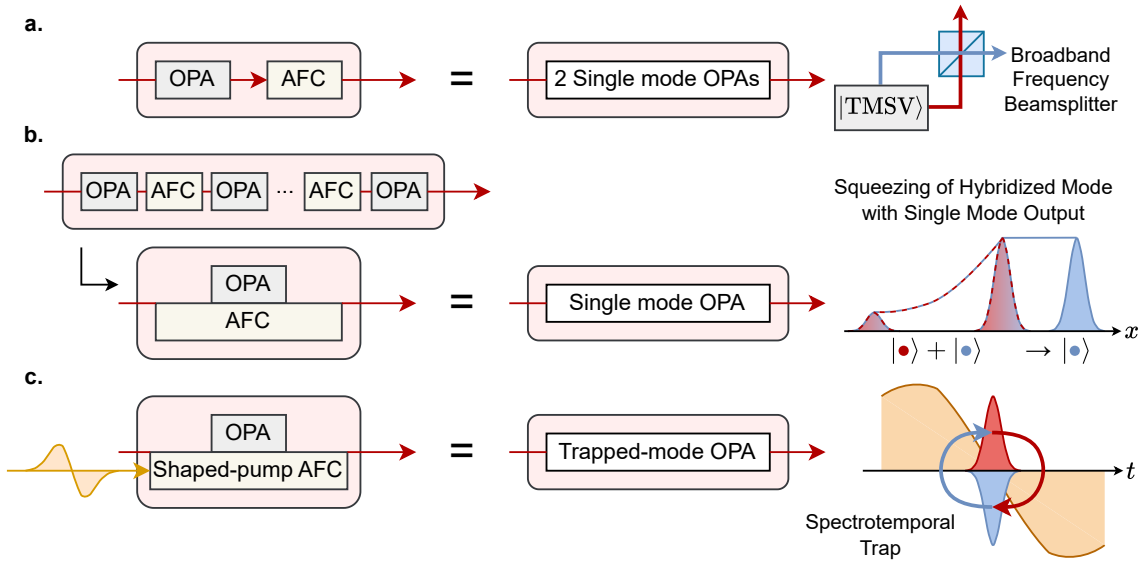

Figure 2.1: **Frequency conversion for frequency-domain quantum-optical state engineering.** Adiabatic frequency conversion (AFC) can be used to efficiently manipulate the frequency degrees-of-freedom of states. AFC enables broadband unitary transformations in the frequency domain, and, combined with optical parametric amplification (OPA), can be used to engineer single-mode squeezing and spectro-temporal state traps. **a.** AFC as a unitary for quantum modes. Consider an OPA, which prepares two-mode squeezed vacuum: it can be followed by an AFC process, acting as a broadband frequency beamsplitter, to output two independent single mode squeezed states. **b.** Simultaneous OPA and AFC for single-mode squeezing. We may wish to improve the previous process, for example by converting back and forth between the modes as we perform OPA, to symmetrize the two-mode process for greater fidelity. Because frequency generation and OPA share the same eigenstates, it turns out that not only is it possible to perform the two processes in parallel, continuously; we can engineer the whole process to phase-match squeezing into a single mode. **c.** Spectro-temporal mode trapping. Single-mode squeezing can be further improved by introducing a potential, or trap, which imposes a set of discrete modes. As we will show, a spectro-temporal trap can be achieved in a combined frequency generation-OPA system by pump shaping.

Single mode squeezing without numerous higher order modes is challenging in optics. This is

due to the requirements of energy and momentum conservation that govern the parametric amplification process used for squeezing, and which tend to make the spontaneously down-converted photons distinguishable. Typically, in a conventional optical parametric amplification (OPA) process, the fewest number of squeezed modes that can be prepared at once is two – in a two-mode squeezed vacuum state. This is known as spectrally separable down-conversion, and the two modes must be either different polarizations or frequencies. In order to recover two independent squeezed states, the two modes must be brought together and interfered with a beamsplitter or equivalent operation.

However, it is well known that this generation of two-mode squeezed states can only preclude higher-order modes when the squeezing is low. Once the spontaneously emitted photons in the squeezed states begin to stimulate further emission, the approximations used to derive the necessary conditions for separability break down, and distinguishability creeps in. This implies the need for squeezing methods with theoretical guarantees of single-modedness.

In this Chapter, we present three general concepts, which build up from each other, and which can, in principle, be applied to generating single-mode squeezing. All of these methods rely on frequency conversion to control the OPA modes: both during and/or after the amplification process. The latter involves sum (or difference) frequency generation (SFG) acting as a spectro-temporal beamsplitter, or unitary operation. The former is a particularly rich concept, which stems from the fact that sum frequency generation and optical parametric amplification both share the same eigenstates. This can be seen from the equations of motion, where κ, γ represent the pumping

strengths:

$$\begin{array}{cc} \text{SFG} & \text{OPA} \\ a' = \kappa b & a' = \gamma b^* \\ b' = \kappa^* a & b' = \gamma a^* \end{array} \tag{2.1}$$

$$\text{Eigenstates: } a \pm b \tag{2.2}$$

These concepts are presented in Fig. 2.1. The first involves using adiabatic frequency conversion (AFC: a specific method for SFG) to act as a spectro-temporal beamsplitter. The AFC follows a two-mode OPA and performs a linear transformation on its output. By appropriately designing the AFC spatial phase-matching profile, the beamsplitting can, in principle, be implemented over arbitrary bandwidths and can account for time delays. The second, which is a generalization of the first concept, is to perform SFG and OPA simultaneously, followed by AFC. This generates single mode squeezing – in a hybridized mode – that finishes in one of the two modes at the end of the AFC process. The third and most powerful idea involves pulse shaping an SFG process to create a spectro-temporal trap over two spectral modes. When this is combined with OPA, squeezing can only occur in the modes of the trap, or effective potential.

The benefit of the frequency-domain approach is that quantum states can be prepared in a single pass of a single device, namely a dispersion-engineered nonlinear waveguide. This precludes the need for physical beamsplitters to interfere the quantum light (as required for spatial or temporal embeddings). The effective beamsplitters arise from the combined effect of the quasi-phase matching (ferroelectric poling pattern) of the material, and the amplitudes and phases of the classical pumps. In addition, simultaneous frequency conversion presents us with a method to control the squeezing modes in an OPA, by way of spectro-temporal traps. Implementing both spectro-temporal beamsplitters and single-mode traps could be a robust method of generating

high quality, multimode Gaussian states, without the distinguishability problems that usually plague these experiments. This could herald a new paradigm for building programmable quantum light sources.

Results

Broadband spectro-temporal operations with adiabatic frequency conversion

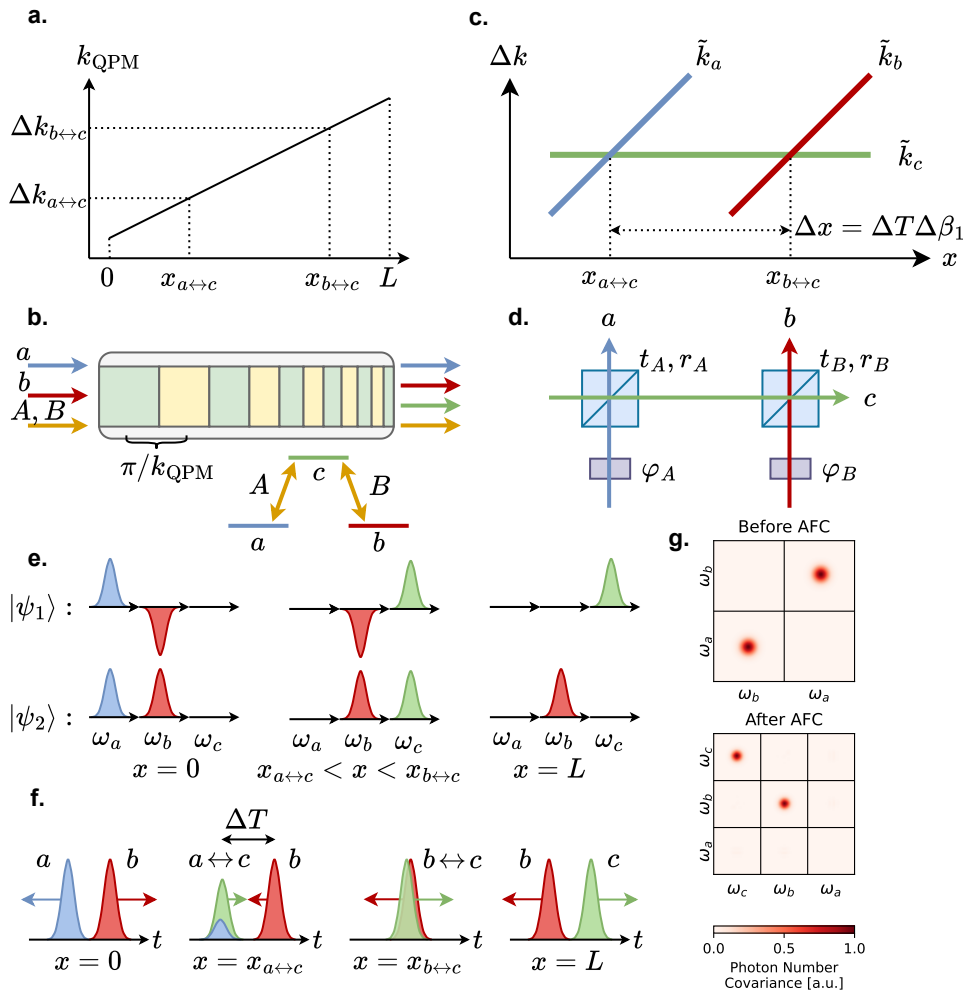

Here we discuss how to use frequency conversion, namely AFC, to perform unitary transformations. As an illustrative example, we will discuss how to separate a two-mode squeezed state

Figure 2.2: **Unitary transformations with AFC: converting two-mode squeezed vacuum into pairs of single mode squeezed vacuum. a.** Quasi-phase matching adiabatic frequency conversion. Over the length of the crystal L, we sweep the spatial frequency of the poling k_{QPM}, as illustrated in **b**. The sweep passes through $\Delta k_{a\leftrightarrow c}$ and $\Delta k_{b\leftrightarrow c}$, the phase matching necessary for conversion between the pair of modes a, c and b, c respectively. These conversions occur at locations $x_{a\leftrightarrow c}$, $x_{b\leftrightarrow c}$ along the length of the crystal. Two pump modes A, B couple a, b to c. **c.** Eigenvalue diagram of the system. As k_{QPM} changes, the phase matching between the pairs of modes a, c and b, c changes. We can choose a rotating frame in which c has constant spatial frequency $\tilde{k}_c$ (eigenvalue), and while a and b rotate with $\tilde{k}_a$ and $\tilde{k}_b$, changing as a function of x. Coherent conversion occurs as the eigenvalues cross. Hence, the state can be interpreted to travel along the trajectories, analogously to the spatial beamsplitter and phase-shifter configuration illustrated in **d**. The magnitudes and relative phases of pumps A, B determine the transmissions (t_A, t_B), reflection (r_A, r_B), and phase (φ_A, φ_B). **e.** Two-mode squeezed state conversion in the frequency-domain. The initial state is composed two supermodes: an even and an odd superposition of a, b, which are thus fully entangled. Following the first conversion, the a component of both supermodes transfer to c. Following the second conversion, by engineering a balanced beamsplitter interaction and setting an appropriate phase difference between the pumps, one transfers to b, and the other to c, disentangling the modes into independent squeezed states. **f.** Modes in the time-domain. Two-mode squeezing requires that mode a have greater (lesser) group velocity than b. In order for the frequency components of the states to interact with each other during conversion they must be coincide in time. We pick c to have the least (greatest) group velocity, such that b, c return to each other. At $x_{a\leftrightarrow c}$, b, c will have a separation of ΔT. We scale this delay by the group velocity difference $\Delta\beta_1$ to find the necessary distance between the two conversion points $\Delta x = x_{b\leftrightarrow c} - x_{a\leftrightarrow c}$ such that b, c overlap during the second conversion. **g.** Simulated photon covariance matrices (join spectral intensity) at the input and output; before and after conversion. This process can, in principle, be made arbitrarily broadband by appropriately tuning the slope and curvature of $k_{\text{QPM}}(x)$.

into two independent squeezed states. This is an enlightening example since it requires compensating for group velocities and time delays. In addition, this is a novel way to design a device for single pass, single-mode squeezing. The requirements for achieving spectrally separable, two-mode squeezing are derived in Ref. [125] and summarized in Appendix E. Here we focus specifically on the case where the two modes have equal bandwidths. Two-mode squeezing requires that – after the OPA process – the two modes are temporally separated and walking off. However, in order to interfere the pulses, they must be brought back together to overlap in time. We there-

fore use an ancillary mode to mediate this interference. Having an additional mode allows more freedom in the choice of OPA signal and pump wavelengths.

Fig. 2.2 illustrates the concepts and the dynamics of the conversion process. Call the three modes a, b, c. Fig. 2.2a represents the simplest design that can perform the frequency beamsplitting to mode sort a two-mode squeezed state into two independent states. The quasi-phase matching k_{QPM} function can be made linear, crossing through the poling period necessary to convert a, c and b, c, pumped by (quasi-)monochromatic modes A, B, as shown in Fig. 2.2b. Accounting for time delay is a matter of appropriately spacing the conversion points based on the differences in group velocity, and is covered in Appendix A. Similarly, the slope of the AFC phase matching can be designed to compensate for dispersion, which enables broadband beamsplitting: piecewise linear to compensate for group velocity mismatch, or nonlinear to account for group velocity dispersion. This is covered in Appendix B.

Fig. 2.2c represents the eigenvalue diagram. The eigenvalues represent the spatial rotation frequency Δk of the modes as a function of position x in the crystal (in this case in the rotating frame of mode c). The speeds of rotation of a, b and c – $\tilde{k}_a$, $\tilde{k}_b$ and $\tilde{k}_c$ – change values with respect to each other based on the value of k_{QPM}. When the diabatic trajectories cross, any state in those two modes will undergo avoided crossings and end up in the other mode. The efficiency of this process depends on the pumping and the k_{QPM} slope, as given by the Landau–Zener formula. Fig. 2.2d gives an analogy in terms of physical beamsplitters, with a given transmission and reflection values, phase plates imparting a given phase, and distance imparting a given group delay.

Fig. 2.2e represents how a two-mode squeezed vacuum state would evolve throughout the AFC process, in the frequency domain. Two-mode squeezed vacuum is made up of a symmetric

and antisymmetric supermode of the frequencies ω_a and ω_b. The fastest mode a is converted into the slowest mode c with (as close as possible to) unit efficiency. The next conversion, between b, c is driven to 50% conversion efficiency (a balanced beamsplitter), and the phase of pump B must be calibrated with respect to pump A. Due to the phase difference in the symmetric and antisymmetric supermodes, one state ends up completely in c and one in b. Fig. 2.2e represents the same process in the time domain. Modes a, b begin with a separation in time. After mode a converts to c, mode b catches up, at which point the b, c conversion occurs, which separates the underlying states. Fig. 2.2g is a simulation of the joint spectral intensity, or photon number covariance, of a fully entangled, two mode-squeezed state given as the input to AFC. The output, shown below, demonstrates the off-diagonal correlations moving into the matrix diagonal, indicating independence between the states.

Single mode squeezing of hybridized modes

We can generalize the results of the previous section by symmetrizing the OPA process to make it more robust, as proposed in Ref. [7]. Distinguishability in the OPA process can arise from differences in the dispersion of its two modes. Ref. [7] proposed squeezing via two passes in an OPA while swapping the modes in between, and showed improved single-mode performance. We can extend this idea further and consider multiple passes through an OPA, alternating with mode swaps (unit-efficiency AFC), as shown in Fig 2.1b. In the limit of many short steps, this amounts to simultaneous OPA and AFC.

The details are discussed in detail in Appendix C. In summary, we can think of the physics in the language of perturbation theory: a strong driving field in the SFG process dictates the eigenmodes of the system. These are the hybridizations of the two frequency modes a, b: $a \pm b$. If

we consider the OPA process as a perturbation, it will act on the eigenmodes of the system, which happen to be its own. In addition, it will split the eigenvalues of the degenerate $a \pm b$ modes, so that these are parametrically amplified under different quasi-phase matching (QPM) values.

Fig. 2.3 illustrates this process. Fig. 2.3a shows the interplay between the sum frequency generation and parametric amplification processes. A hypothetical state embedded in the frequencies of a, i.e. ω_a, is brought to an equal superposition of a, b, and therefore spans both ω_a, ω_b. Given that these are the two modes of the OPA process, this enables two mode squeezing of the state with itself, or, more precisely, single-mode squeezing of the dressed state in the hybridized mode. After this, the state is brought back into a single mode, becoming a bare state once again.

Fig. 2.3b shows the QPM frequency that can implement this combined AFC-OPA process. The

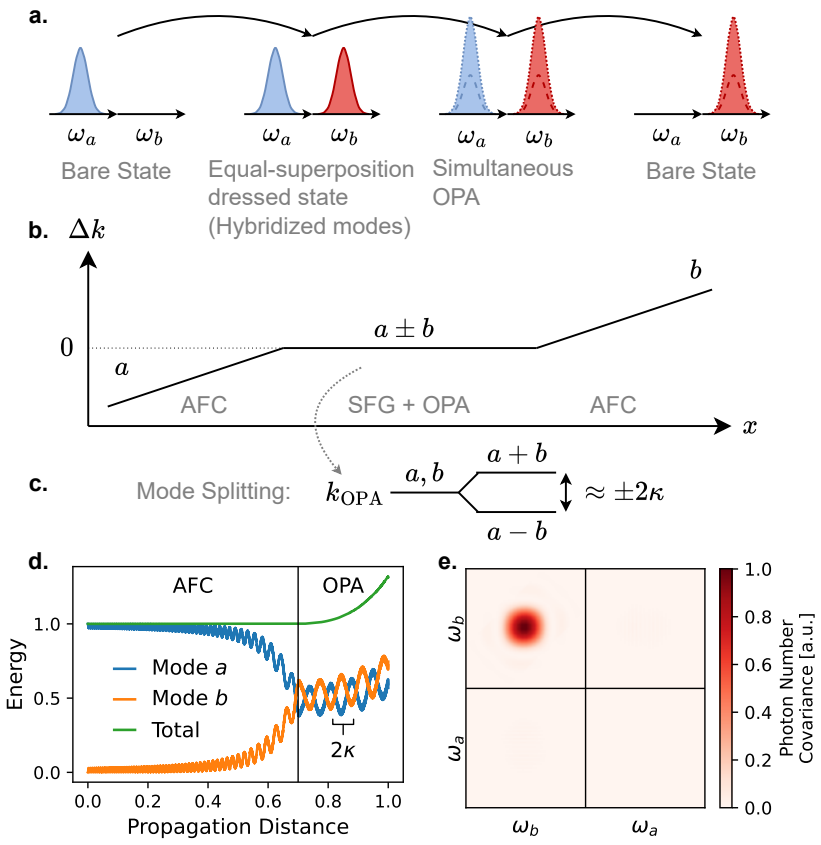

Figure 2.3: **Direct generation of single mode squeezing via AFC-enabled mode hybridization. a.** Frequency mixing of the proposed process. A state in mode a is input into the device. As the modes hybridize, by reducing the AFC detuning, a becomes an equal superposition of a, b. The AFC process is stalled at the halfway point, where the SFG process is phase-matched (zero detuning). A two-mode OPA process between modes a, b is driven simultaneously, and the hybridized $a \pm b$ modes may experience parametric gain. The AFC process is then continued, and the state finishes in b. (When performing vacuum squeezing, the initial frequency conversion, prior to squeezing, is unnecessary.) **b.** Diabatic trajectory of the state with respect to AFC detuning Δk. The AFC process begins highly detuned (large $|\Delta k|$), where a, b are effectively uncoupled. The detuning is brought to $\Delta k = 0$, where a, b are hybridized and held constant for some length. The detuning sweep is then continued towards large $|\Delta k|$, ending the process with uncoupled modes. **c.** Mode splitting in the OPA. The frequency of the hybridized modes deviate somewhat from a, b, causing a mode splitting between $a \pm b$. The difference in phase-matching k_{OPA} is approximately proportional to the magnitude of the coupling (pumping) between the modes κ. **d.** Single-mode simulation of the hybridization and parametric amplification process, for the first AFC and OPA regions. Here the process is seeded with energy in mode a. Approximately half the energy is converted to b prior to the OPA region, at which point the energy oscillates back and forth between modes. This additional oscillation frequency causes the mode splitting, which has to be compensated for in the OPA. (For vacuum squeezing, we would run this process backwards.) **e.** Simulated covariance matrix of the state. By using AFC in addition to two-mode squeezing, the final state is localized to one mode.

AFC process is started with a high detuning Δk, and brought to the SFG QPM frequency, i.e. $\Delta k = 0$. This QPM is then kept constant for some propagation length, and device is QPM'd for OPA simultaneously. Finally, the AFC process is continued (or reversed) to a large detuning value. Note that for vacuum squeezing, the initial AFC process is not necessary, since a optical unitary transformation does not affect the vacuum state.

Fig. 2.3d is a two mode simulation of the initial AFC and simultaneous SFG and OPA processes. Approximately half the amplitude of a signal initially in mode a is split into mode b. During the OPA process, the total signal is amplified, and the amplitude partially oscillates between a, b. This additional periodicity must be accounted for in the OPA QPM frequency, and it is dependent on the pump power of the AFC pump, as shown in Appendix C. The mode splitting is approximately

twice the magnitude of the pumping term in Eq. 2.1: $\pm 2\kappa$.

Fig. 2.3d represents the photon covariance matrix of vacuum squeezed in this manner. (a multimode version of the simulation in Fig. 2.3d, run in the reverse direction). While ostensibly fairly circularly symmetric, it is not quite single mode due to side lobes and other minor features. Apodization techniques could be used to improve single-mode behavior, but this is nontrivial, since the OPA and SFG must be simultaneously phase-matched. It requires that the strength of the OPA interaction must be varied while keeping the strength of the SFG interaction constant. In addition, the phase-matching function that arises from mode hybridization is unusual, as it tends towards a circularly symmetric function in joint frequency space. This is also covered in Appendix C.

Mode trapping with a shaped pump

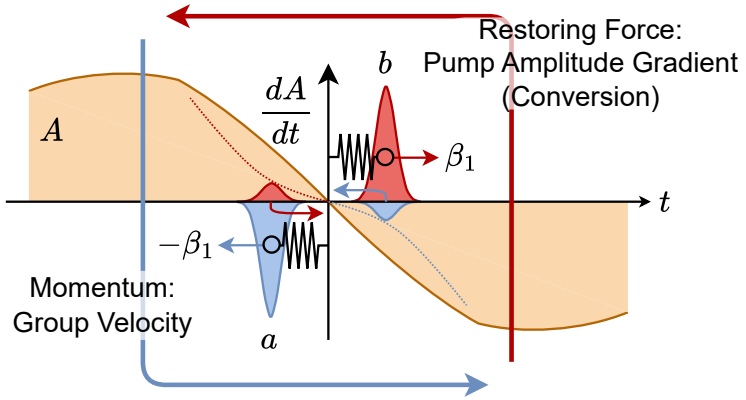

Figure 2.4: **Spectro-temporal mode trapping by frequency conversion.** This is achieved by pump shaping such that the amplitude (envelope) of the pump field A crosses through zero. The combination of temporal walk-off and frequency conversion between modes a, b results in an effective potential. With a linear pump amplitude, the system acts as a harmonic oscillator. The group velocity mismatch acts analogously to the momentum in an oscillator, such that wave-packets in frequency-modes a, b travel away from the center in opposite directions. The pump amplitude increases with the distance from the center, which acts as a restoring force, due to the increased greater back-conversion.

Until now, we have been considering a quasi-monochromatic pump for the frequency conversion processes enabling beamsplitting and hybridized squeezing. However, shaping the pump introduces remarkable physics, under the assumption that the group velocity of the pump is between that of the two signal modes.

In the stationary frame of the pump, the two signal modes a, b will walk-off in opposite directions (temporally). When a pulse is converted from one mode to the other, it will change its direction. By "bouncing" a pulse back and forth – by converting it each time it walks off by a given delay in one direction – we create a temporal trap. The end result is that the pump shape defines an effective potential. A linear pump field crossing zero will like act as a harmonic oscillator. This is covered in more detail in Appendix D.

This harmonic oscillator mechanism is illustrated in Fig. 2.4a. The group velocities of the two signal modes, the tendency for the pulses to walk off in one direction, are analogous to the momentum. The amplitude of the SFG pump field, and hence the strength of the conversion to the other mode, acts analogously to a restoring force.

Mode trapping might be an avenue to generating strictly single mode squeezing. It would appear that combining:

1. an SFG pump shape that corresponds to an anharmonic potential that supports only one mode;
2. and appropriately pumping the OPA process within this potential.

A Designing the AFC to compensate for time delay

Consider three frequency modes a, b, c. Their group velocity are assumed to be $v_a > v_b > v_c$ (where the group velocity is the inverse of the first-order propagation constant $v = \beta_1^{-1}$) such that the pulse in mode a first converts to c, and experiences a time delay with respect to b. Once the pulses in b and c overlap, the second conversion occurs. Let ΔT be the original delay between the two pulses in a and b at the first conversion point, which is due to the propagation length within the OPA (L_{OPA}) and within the AFC before the conversion point (L'_{AFC}):

$$\Delta T \approx \left(L_{\text{OPA}} + L'_{\text{AFC}}\right)\left(\beta_1^{(b)} - \beta_1^{(a)}\right),$$

then the distance between the two conversion points, $a \to c$ and $b \leftrightarrow c$, must be

$$L_{\text{AFC}}\left(\beta_1^{(c)} - \beta_1^{(b)}\right) = \Delta T.$$

Within this distance the quasi-phase matching for the AFC must change from $\Delta k_{(ac)} = k_p + k_a - k_c$ to $\Delta k_{(bc)} = k_p + k_b - k_c$ The simplest way to do this is by varying the QPM linearly to connect the two points. This works sufficiently well, however, as discussed in the next section, for broadband processes it is preferable to vary the slope according to the dispersion.

Finally, consider some error in the design, such that there is a deviation from the optimal length

$$L_{\text{AFC}} \to L_{\text{AFC}} + \delta L.$$

If modes a, b are at the same frequency (e.g. different polarization modes), then varying the pump wavelength (hence the central wavelength of mode c) can compensate for this error. The change in frequency affects k_p and k_c, hence the effective L'_{AFC} and ΔT for the new mode c and consequently L_{AFC}.

B Designing the slope for broadband conversion

We want to design the slope of the AFC such that the different wavelengths all experience the same phase and time delay. To achieve this, the conversion points for different wavelengths, occurring in different locations along the propagation axis of the crystal, must be spaced according to the dispersion.

The slope is defined as the rate of change in the quasi-phase matching frequency k over the propagation axis:

$$S(x) = \frac{dk}{dx}.$$

Let x_1 and x_2 be the two conversion points for the central frequencies, as discussed previously. Consider a frequency $\delta\omega$ away from the initial central frequency ω_0. Due to dispersion, it will experience a different wavenumber, which will result in a phase and time delay; this can be compensated for by propagation over a longer or shorter distance. Let $\delta k_1 = \Delta k(\delta\omega + \omega_0) - \Delta k(\omega_0)$, and similarly δk_2, be the difference in the wavenumbers involved in the first and second conversion. The overall phase delay ϕ (with respect to the central frequency, and which we wish to eliminate) will be the spatial integral of the wavenumber between the two conversion points, and its derivative is the time delay ΔT:

$$\begin{aligned}
\phi(\delta\omega) &= \int_0^{x_1(\delta\omega)} \delta k_1(\delta\omega)dx - \int_0^{x_2(\delta\omega)} \delta k_2(\delta\omega)dx \\
-\Delta T(\delta\omega) &= \frac{d}{d\omega}\left[\int_0^{x_1(\delta\omega)} \delta k_1(\delta\omega)dx - \int_0^{x_2(\delta\omega)} \delta k_2(\delta\omega)dx\right] \\
&= \int_0^{x_1} \frac{dk_1}{d\omega}dx + \delta k_1 \frac{dx_1}{d\omega}\bigg|_{\delta\omega} - \int_0^{x_2} \frac{dk_2}{d\omega}dx - \delta k_2 \frac{dx_2}{d\omega}\bigg|_{\delta\omega}.
\end{aligned}$$

These derivatives, $dx_i/d\omega$, depend on the slope, since $dx = dk_1/S_1$. For simplicity let us consider

the case of linear dispersion, where $\delta k_1 = \Delta\beta_1^{(1)}\delta\omega$, $\delta k_2 = \Delta\beta_1^{(2)}\delta\omega$. Therefore:

$$\frac{dx_1}{d\omega} = \left(\frac{dk_1}{dx_1}\right)^{-1}\frac{dk_1}{d\omega} = \frac{\Delta\beta_1^{(1)}}{S_1},\ \frac{dx_2}{d\omega} = \frac{\Delta\beta_1^{(2)}}{S_2}.$$

Hence, returning to our expression for the delay:

$$\begin{aligned}-\Delta T(\delta\omega) &= \int_0^{x_1}\Delta\beta_1^{(1)}dx + \Delta\beta_1^{(1)}\delta\omega\frac{dx_1}{d\omega} - \int_0^{x_2}\Delta\beta_1^{(2)}dx - \Delta\beta_1^{(2)}\delta\omega\frac{dx_2}{d\omega} + O(\delta\omega)\\ &= \int_0^{x_1}\Delta\beta_1^{(1)}dx - \int_0^{x_2}\Delta\beta_1^{(2)}dx + \left(\frac{{\Delta\beta_1^{(1)}}^2}{S_1} - \frac{{\Delta\beta_1^{(2)}}^2}{S_2}\right)\delta\omega.\end{aligned}$$

We need $\Delta T = 0$. Set:

$$\frac{S_1}{S_2} = \left(\frac{\Delta\beta_1^{(1)}}{\Delta\beta_2^{(2)}}\right)^2$$

and it remains be to be shown that:

$$\int_0^{x_1}\Delta\beta_1^{(1)}dx - \int_0^{x_2}\Delta\beta_1^{(2)}dx = 0.$$

By integrating the left-hand side:

$$\begin{aligned}\Delta\beta_1^{(1)}x_1 - \Delta\beta_1^{(2)}x_2 &= \Delta\beta_1^{(1)}\frac{dx_1}{dk}\frac{dk}{d\omega}\delta\omega - \Delta\beta_1^{(2)}\frac{dx_2}{dk}\frac{dk}{d\omega}\delta\omega\\ &= \left(\frac{{\Delta\beta_1^{(1)}}^2}{S_1} - \frac{{\Delta\beta_1^{(2)}}^2}{S_2}\right)\delta\omega = 0,\end{aligned}$$

where we used that:

$$x_i = \int\frac{dx_i}{d\omega}d\omega = \int\left(\frac{dk_i}{dx_i}\right)^{-1}\frac{dk_i}{d\omega}d\omega.$$

Hence $\Delta T(\delta\omega) = 0$ and $\phi(\delta\omega)$ is constant.

C Parametric amplification of hybridized modes

In this section, we shall describe in some detail the physics of the parametric amplification, or squeezing, alongside a simultaneous AFC process.

An OPA, which acts on two modes a and b, is described by the equations:

$$\frac{da}{dx} = i\gamma b^* \mathrm{e}^{i\Delta k_{\mathrm{OPA}} x}$$
$$\frac{db}{dx} = i\gamma a^* \mathrm{e}^{i\Delta k_{\mathrm{OPA}} x}$$

for some phase mismatch Δk_{OPA} and coupling γ. When phase-matched, i.e. $\Delta k_{\mathrm{OPA}} = 0$, the eigenstates are the sum and difference of the two modes: $(a \pm b)/\sqrt{2}$.

Similarly, the AFC can be thought to hybridize the modes, where the eigenstates adiabatically evolve from the bare to the dressed states and back (cite). The equations of motion are:

$$\frac{da}{dx} = i\kappa b \mathrm{e}^{-i\Delta k_{\mathrm{AFC}}(x) x}$$
$$\frac{db}{dx} = i\kappa^* a \mathrm{e}^{i\Delta k_{\mathrm{AFC}}(x) x}$$

which can be moved the into the rotating frame ($a \to a\exp(ik_{\mathrm{AFC}}z/2)$, $b \to b\exp(-ik_{\mathrm{AFC}}z/2)$) and written in the more intuitive form:

$$\frac{d}{dx}\begin{pmatrix} a \\ b \end{pmatrix} = i\begin{pmatrix} \frac{1}{2}k_{\mathrm{AFC}}(x) & \kappa \\ \kappa^* & -\frac{1}{2}k_{\mathrm{AFC}}(x) \end{pmatrix}\begin{pmatrix} a \\ b \end{pmatrix}$$

Indeed the eigenvalues of this Hamiltonian are

$$\pm\frac{1}{2}\sqrt{k_{\mathrm{AFC}}^2 + 4\kappa^2}$$

and when the phase-matching condition is met, $k_{\mathrm{AFC}}(z) = 0$, we obtain the same eigenstates as in the OPA. This implies that we can combine the AFC and the OPA, in order to squeeze the dressed states $(a \pm b)/\sqrt{2}$ and then adiabatically return them to the bare states, and perform an overall single-mode squeezing operation. This requires the AFC Hamiltonian to dominate, hence $\kappa \gg \gamma$.

Let us now consider the broadband, frequency-multimode case. We are interested in the case of a broadband OPA pump, but a monochromatic AFC pump. For simplicity, we consider the

linear dispersion case, where the wavenumbers of the two modes scale as:

$$k_a(\omega_0 + \delta\omega) = k_a(\omega_0) + \beta_{1a}\delta\omega$$

$$k_b(\omega_0 + \delta\omega) = k_b(\omega_0) + \beta_{1b}\delta\omega$$

Similarly to the previous section, we might expect that the phase-matching for the AFC and OPA, for a given frequency, must occur at the same location In other words that the phase-matching condition of the OPA should also be varied spatially: for any given pair $a(\omega_0 + \delta\omega)$ and $b(\omega_0 - \delta\omega)$, $k_{\text{AFC}} = 0$ and $k_{\text{OPA}} = 0$ should occur simultaneously, to avoid generating squeezed vacuum states with undesired, complicated, multimode spectro-temporal structure. As presented in the previous section, this condition requires

$$\begin{aligned}
\frac{dx_{\text{AFC}}}{d\omega} &= \frac{dx_{\text{OPA}}}{d\omega} \\
\left(\frac{dk_{\text{AFC}}}{dx_{\text{AFC}}}\right)^{-1} \frac{dk_{\text{AFC}}}{d\omega} &= \left(\frac{dk_{\text{OPA}}}{dx_{\text{OPA}}}\right)^{-1} \frac{dk_{\text{OPA}}}{d\omega} \\
\left(\frac{dk_{\text{AFC}}}{dx_{\text{AFC}}}\right)^{-1} (\beta_{1a} - \beta_{1b}) &= \left(\frac{dk_{\text{OPA}}}{dx_{\text{OPA}}}\right)^{-1} (\beta_{1a} + \beta_{1b})
\end{aligned}$$

where x represents the phase matching point as a function of ω. However, we can see that as long as we enforce the condition $\beta_{1a} = -\beta_{1b} = \beta_1$, any spatial variation is unnecessary (this condition is also required to conventionally obtain two-mode squeezing over equal bandwidths in both modes).

Therefore, write the AFC Hamiltonian for $\Delta k_{\text{AFC}} = 0$ and then transform it into the dressed

basis:

$$\mathcal{H}_{\text{AFC}}(\omega_i, \omega_i') = \begin{pmatrix} \beta_{1a}\omega\ \delta(\omega_a - \omega_a') & \kappa\ \delta(\omega_b - \omega_a') \\ \kappa^*\ \delta(\omega_b - \omega_b') & \beta_{1b}\omega\ \delta(\omega_b - \omega_b') \end{pmatrix}$$

$$\rightarrow \mathcal{H}_{\text{AFC}}(\omega, \omega') = \begin{pmatrix} \sqrt{\beta_1^2\omega^2 + \kappa^2}\ \delta(\omega - \omega') & \nvDash \\ \nvDash & -\sqrt{\beta_1^2\omega^2 + \kappa^2}\ \delta(\omega - \omega') \end{pmatrix}$$

(we include the Dirac delta function $\delta(\omega)$ to indicate that the AFC pump is monochromatic). The hybridized eigenstates are:

$$A = \frac{a+b}{\sqrt{2}},\ B = \frac{a-b}{\sqrt{2}}$$

and we can substitute these into the OPA Hamiltonian:

$$\begin{aligned} \mathcal{H}_{\text{OPA}} &= \gamma(\omega_a + \omega_b)a^\dagger(\omega_a)b^\dagger(\omega_b)\mathrm{e}^{i\Delta k_{\text{OPA}}(\omega_a,\omega_b)z} \\ &= \tfrac{1}{2}\gamma(\omega_a + \omega_b)\mathrm{e}^{i\Delta k_{\text{OPA}}z}\left(A^\dagger(\omega)\exp\left(-iz\sqrt{\beta_1^2\omega^2 + \kappa^2}\right) + B^\dagger(\omega)\exp\left(iz\sqrt{\beta_1^2\omega^2 + \kappa^2}\right)\right) \\ &\qquad \left(A^\dagger(\omega')\exp\left(-iz\sqrt{\beta_1^2\omega'^2 + \kappa^2}\right) + B^\dagger(\omega')\exp\left(iz\sqrt{\beta_1^2\omega'^2 + \kappa^2}\right)\right) \end{aligned}$$

Consider, for example, the $A^\dagger(\omega)A^\dagger(\omega')$ term. The term rotates as

$$k_{\text{tot}}(\omega, \omega') = \Delta k_{\text{OPA}} - \sqrt{\beta^2\omega^2 + \kappa^2} - \sqrt{\beta^2\omega'^2 + \kappa^2}$$

which depends on the pump strength κ. Hence, we would compensate in the phase matching condition for the central frequency:

$$\Delta k_{\text{OPA}} = 2|\kappa|.$$

(Experimentally we would design a device for some value of κ and sweep the pump strength until the phase matching condition is met.) Notice also that there is a level splitting: the $B^\dagger(\omega)B^\dagger(\omega')$ term in the Hamiltonian would require $-2|\kappa|$, hence it will not be phase matched. When $\kappa/\beta_1 \gg$

ω, ω', the phase rotation term is:

$$\begin{aligned} k_{\text{tot}}(\omega, \omega') &= 2|\kappa| - \sqrt{\beta_1^2 \omega^2 + \kappa^2} - \sqrt{\beta_1^2 \omega'^2 + \kappa^2} \\ &\approx -\frac{\beta_1^2}{2\kappa} \left(\omega^2 + \omega'^2\right) \end{aligned}$$

It is fascinating that k_{tot} has circular symmetry (while the quadratic approximation holds) and, therefore, any phase matching function will introduce no momentum-conservation-related spectral correlations. However, energy conservation will generally introduce spectral correlations. We can thus expect to be able to engineer single mode squeezing (or approximately thereof) with this method if the effects of these correlations can be minimized. For example, if the OPA pump bandwidth is broader than the phase-matching bandwidth, and spectrally flat.

D Pump shaping for mode trapping

The previous section considered the behavior of two spectral modes under the influence of a monochromatic linearly coupling the two. Even more interesting scenario arises when we consider two pump frequencies, or more generally, shaped broadband pulses. Consider the coupled wave equations as before, but with a time dependent pump:

$$\begin{aligned} \frac{da}{dx} &= i\kappa(t) b(t) \mathrm{e}^{-i\Delta k_{\text{AFC}}(x)x} \\ \frac{db}{dx} &= i\kappa^*(t) a(t) \mathrm{e}^{i\Delta k_{\text{AFC}}(x)x}. \end{aligned}$$

Moving into the rotating frame, and expanding the phase mismatch about the central frequency:

$$\begin{aligned} \frac{da}{dx} &= i\kappa(t) b(t) + i\left(\beta_{0a} + i\beta_{1a}\frac{d}{dt} - \frac{1}{2}\beta_{2a}\frac{d^2}{dt^2}\ldots\right) a(t) \\ \frac{db}{dx} &= i\kappa^*(t) a(t) + i\left(\beta_{0b} + i\beta_{1b}\frac{d}{dt} - \frac{1}{2}\beta_{2b}\frac{d^2}{dt^2}\ldots\right) b(t). \end{aligned}$$

(the Fourier-transform of the dispersion expansion replaces the frequency with the differential operator $\omega \to id/dt$).

If we consider the phase-matched and anti-symmetric linear dispersion case, and change $\kappa \to i\kappa$, we simplify to:

$$\frac{da}{dx} = \kappa(t)b(t) + \beta_1 \frac{d}{dt}a(t)$$
$$\frac{db}{dx} = -\kappa^*(t)a(t) - \beta_1 \frac{d}{dt}b(t)$$

for which we would like to find the stationary or eigenstates. For this we change to a time-independent (Schrödinger) equation, using as an ansatz that the time evolution is simply a phase rotation $\exp(-iEt)$:

$$-iEa = \kappa b + \beta_1 \frac{d}{dt}a$$
$$-iEb = -\kappa^* a - \beta_1 \frac{d}{dt}b$$

and taking superpositions (assuming real κ:

$$E(a+b) = -i\kappa(a-b) + i\beta_1 \frac{d}{dt}(a-b) = -i\left(\kappa - \beta_1 \frac{d}{dt}\right)(a-b) = -iA^\dagger(a-b)$$
$$E(a-b) = i\kappa(a+b) + i\beta_1 \frac{d}{dt}(a+b) = i\left(\kappa + \beta_1 \frac{d}{dt}\right)(a+b) = iA(a+b)$$

Note the resemblance to the quantum harmonic oscillator formalism that arises if we set $\kappa(t) \propto t$. κ will then act as the restoring force term and $-i\beta_1 d/dt$ will act as the inertial term, and $A, A^\dagger$ are

creation and annihilation operators. Indeed:

$$\begin{aligned}
E^2(a+b) &= AA^\dagger(a-b) \\
&= \left(\kappa + \beta_1 \frac{d}{dt}\right)\left(\kappa - \beta_1 \frac{d}{dt}\right)(a-b) \\
&= \left(\kappa^2 - \beta_1^2 \frac{d^2}{dt^2} + \beta_1 \frac{d\kappa}{dt}\right)(a-b) \\
E^2(a-b) &= A^\dagger A(a+b) \\
&= \left(\kappa - \beta_1 \frac{d}{dt}\right)\left(\kappa + \beta_1 \frac{d}{dt}\right)(a-b) \\
&= \left(\kappa^2 - \beta_1^2 \frac{d^2}{dt^2} - \beta_1 \frac{d\kappa}{dt}\right)(a-b)
\end{aligned}$$

which confirms that $a+b$ and $a-b$ are stationary states of the system. The raising operator $A^\dagger$ maps $a-b \to a+b$ and, inversely, the lowering operator A maps $a+b \to a-b$. It also tells us that the energy gap is $2\beta_1 d\kappa/dt$, which is constant given linear κ. Lastly, we infer that $a+b$ and $a-b$ must be Hermite–Gauss modes (but not necessarily a, b individually).

There are a few ways to make $\kappa(t) \propto t$. The first is a two tone AFC; the sinusoidal temporal beating of two monochromatic pumps will be linear near the nodes. This could be realized by modulation of a monochromatic pump. However, because of the periodic nature of the potential, these are likely to form Bloch waves rather than purely localized states. A second possibility is (a pulse resembling) the first Hermite–Gauss function, which is linear at the center. This is in principle feasible with pulse shaping. However, the Hermite–Gauss function decays too rapidly to formally contain a bound state (with normalizable wavefunction) in the center region. Mathematically, a pump resembling a slowly decaying tanh- or sigmoid-like function would be appropriate.

E A brief review of pump spectrum and phase-matching engineering for squeezed state generation

Squeezed vacuum states are generated by parametric amplification, which generally follows the formula:

$$\frac{da(\omega,z)}{dz} = iA(\omega+\omega')g(z)a^\dagger(\omega',z)\exp(i\Delta k(\omega,\omega')z)$$

where and Δk is a phase rotation term between modes at two given frequencies. The nonlinearity, or coupling, is assumed to be separable in space and frequency: $g(z)$ is the effective nonlinearity as a function of propagation position; $A(\omega)$ is the frequency-dependent coupling, due to the pump spectrum. Generally, a may be a vector comprised of modes due to various degrees of freedom in addition to frequency (e.g. polarization, space).

By integrating the equation, we obtain the Green's function:

$$a(\omega,z=L) = \int d\omega' \left[C(\omega,\omega')a(z=0) + S(\omega,\omega')a^\dagger(z=0)\right]$$

or in alternative notation:

$$\begin{pmatrix} a \\ a^\dagger \end{pmatrix} = \begin{pmatrix} C & S \\ S^* & C^* \end{pmatrix} \begin{pmatrix} a \\ a^\dagger \end{pmatrix}.$$

The spectral correlations for vacuum input can then be written as:

$$\frac{1}{2}\begin{pmatrix} \langle a(\omega)a^\dagger(\omega')\rangle & \langle a(\omega)a(\omega')\rangle \\ \langle a^\dagger(\omega)a^\dagger(\omega')\rangle & \langle a(\omega)^\dagger a(\omega')\rangle \end{pmatrix} + h.c. = \frac{1}{2}\begin{pmatrix} SS^\dagger + CC^\dagger & CS^\intercal + SC^\intercal \\ C^*S^\dagger + S^*C^\dagger & S^*S^\intercal + C^*C^\intercal \end{pmatrix}$$
$$= \begin{pmatrix} SS^\dagger + I/2 & (CS^\intercal + SC^\intercal)/2 \\ (C^*S^\dagger + S^*C^\dagger)/2 & S^*S^\intercal + I/2 \end{pmatrix}.$$

Decomposition of this matrix reveals the underlying squeezed vacuum modes.

It is common practice to take a first order approximation of the differential equation:

$$a(\omega, z = L) \approx a(\omega, z = 0) \exp(ik(\omega)L) + ia^\dagger(\omega', z = 0)A(\omega + \omega')\Phi(\Delta k(\omega, \omega'))$$
$$\Phi(\Delta k) = \int_0^L dz\, g(z) \exp(i\Delta k z)$$

where we refer to Φ as the phase matching function (PMF), which is effectively the Fourier transform of $g(z)$. (Often the approximation is made via exponentiation followed by truncation of the time-ordering expansion, but this is equivalent.) Hence,

$$C \approx \delta(\omega - \omega') \exp(ik(\omega)L)$$
$$S \approx iA(\omega + \omega')\Phi(\Delta k(\omega, \omega')).$$

Since C essentially the identity under this approximation, we can analyze the system by inspecting S.

It has been shown that manipulating A and Φ appropriately can yield approximately two-mode squeezing, referred to as a "spectrally separable" state. To minimize the rank of S, one must notice that A tends to generate anti-correlations between modes in ω and ω'. Therefore, Φ can be designed to introduce equal and opposite correlations. Both may be designed to be Gaussian:

$$A \propto \exp\left(\frac{(\omega + \omega')^2}{2\sigma_p^2} + ic(\omega + \omega')^2\right)$$
$$\Phi \propto \exp\left(\frac{\sigma_g^2 \Delta k(\omega, \omega')^2}{2} + i\frac{\Delta k(\omega, \omega')L}{2}\right)$$

where σ_p and σ_g are the spectral width of the pump and spatial width of the nonlinearity $g(z)$ in real space. The pump has an additional chirp term c and the PMF has a translation phase as it is centered at $L/2$. The phase mismatch is expanded with respect to the frequency:

$$\begin{aligned}\Delta k(\omega, \omega') &= k(\omega) + k'(\omega') - k_p(\omega + \omega') \\ &= \left(\beta_1 \omega + O(\omega^2)\right) + \left(\beta_1' \omega' + O(\omega'^2)\right) - \left(\beta_{1p}(\omega + \omega') + \tfrac{1}{2}\beta_{2p}(\omega + \omega')^2 + O((\omega + \omega')^3)\right)\end{aligned}$$

assuming that the process is phase-matched. To remove all spectral correlations from the product $A\Phi$ means to make it separable in ω and ω', hence – to leading order – have any $\omega\omega'$ product terms vanish. By evaluating the exponentiated terms in $A\Phi$ we may rederive the two separability conditions on the widths and spectral phase:

$$\sigma_p^2\sigma_g^2(\beta_1 - \beta_{1p})(\beta_1' - \beta_{1p}) = -1$$

$$c = -\frac{1}{2}\beta_{2p}L.$$

To satisfy the first equation, the group velocity condition requires $\beta_1 > \beta_{1p} > \beta_1'$ or vice versa. Similarly, to have both modes have the same bandwidth requires symmetry: the group velocities must be equal and opposite relative to the pump: $\beta_1 - \beta_{1p} = \beta_{1p} - \beta_1'$. The second equation implies that the pump must be unchirped at the center of the crystal for best performance.

Finally, we must not forget that higher-order effects will play a role as the amount of gain increases.

CHAPTER 3

FOCUSING ON BANDWIDTH: ACHROMATIC METALENS LIMITS

This work was done together with Francesco Monticone [126].

Metalenses have shown great promise in their ability to function as ultracompact optical systems for focusing and imaging. Remarkably, several designs have been recently demonstrated that operate over a large range of frequencies with minimized chromatic aberrations, potentially paving the way for ultrathin achromatic optics. Here, we derive fundamental bandwidth limits that apply to broadband optical metalenses, regardless of their implementation. Specifically, we discuss how the product between achievable time delay and bandwidth is limited in any time-invariant system, and we apply well-established bounds on this product to a general focusing system. We then show that all metalenses designed thus far obey the appropriate bandwidth limit. The derived physical bounds provide a useful metric to compare and assess the performance of different devices, and they offer fundamental insight into how to design better broadband metalenses.

The field of metasurfaces holds the promise of a revolution in many areas of optics and photonics. In principle, any optical system may be made flat and compact by replacing the conventional optics with ultrathin devices, with great potential benefits in terms of size, cost, and ease of fabrication [127–129]. While metasurfaces can achieve arbitrary wavefront transformations and may even be used for optical wave-based computing [130, 131], "metalenses" specifically designed for focusing and imaging represent one of the most important classes of metasurfaces for practical applications. One of the main challenges in this context is the realization of thin metalenses operating over a broad wavelength range, with minimized chromatic aberrations. In conventional

optics, it is possible to stack various lenses to correct chromatic aberrations [132], but at the price of making the overall system more bulky and costly. It is therefore remarkable that, in recent years, different groups have demonstrated metalenses with a fixed focal length over a large range of wavelengths, some even surpassing the achromatic performance of conventional lens systems (at least for normal incidence) [133–148].

Regardless of its implementation, a metalens achieves focusing by changing the phase of an incoming plane wave, with a phase profile that must vary radially according to the following equation [127]:

$$\varphi(r,\omega) = -\frac{\omega}{c}\left(\sqrt{F^2+r^2} - F\right), \tag{3.1}$$

where ω, F, r and c are the angular frequency, focal length, radial coordinate and speed of light, respectively. In the general case, a spatial- and frequency-dependent phase profile, as in (3.1), can be Taylor expanded around a central frequency ω_c:

$$\varphi(r,\omega) = \varphi(r,\omega_c) + (\omega-\omega_c)\left.\frac{\partial\varphi(r,\omega)}{\partial\omega}\right|_{\omega=\omega_c} + \frac{1}{2}(\omega-\omega_c)^2\left.\frac{\partial^2\varphi(r,\omega)}{\partial\omega^2}\right|_{\omega=\omega_c} + \dots \tag{3.2}$$

where the latter two terms are the group delay and the group-delay dispersion. As discussed by Chen et al. [133], when the focal length F is frequency independent, (3.2) contains no higher-order terms than the linear one. Thus, to realize a perfectly achromatic lens, the design should implement (i) a suitable frequency-independent phase pattern $\varphi(r,\omega_c)$, (ii) a spatial pattern of group delay, and (iii) zero group-delay dispersion and higher-order terms. We also note that, while here we focus on metalenses for normal incidence, similar considerations apply to different phase functions in other metasurface devices (e.g., broadband beam deflection and splitting [149, 150]).

Early examples of optical metalenses were based on deeply subwavelength "meta-atoms" (e.g. plasmonic dipole nano-antennas) operating near a scattering resonance to achieve the phase delay

$\varphi(r, \omega_c)$ over the smallest possible thickness (a fraction of a wavelength), without any considerations of the linear and higher-order terms in (3.2). While this strategy allows realizing arbitrarily thin metasurfaces, these devices were highly dispersive with large chromatic aberrations, due to their resonant nature, and could only operate at either a single frequency or a discrete set of frequencies [127–129]. In contrast, the most recent designs at the time of writing have employed relatively thicker meta-structures (still on the order of a wavelength) that function essentially as microscopic waveguide segments. The waveguiding approach does not depend on the phase delay obtained through near-resonant light interaction with a scatterer, but rather on the *true time delay* obtained via guided-wave propagation, thus allowing significantly larger bandwidths. Conceptually, this new approach is more similar to early examples of flat lenses at microwave frequencies, e.g., [151], than to the first versions of modern optical metasurfaces based on resonant meta-atoms.

While the results obtained in recent works on broadband metalenses are remarkable, here we argue that there exists a strict physical bound on the chromatic properties of a metalens, which stems from the fact that it is not possible to impart an arbitrary group delay to a signal independently of its bandwidth. Indeed, the delay-bandwidth product is limited in any linear, time-invariant system, as recognized in several works, [152–154], and is related to the thickness of the device. Based on this concept, in the following section we derive fundamental limits on the bandwidth of achromatic metalenses, and assess the performance of various existing designs against these limits.

Results

Time-bandwidth products — Some attempts at identifying limits on the bandwidth of specific metalens designs have been recently made. For example, Shrestha et al. [136] have derived a bound on metalens bandwidths based on the range of dispersion properties covered by a meta-structure library, and Fathnan and Powell [155, 156] have derived bandwidth limits on low-frequency metasurfaces composed of printed-circuit impedance sheets. Here, instead, we are interested in a fundamental limit, applicable in general to any metalens, regardless of its specific implementation. With this goal in mind, we turn to the concept of delay-bandwidth, or time-bandwidth, product (TBP): the TBP of a device (a cavity, waveguide, etc.) is the product of the time delay, or interaction time, ΔT, experienced by the signal, and the signal bandwidth $\Delta\omega$. Wave physics imposes an upper bound on this quantity, which can be generally written as

$$\Delta T \, \Delta\omega \leq \kappa, \tag{3.3}$$

where κ is a dimensionless quantity. Bounds on the time-bandwidth product have been studied extensively in the field of slow light [152–154]. In particular, as discussed below, different bounds have been derived in the literature under different assumptions, but κ always depends on some general properties of the device, for example its length and refractive-index contrast of the materials involved.

In order to apply the concept of TBP and the associated bounds to our problem, we treat a metasurface lens as composed of one-dimensional slow-light devices or delay lines. More specifically, we consider a rotationally symmetric radial array, or continuum, of delay-line buffers, such that the incident wave is delayed as a function of radius, as illustrated in Fig. 3.1. According to (3.2), each delay-line buffer must impart a suitable group delay, dispersionless over the given

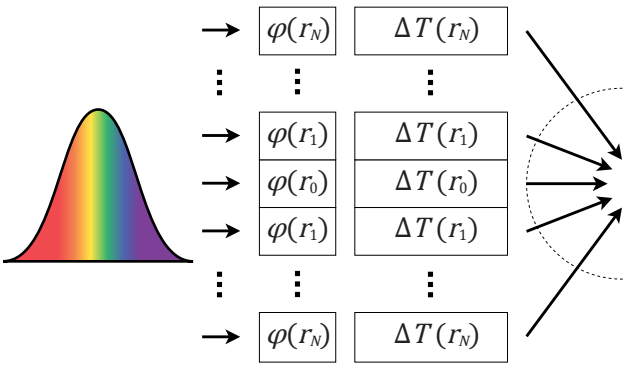

Figure 3.1: Delay-line model of a thin broadband metalens. Radially arranged delay lines provide a broadband signal the necessary group delay $\Delta T(r)$ to compensate for the difference in arrival times at the focus, while the phase pattern $\varphi(r)$ creates a spherical wavefront according to Eqs. (3.1) and (3.2).

band, to compensate for the difference in the arrival times of wavepackets at the focus. The lens must also impart a frequency-independent phase pattern, $\varphi(r, \omega_c)$, to create a spherical wavefront at the output. This phase pattern can be implemented independently of the group-delay requirement, using, for example, the concept of geometric phase, as shown in Ref. [133]. We would like to note that the 1D model in Fig. 3.1 is an approximation since a metasurface with finite thickness is not strictly a one-dimensional device; however, we expect that light normally incident on metasurfaces of thicknesses of the order of one wavelength would acquire time delay predominantly through longitudinal propagation, with little propagation along the lateral (radial) direction. For this reason, in what follows, we only consider metasurfaces with thickness smaller than about five free-space wavelengths. We further discuss this approximation and its implications in the Discussion and Conclusion section.

Consider a lens with radius R and focal distance F. From (3.1) and (3.2), the required relative

group delay imposed by the lens at a radial position $r \leq R$ is

$$\Delta T(r) = \frac{\partial \varphi}{\partial \omega}(r) - \frac{\partial \varphi}{\partial \omega}(R) \tag{3.4}$$

$$= \frac{1}{c}\left(\sqrt{F^2 + R^2} - \sqrt{F^2 + r^2}\right). \tag{3.5}$$

(In most cases, the group delay is equal to the actual time delay experienced by the signal, except in the presence of anomalous dispersion near resonances, which is, however, not a case of interest in this context, due to the strong absorption that unavoidably accompanies anomalous dispersion in passive systems [157].) The greatest delay is required at the center ($r = 0$) to compensate for the additional time taken by a signal arriving from the edge ($r = R$), such that the lens design must achieve

$$\Delta T_{\text{max}} = \frac{F}{c}\left(\sqrt{1 + (R/F)^2} - 1\right). \tag{3.6}$$

This defines our required time delay in the time-bandwidth product in (3.3).

Then, using the numerical aperture definition

$$\text{NA} = n_b \sin\theta = n_b \sin\left[\arctan\left(\frac{R}{F}\right)\right], \tag{3.7}$$

where n_b is the background refractive index, and the identity $1 + \tan^2(\arcsin x) = 1/(1 - x^2)$, we can use (3.3) and (3.6) to set a limit on the lens' bandwidth based on its numerical aperture (NA) and geometrical properties:

$$\Delta\omega \leq \frac{\kappa c}{F\left(\sqrt{1 + (R/F)^2} - 1\right)} = \frac{\kappa c\sqrt{1 - (\text{NA}/n_b)^2}}{F\left(1 - \sqrt{1 - (\text{NA}/n_b)^2}\right)}. \tag{3.8}$$

We note that the form of this limit is consistent with the bandwidth bound derived in [155] based on different considerations (Foster's reactance theorem) for the case of metasurfaces composed of impedance sheets. Our results, however, are more general, and apply to any type of metalenses, as we discuss below.

As mentioned above, different values of the upper bound κ have been derived for different general classes of devices. Thus, depending on the type of metasurface (whether it is based on resonant meta-atoms or waveguiding structures), we can apply the appropriate TBP bound and derive the relevant bandwidth limit. We now identify three relevant cases, covering all types of metasurfaces.

(i) If the metasurface has deeply subwavelength thickness, the only way to impart the necessary phase/time delay to incoming light is by interaction with resonant scattering meta-atoms. In this case, coupled-mode theory provides a geometry- and material-independent time-bandwidth product for a single-mode resonator (e.g., see [158]):

$$\kappa = 2. \tag{3.9}$$

In this case, (3.3) becomes an equality and it may also be written in terms of the Q factor of the resonant meta-atoms, $\Delta T = 2Q/\omega_c$, as recognized in Refs. [159, 160]. While the following goes beyond the scope of the present work, we also note that this case could be generalized to account for more than one resonator, as in the case of overlapped electric and magnetic dipole resonances used in Huygens' metasurfaces [155, 161–163]. However, the bandwidth bounds are not expected to significantly improve. In addition, while electric-dipole resonators can be made infinitesimally thin (e.g., printed dipole antennas), a magnetic-dipole resonator always requires a non-zero thickness, since a non-zero volume is necessary to establish a circulation of (conduction or polarization) current supporting a non-zero magnetic dipole moment [157].

(ii) For thick metasurfaces based on inclusions acting as waveguides, the previous limit clearly does not apply, since wave-guiding structures cannot be treated as individual resonators. Tucker et al. [153] provide a generally applicable time-bandwidth limit, valid for any one-dimensional, lossless, dielectric device that may be treated as a waveguide (the limit is strictly valid only if the

fractional bandwidth is not too large, i.e., smaller than unity). The value of the upper bound κ is given by

$$\kappa = 2\pi \frac{L}{\lambda_c}(n_{\text{max}} - n_{\text{min}}), \tag{3.10}$$

where n_{max} and n_{min} are the maximum and minimum *effective* refractive indices of the device. This effective index $n(\omega)$ is defined by the dispersion relation for the mode of interest in the structure, $\beta(\omega) = \omega n(\omega)/c$, as if the structure was homogeneous. $n(\omega)$, n_{max} and n_{min} are generally different from the material indices that make up the device. However, in the case of a one-dimensional dielectric waveguide segment (or coupled segments, as in [133]), which is the case of interest for most modern metasurfaces, we can take n_{max} and n_{min} as the refractive index of the dielectric material composing the waveguide and of the surrounding medium, respectively, because the guided-mode dispersion converges to the light line of the low-index material at low frequency, and to the light line of the high-index material at high frequency. We thus replace the difference term in (3.10) with $\Delta n = n_{\text{max}} - n_b$.

(iii) Finally, Miller [152] provides a similar, but much more general, time-bandwidth limit that is valid for a very broad class of one-dimensional structures (not necessarily dielectric) acting as delay lines:

$$\kappa = \frac{\pi}{\sqrt{3}} \frac{L}{\lambda_c} \eta_{\text{max}}, \tag{3.11}$$

where $\eta_{\text{max}} = |(\varepsilon_{\text{max}} - \varepsilon_b)/\varepsilon_b|$ is the device's maximum contrast in relative permittivity, with respect to the surrounding medium's permittivity ε_b, at any frequency within the band of interest and at any position within the structure. The limit is very general, as it is independent of the device design, and is not based on the simplifying assumptions used in Tucker's limit (lossless dielectric materials and well-defined group velocity). The limit strictly applies if the device length $L \gg \lambda_c$, where λ_c is the band-center wavelength in the background medium, and if the fractional

bandwidth is not too large. However, in practice, we have verified that, if L is just few times larger than the longest wavelength in the device, Miller's limit seems to apply, that is, it is consistent with Tucker's limit (which has no assumptions on length). If they both apply, Miller's limit is close to Tucker's, and exceeds it to some degree if $\varepsilon_{\max} \gtrapprox 6$.

These bounds on the time-bandwidth product, within their limits of applicability, may be combined with (3.8) to obtain an upper bound on the bandwidth of achromatic metalenses. Essentially all types of metalenses, for any thickness (smaller than a few wavelengths) and material composition, are covered by the three TBP bounds outlined above, leading to the following bandwidth limits:

(i) for ultra-thin metasurfaces based on resonant meta-atoms (single resonance) [from (3.9)],

$$\Delta\omega \leq \frac{2c}{F}\Theta\left(\frac{\mathrm{NA}}{n_b}\right), \tag{3.12}$$

(ii) for waveguide-based dielectric transparent metasurfaces [from (3.10)],

$$\Delta\omega \leq \omega_c \frac{L\Delta n}{F}\Theta\left(\frac{\mathrm{NA}}{n_b}\right), \tag{3.13}$$

(iii) for generic metasurfaces (not necessarily dielectric and lossless) of thickness larger than the wavelength [from (3.11)],

$$\Delta\omega \leq \frac{\omega_c}{2\sqrt{3}} \frac{L\eta_{\max}}{F}\Theta\left(\frac{\mathrm{NA}}{n_b}\right), \tag{3.14}$$

where we replaced $\omega_c = 2\pi c/\lambda_c$ and

$$\Theta\left(\frac{\mathrm{NA}}{n_b}\right) = \frac{\sqrt{1-(\mathrm{NA}/n_b)^2}}{1-\sqrt{1-(\mathrm{NA}/n_b)^2}}. \tag{3.15}$$

We compared these bandwidth limits to various broadband metalens designs available in the literature. Comparisons are shown in Fig. 3.2, using suitably normalized quantities, and are tab-

ulated in Table 3.1. What immediately stands out is that the limits correctly predict the expected performance trend: for larger numerical aperture the achievable bandwidth shrinks, because the required maximum time delay, $\Delta T_{\max}$ in (3.6), rapidly increases (and diverges at $\mathrm{NA}/n_b = 1$).

Not surprisingly, as seen in Fig. 3.2(a), only few thin, subwavelength, metalenses obey the bandwidth limit based on the single-resonator TBP given in (3.9). Instead, all the metalens designs obey our limits based on Tucker's or Miller's TBP (see Fig. 3.2(b) and Table 1), including recent ultrabroadband metalenses obtained using free-form all-area optimization and inverse design [139].

At this point, it is important to note that, although all the considered designs claim achromatic performance, some have non-negligible focal length variations, or do not disclose the exact field profile at the focal plane and the associated level of monochromatic aberrations. The focal field profile is relevant because the bandwidth limit derivation above assumes a diffraction-limited lens with no aberrations, i.e., Strehl ratio $S = 1$. The Strehl ratio is a measure of the wavefront aberration, defined as the ratio of the peak focal spot intensity to the maximum attainable intensity of an ideal lens. A metalens that does not achieve diffraction-limited focusing with $S = 1$ across the nominal operational bandwidth is not implementing the phase and time-delay profiles assumed above exactly; hence, it may surpass the bounds since the requirements are somewhat relaxed.

To quantify the effect of aberrations on our bandwidth bounds, we assume that the aberrations are not too large, which is the scenario of interest for imaging applications. In this case, the Strehl ratio is approximately independent of the nature of the aberration and, according to the "extended Maréchal approximation," it can be estimated from the variance of the wavefront deformation

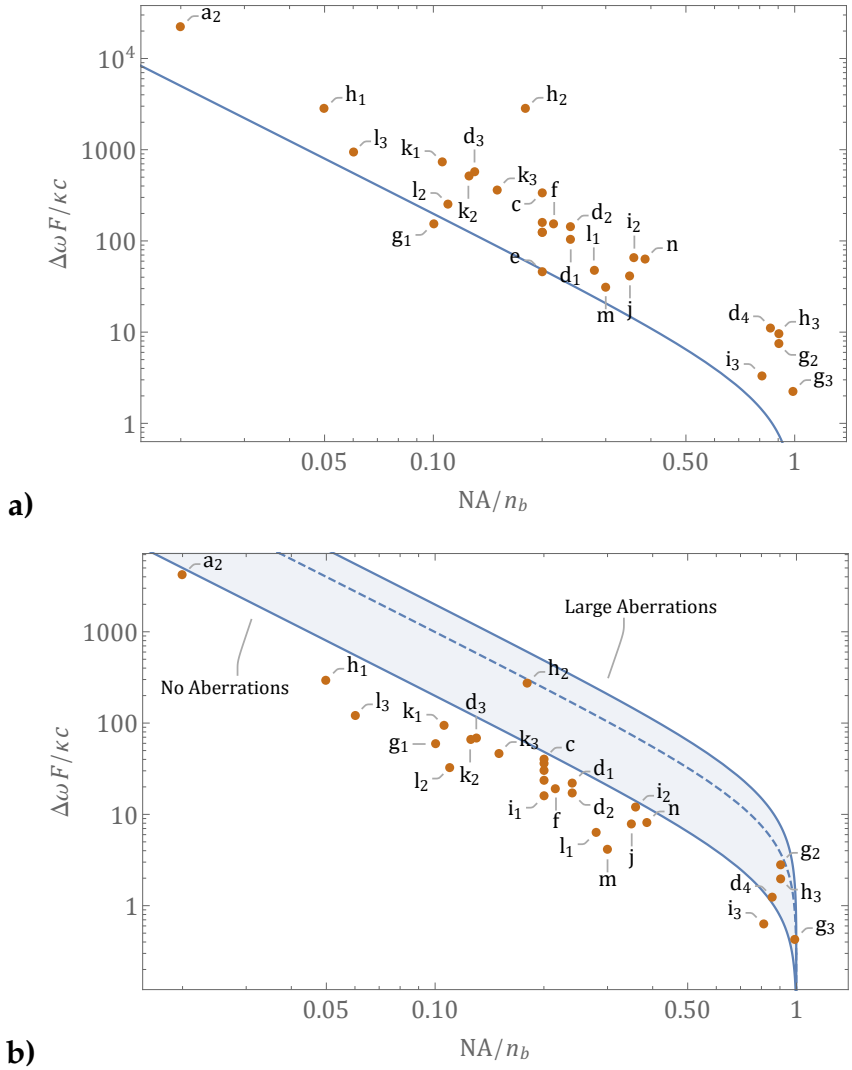

Figure 3.2: Comparisons of published achromatic metalens designs against the derived bandwidth limits. (a) Limit based on the single-resonator TBP bound, given by (3.12). Not surprisingly, most data points exceed this bound except for some thin devices. (b) Limit based on Tucker's TBP bound, given by (3.13). Each data point in the plots represent a single design, with each label corresponding to a specific row of Table 3.1. The performance of each metalens is represented in terms of numerical aperture and bandwidth. In order to compare vastly different designs against the bandwidth bounds, the bandwidths are normalized by c, F and the corresponding κ (see (3.8)). In both panels, the lowest blue curve represents the function $\Theta(\mathrm{NA}/n_b) = c/F\Delta T$, where ΔT is the required time delay for ideal operation, given by (3.6). Fig. 3.2(b) includes both the upper bound for ideal metalenses with no aberrations, $\Delta T_{\mathrm{err}} = 0$ (Θ, lower solid blue curve), and the bound for highly aberrated metalenses with an error $\Delta T_{\mathrm{err}} = 0.8\Delta T$ ($\Theta/0.2$, dashed blue curve) and $\Delta T_{\mathrm{err}} = 0.9\Delta T$ ($\Theta/0.1$, upper solid blue curve), which correspond to low values of Strehl ratio according to (3.17). All design parameters and bandwidth values are given in Table 3.1.

with respect to an ideal spherical wavefront:

$$S \approx \mathrm{e}^{-(k_0\sigma)^2}, \tag{3.16}$$

where σ is the standard deviation of the spatial wavefront deformation and k_0 is the free-space wavenumber [132, 164, 165]. In addition, the maximum peak-to-peak deformation of the wavefront can be related to the standard deviation as $\Delta W_{\text{max}} \approx \alpha\sigma$, where the factor α depends on the type of aberration, and for a mixture of low-order aberrations (defocusing, etc.) α is in the order of a few units (e.g., $\alpha \approx 4.5$ [164]). This spatial error corresponds to a maximum phase error $\Delta\varphi_{\text{max}} = \Delta W_{\text{max}} k_0$. Thus, if a less-than-unity Strehl ratio is tolerated within the operational bandwidth of the metalens, an error in the implemented phase profile would be acceptable, which in turn would relax the requirements on the time delay ΔT and the associated bandwidth bounds. In particular, assuming no phase errors at the central frequency, if the implemented time delay is incorrect by a maximum amount ΔT_{err}, (3.2) indicates that the phase profile would be incorrect by an amount $\Delta\varphi_{\text{max}} = (\omega - \omega_c)\Delta T_{\text{err}}$ at a certain frequency ω, corresponding to a Strehl ratio:

$$S \approx \exp\Big(-\big(\alpha^{-1}(\omega - \omega_c)\Delta T_{\text{err}}\big)^2\Big). \tag{3.17}$$

Based on these considerations, it is then possible to approximately account for aberrations in our bandwidth bounds by substituting ΔT with $\Delta T - \Delta T_{\text{err}}$ in (3.3) and expressing ΔT_{err} in terms of S by inverting (3.17). This leads to a looser bandwidth bound if the Strehl ratio decreases, suggesting that a relaxation of the imaging performance of the metalens allows for a broader bandwidth, as expected. We also stress that an imaging system is considered practically diffraction limited if $S > 0.8$ [132, 164–166], which implies that the bandwidth bound may be relaxed, to some degree, with respect to the ideal case, with only minimal deterioration of the imaging performance.

Since we do not have access to the field profiles of all the metalenses considered in the literature, in Fig. 3.2(b) we include both the bound for ideal metalenses with no aberrations (lower

solid blue curve), and a bound for highly aberrated metalenses with an error $\Delta T_{\text{err}} = 0.9\Delta T$ (upper solid blue curve), corresponding to low values of Strehl ratio according to (3.17). Most published metalens designs are below the bound for ideal metalenses, with only a handful of designs exceeding this limit. However, the latter are all bound by the limit for aberrated metalenses with $\Delta T_{\text{err}} = 0.8\Delta T$ (dashed blue curve), corresponding to a typical Strehl ratio < 0.5 away from the central wavelength, which is consistent with the published results (we note that since the nominal ΔT depends on F and NA, according to (3.6), the resulting Strehl ratio also depends on these quantities). Thus, in principle, even broader bandwidths could be achievable, but only at the expenses of even higher aberrations and lower focal spot intensity.

Finally, in Fig. 3.3, we show an example of how a specific metalens design (from Ref. [135]) compares with the bandwidth limits described above, considering the case of no aberrations for simplicity. This metasurface, which is based on dielectric waveguide segments, has a much wider bandwidth than what would be achievable using a single-resonator-based design, as expected. In addition, its bandwidth performance is not too far from the appropriate upper bound (either (3.10) or (3.11)) based on the employed materials and thickness. In other words, the dielectric metalens is using its thickness and refractive-index contrast almost optimally. Fig. 3.3 also shows a design-independent version of both Tucker's and Miller's limit using the highest refractive-index and permittivity contrast naturally available at optical frequencies, for lossless dielectrics and generic materials, respectively. Further details are discussed in the Discussion and Conclusion section.

Bandwidth limits on reflection suppression — For the sake of completeness, we briefly discuss another important trade-off, between the bandwidth of operation of a metalens and its transmission efficiency. The ability to transmit energy efficiently requires, at a minimum, that the reflections are minimized, namely, that the metalens is impedance matched with respect to the medium in which

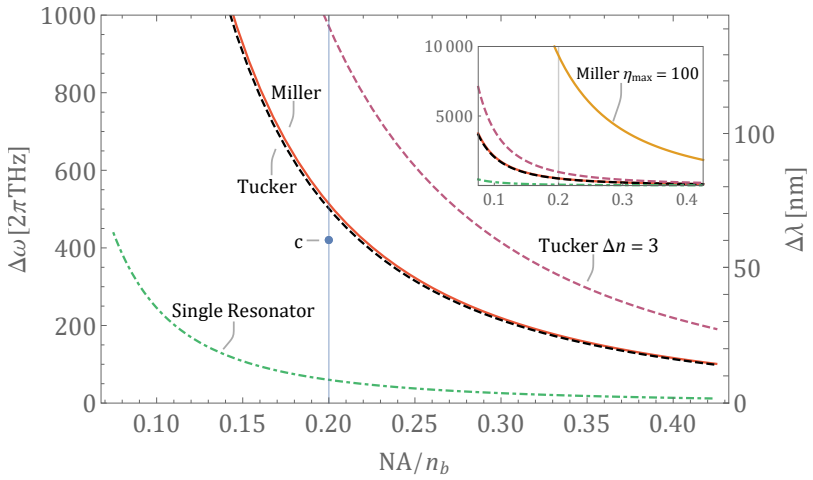

Figure 3.3: Different bandwidth limits compared to the performance of a specific metalens design, from Ref. [135] (central wavelength $\lambda_c = 518$ nm): Single-resonator limit ((3.9), dot-dashed green curve); Tucker's limit ((3.10), dashed black) and Miller's limit ((3.11), solid red) using the refractive-index/permittivity contrast considered in Ref. [135]; design-independent Tucker's limit (dashed purple) with the highest refractive index for lossless dielectrics naturally available at optical frequency, $n \approx 4$. The inset includes the same curves and an additional curve (solid orange) for a design-independent version of Miller's limit with the highest permittivity contrast (in magnitude) available at optical frequency $\eta \approx 100$ [152] (which may include the case of metallic materials, and materials with loss and gain).

the incident wave propagates (usually air or a transparent substrate). While it is always possible to design a lossless anti-reflection coating to achieve identically zero reflection (ideal impedance matching) at a single frequency, a fundamental trade-off exists between the reflection reduction and the continuous bandwidth over which this reduction can be achieved. This fundamental limit on broadband impedance matching is known as the Bode-Fano limit [167], which has been used for decades in microwave engineering, but it applies equally well at optical frequencies [168]. This bound depends uniquely on the linearity, passivity, time-invariance, and causality of the scattering system, and, most importantly, is independent of the employed anti-reflection coating, regardless of its complexity (the matching structure is only assumed to be lossless).

In order to apply the Bode-Fano limit to the problem under consideration, we approximate

the metalens as a thin homogeneous slab with refractive index equal to the average refractive index n_{avg} of the materials composing the structure. This is clearly a coarse approximation, but it allows us to get some general insight on this relevant design trade-off. In addition, we assume that we operate in the most favorable condition for impedance matching, that is, we assume that the central frequency corresponds to a Fabry-Perot resonance of the slab, at which the reflection coefficient automatically goes to zero. The slab thickness L is assumed to be smaller or comparable to the wavelength. Under these approximations, the limit is given by [168]

$$\frac{\Delta\omega}{\omega_c} \leq \frac{1}{L/\lambda_c(\varepsilon - \varepsilon_b)} \left[\log \frac{1}{|\Gamma|}\right]^{-1}, \tag{3.18}$$

where $\varepsilon = n_{\text{avg}}^2$ and Γ is the in-band reflection coefficient. If the equal sign is used, (3.18) represents the optimal trade-off between bandwidth and reflection reduction.

Depending on the application under consideration, the maximum bandwidth over which a metalens can operate depends on both the achromatic focusing limit derived above and the impedance-matching limit. Interestingly, it is immediately clear that (3.18) is inversely proportional to the thickness L and permittivity contrast η of the device, while (3.13) and (3.14) are directly proportional to these quantities. This suggests the existence of a fundamental trade-off between the ability to reduce reflections with an anti-reflection coating (maximizing transmission efficiency) and the ability to minimize chromatic aberrations for a metasurface operating over a broad continuous bandwidth. This trade-off is represented in Fig. 3.4: thicker devices or larger refractive-index contrast lead to wider bandwidths for achromatic operation (blue curves), but narrower bandwidths over which the reflection coefficient can be reduced to a certain level (orange curves). In other words, achieving achromatic performance over a wider band requires a larger $\eta L/\lambda_c$, which, however, increases the minimum reflectance achievable over that band, as expected. If both efficiency and achromatic performance are equally important, an optimal value

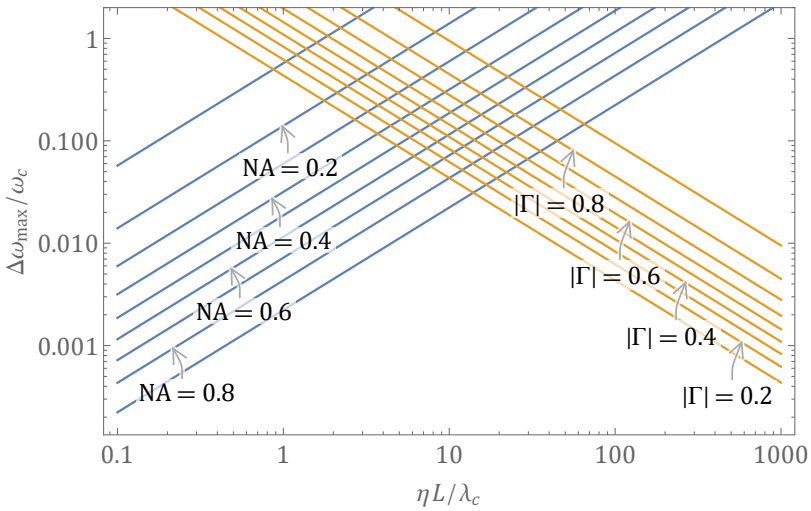

Figure 3.4: Comparison of the bandwidth limit for achromatic performance (blue), based on Miller's TBP, (3.14), and the Bode-Fano bandwidth limit on reflection reduction, (3.18) (orange), as a function of the product of permittivity contrast and normalized thickness: $\eta L/\lambda_c$. The limits are compared for various values of NA and in-band reflection coefficient $|\Gamma|$. As an example, we considered a dielectric metalens with $F = 100\lambda_c$ and $\varepsilon_b = 1$. In order to apply the Bode-Fano limit to the considered problem, and compare it with Miller's limit, we treat the metasurface as a homogeneous slab with averaged refractive index, and a permittivity contrast $\eta = \varepsilon - \varepsilon_b = \eta_{\max}$ (further details in the text). For a given value of NA and $|\Gamma|$ there is an optimal value of $\eta L/\lambda_c$, where the two limits intersect, that maximizes $\Delta\omega$.

of $\eta L/\lambda_c$ may be identified depending on the specific application under consideration.

Discussion and Conclusion

Considering the bandwidth limits on achromatic metalenses discussed above, one may wonder what type of metalens design, for a fixed refractive-index/permittivity contrast and thickness, can get closest to the limit and why.

Interestingly, for a certain refractive-index contrast, a metasurface design based on suitable dielectric waveguide segments seems to directly provide a way to realize performance close to the upper bound for the given thickness. Indeed, the guided-mode dispersion of a dielectric waveg-

uide converges to the light line of the low-index material at low frequency, and to the light line of the high-index material at high frequency. This provides an intermediate frequency window with low group velocity and locally linear dispersion that is automatically close to the optimal linear dispersion considered by Tucker et al. [153] for an ideal delay line for that level of contrast.

It is therefore not surprising that, even when considering free-form all-area optimization of dielectric metalenses as in [139], the optimization tends to create a spatial distribution of material with "channels" that resemble waveguide segments. It is also not surprising that many of the designs we considered are relatively close to the limit, as shown in Fig. 3.2(b), since many make use of the available length and refractive-index contrast almost optimally. Using the largest naturally available refractive index for a transparent material at optical frequency, which is around three to four in silicon and germanium, would certainly provide a wider bandwidth, but not an order-of-magnitude improvement with respect to metasurfaces fabricated with lower values of refractive index. Fig. 3.3 (purple dashed curve) shows the bandwidth limit for this maximum value of lossless refractive index, $n = 4$, compared to the bandwidth of the metalens in Ref. [135]. Such a bandwidth limit provides a design-independent upper bound for transparent dielectric metasurfaces, which only depends on the thickness and the desired focal length and NA. We also note that certain recently studied materials, such as phase-change chalcogenides [169], have been shown to exhibit very large refractive index over broad bandwidths, which could be promising in the context of achromatic metasurfaces; however, their non-negligible absorption losses will unavoidably deteriorate the performance of the device. Since it is unlikely that a much larger natural refractive-index contrast could be achieved in *lossless* materials at optical frequencies, the only way to improve the bandwidth performance using transparent materials is to consider longer devices, or overcome the limit by breaking its main assumptions, for example, time-invariance, a possibility that will be the subject of future works.

Considering much longer metalenses may also break the assumption of one-dimensionality on which the limits above are based (see Fig. 3.1 and related discussion). An example of this is the broadband metalens in Ref. [148], designed through free-form all-area optimization, whose thickness is more than five free-space wavelengths (and even longer considering the wavelength within the metasurface structure). Thus, this metalens cannot be considered an array of one-dimensional delay lines as in Fig. 3.1 since lateral propagation can no longer be neglected. Indeed, this thick metasurface manages to surpass our bounds to some degree, with relatively small aberrations. In general, we expect that thicker metasurfaces or stack of metasurfaces, with a thickness of several wavelengths, may be designed to optimally take advantage of the two- or three-dimensionality of the system, increasing the path a wavepacket travels laterally, not just longitudinally, which would in turn lead to wider achievable bandwidths. In this context, we believe that all-area optimization is critical to fully take advantage of the whole available *volume*.

In addition, one may also wonder whether it would be possible to artificially increase the maximum available refractive index by realizing an engineered metamaterial with effective index much larger than the one of the constituent materials. However, if the thickness of the metalens is limited to approximately a wavelength or few wavelengths, the meta-atoms must be very small to actually form an effective homogeneous metamaterial, and not act as a discrete arrangement of elements. If we choose, for example, the size of the meta-atoms to be $d \approx \lambda/10$, a dielectric meta-atom would be largely off-resonance even considering the largest refractive index, $n \approx 4$ (the first resonance of a high-index dielectric sphere is of magnetic dipolar type, and it occurs when $d \approx \lambda/n$). As a result, the effective permittivity would not be too different from the average between the permittivity of the inclusions and of the background, following standard mixing formulas for non-resonant meta-atoms (e.g., see [170]). Using plasmonic materials would allow realizing deeply subwavelength resonant meta-atoms and, therefore, a metamaterial with much larger ef-

fective permittivity. This would, however, be accompanied by large Lorentzian dispersion around an unavoidable absorption peak, which would greatly reduce the bandwidth and efficiency of the device. Still, Miller's limit in (3.14), which is based on the *magnitude* of the permittivity contrast, does not preclude the possibility of achieving better bandwidth performance at optical frequencies by using metallic materials, for which the contrast can be as high as $\eta_{\max} \approx 100$ at near-infrared frequencies. In theory, this would allow an order-of-magnitude improvement in bandwidth, as seen in the inset of Fig. 3.3 (orange curve), where we show Miller's limit for $\eta_{\max} \approx 100$. This provides a ultimate upper bound on the bandwidth of optical metalenses that may include any available material. However, there is no guarantee that this limit is tight, namely, that it could be achieved with a physical design [152].

Finally, we expect that the use of post-processing and, more generally, computational imaging techniques could enable broadband imaging even if the metalens itself does not perform achromatic focusing. This is demonstrated, for example, in [171, 172], using extended depth of focus metalenses and computational reconstruction. In this context, our bounds would be crucial to assess whether a dispersion engineered metasurface is sufficient to achieve the desired bandwidth for the considered application, or whether post-processing would be beneficial or necessary.

To conclude, we believe that the fundamental bandwidth limits presented in this Article will prove useful to the many research groups working on metasurfaces to assess and compare the performance of different devices, and may offer fundamental insight into how to design broadband achromatic metalenses for different applications.

Design	NA	F / μm	λ_{min} / nm	λ_{max} / nm	L / nm	$\lvert\varepsilon_r\rvert_{\text{max}}$	$\Delta\omega$ / 2π THz	SR / 2π THz	Miller / 2π THz	Tucker / 2π THz
a_1 [133]	0.20	63	470	670	600	6.5	1200	462	2500 (12 500)	2440 (12 200)
a_2 [133]	0.02	11 000	470	670	600	6.5	1200	272	1480 (7380)	1440 (7200)
b [134]	0.20	67	460	700	600	6.5	1400	434	2340 (11 700)	2280 (11 400)
c [135]	0.20	485	490	550	890	6.5	419	60.0	514 (2570)	501 (2510)
d_1 [136]	0.24	200	1300	1650	800	13.5	307	99.6	621 (3100)	460 (2300)
d_2 [136]	0.13	800	1200	1650	1400	13.5	428	87.6	1000 (5690)	741 (4210)
d_3 [136]	0.13	800	1200	1650	1400	13.5	428	87.6	1000 (5000)	741 (3710)
d_4 [136]	0.86	30	1200	1400	1400	13.5	224	20.8	256 (1280)	190 (948)
e [137]	0.20	17.5	435	685	400	2.4	1580	1660	1590 (7930)	2160 (10 800)
f [138]	0.216	49	420	640	800	6.5	1860	506	4050 (20 300)	3960 (19 800)
g_1 [139]	0.1	62	450	700	250	8	1490	1920	5560 (27 800)	5030 (25 200)
g_2 [139]	0.9	3	450	700	250	8	1490	154	447 (2240)	405 (2020)
g_3 [139]	0.99	0.9	450	700	500	8	1490	109	634 (3170)	574 (2870)
h_1 [140]	0.05	1000	450	750	2400	2.9	1670	479	3520 (17 600)	4510 (22 600)
h_2 [140]	0.18	1000	450	750	2600	2.9	1670	36.1	288 (1440)	369 (1840)
h_3 [140]	0.9	3.5	450	750	1250	2.9	1670	132	507 (2530)	650 (3250)
i_1 [141]	0.2	63	470	670	2000	2.9	1200	462	2880 (14 400)	3690 (18 400)
i_2 [141]	0.36	155	3000	5000	10 000	2.7	251	53.8	221 (1110)	290 (1450)
i_3 [141]	0.81	2	560	800	1600	2.9	1010	425	1780 (8890)	2280 (11 400)
j [142]	0.35	158	3000	4000	2000	15	157	56.2	416 (2080)	296 (1480)
k_1 [143]	0.106	235	400	660	800	6.5	1860	450	3610 (18 000)	3520 (17 600)
k_2 [143]	0.125	165	400	660	800	6.5	1860	460	3680 (18 400)	3590 (18 000)
k_3 [143]	0.15	118	400	660	800	6.5	1860	444	3560 (17 800)	3470 (17 400)
l_1 [144]	0.278	34.5	1000	1800	5900	2.4	837	424	2380 (11 900)	3260 (16 300)
l_2 [144]	0.11	181	1000	1800	5900	2.4	837	543	3060 (15 300)	4180 (20 900)
l_3 [144]	0.06	665	1000	1800	5900	2.4	837	499	2810 (14 100)	3840 (19 200)
m [145]	0.3	60	1000	1200	1000	13.5	314	207	2150 (10 800)	1590 (7970)
n [146]	0.385	12 000	0.375 mm	1 mm	550 μm	12	3.14	0.598	5.96 (29.8)	4.64 (23.2)

Table 3.1: Summary of design parameters and performance values of broadband achromatic metalenses in the literature. Listed are the numerical aperture (NA), the focal length (F), the wavelength range ($\lambda_{\text{min}}, \lambda_{\text{max}}$), the device thickness (L), the maximum relative permittivity used in the device ($\lvert\varepsilon_r\rvert_{\text{max}}$), the nominal bandwidth ($\Delta\omega$), and the three limits derived from the single-resonance, Miller's, and Tucker's time-bandwidth products, given by (3.12), (3.14) and (3.13), respectively. In parentheses in the last two columns are the relaxed bandwidth limits accounting for an error in the implemented time delay, $\Delta T_{\text{err}} = 0.8\Delta T$, which corresponds to large aberrations and lower focal spot intensity, as discussed in the text. All design parameters are quoted from the respective sources with the exception of some values of permittivity, which are estimated based on the material if not reported [173–176].

Outlook

This section represents a loose assortment of ideas, thoughts and unanswered questions. They are based on the work presented in the previous Chapters, and which we have either considered as future research directions, or which could merit being revisited.

The use of frequency-domain engineering remains a promising avenue for quantum optics and quantum information experiments. However, the level of control and fidelity demonstrated in our initial experimental demonstrations (Chapter 1) are not yet comparable to the state of the art in the more conventional temporal and spatial encodings of squeezed light. Arguably, the greatest shortcoming of our experimental work was in the ability to perform and verify the transformations between the light modes: nonlinear optical processes are more challenging to control than linear ones. This implies a need for better pump and seed sources, pulse shaping, and material and waveguiding platforms, e.g. for dispersion engineering. Concerning the latter, the development of platforms for integrated nonlinear optics is an active field, which will accelerate progress in quantum optics.

Integrated nonlinear and quantum optics

The most notable integrated material platform for nonlinear optics is currently thin-film lithium niobate (TFLN). The high confinement afforded by TFLN devices, and hence their high effective nonlinearities, make them attractive for complex nonlinear optical processes. Developing such integrated nonlinear and quantum photonic devices has been an aspiration, and ostensibly the field is also somewhat moving in this direction. Making use of these integrated devices is a natural extension for the kind of schemes presented in this thesis, since squeezing and frequency

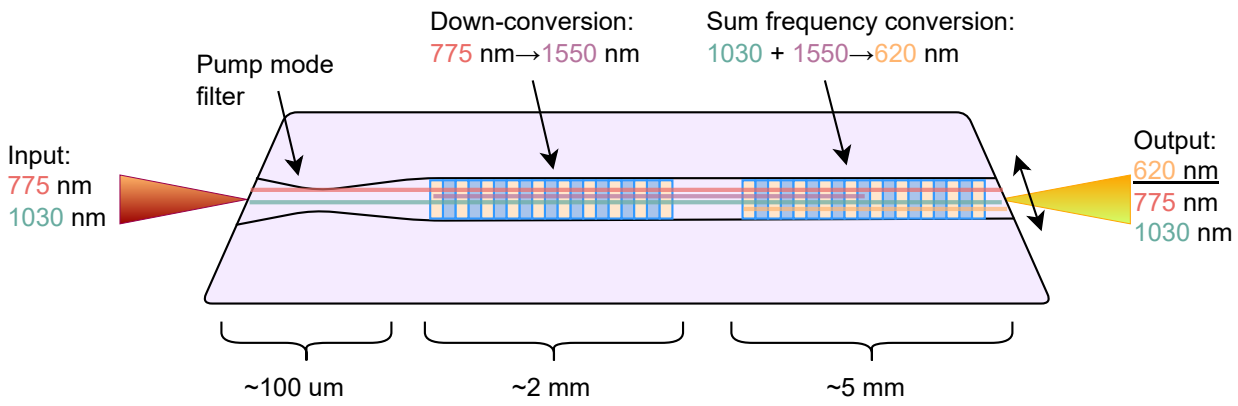

Figure 2: **OPA and AFC integrated into a single waveguide.** We can design a nonlinear waveguide incorporating both the OPA and AFC processes in a single pass of one device. The design shown uses the same architecture and wavelengths as shown in Chapter 1. However, the OPA and AFC regions can be made into two contiguous poling regions, and driven by the 775 nm and 1030 nm pumps simultaneously. This would usually be preferred to using adiabatic waveguide couplers, as these devices are typically not sufficiently broadband. Although integrated photonic devices (namely in TFLN) are currently practically limited to roughly <10 mm length, this length reduction can be compensated for by the increased effective nonlinearity due to high confinement, and the ability to engineer the dispersion. These are necessary since shorter lengths will broaden the OPA gain bandwidth and reduce the AFC efficiency. The former is approximately inversely proportional to the square root of the group velocity dispersion and the length [70], and the latter follows the Landau–Zener formula [67]. Due to the diversity in wavelengths involved in both the OPA and the AFC, a mode filter might be a necessary precaution to retain only the fundamental spatial modes of the pumps. Shorter wavelengths, including those of the pumps, might be guided in several spatial modes, but as long as the waveguide is single mode at 1550 nm and the pumps propagate in their fundamental mode, we do not expect spatio-temporal coupling at 620 nm.

conversion can, in principle, be performed compactly in a single waveguide. They are especially beneficial since broadband frequency conversion requires greater nonlinearities than conventional narrowband techniques. Indeed pump power (as well as the bandwidth) was a limitation in the experiment presented in Chapter 1. In addition, the higher nonlinearities can enable simultaneous wave-mixing processes, as required by the hybrid squeezing techniques discussed in Chapter 2. Lastly, these waveguides can be fabricated at a scale where the geometric dispersion becomes significant. Dispersion is crucial to how waves at different frequencies interact. Dispersion engineering would allow us to optimize various aspects of the squeezing and frequency conversion

processes, most notably the parametric gain bandwidth. Fig. 2 shows how a device incorporating both OPA and AFC could be realized.

Characterizing frequency domain transformations

Applying a desired frequency-domain transformation and verifying it also proved to be a challenge for other, platform-agnostic reasons, and new experimental methods should be considered to address these shortcomings. Linear transformations in the frequency domain are difficult to determine, as they require a complex-valued Green's function – input-output – measurement.

The naif approach would be to weakly seed the combined parametric amplification and conversion process over the set of wavelengths of interest, and measure the output spectral amplitudes for each input. However, obtaining the complete phase information of the transformation implies that the phase of the signal at the output wavelengths needs to be measured with respect to the phase of the input seed. This is especially impractical when the input and output are at different wavelengths. An alternative would be to use a pair of broadband, tunable, and mutually coherent sources for seeding, whose relative phase can be varied, in which case an intensity measurement of the output is sufficient. However, this solution is also nontrivial given the requirements on the seed sources.

In addition to verifying the transformation, understanding how to shape the frequency conversion pump – to yield a desired transformation in the first place – is nontrivial. The same thing can be said about squeezing: we still lack a way to program what modes are prepared by a broadband parametric amplifier and how squeezed they are.

One way forward, appears to reduce the complexity by using a "neater" discrete frequency bin

basis for squeezing and conversion (a more conventional approach). These ideas were implicitly explored in Chapter 2. One of the motivations for this research was to find ways to produce well-behaved squeezed modes and how to control them in ways that can be understood analytically. This is something that should be explored further. Nonetheless, the approach has greater experimental requirements that must be overcome, especially with respect to the necessary properties of the pumps and nonlinear devices.

Finally, one avenue that was explored but is not presented here is to use photon statistics – correlations and probabilities – to determine the underlying Gaussian state and hence the transformations. However, this proved to be impractical for many states.

Understanding frequency domain transformations

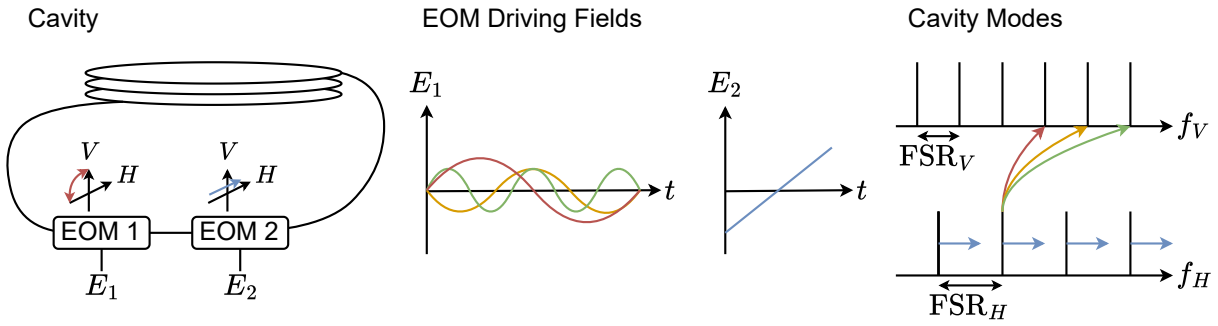

Figure 3: **Sketch of using a fiber loop to implement linear transformations in analogy to adiabatic frequency conversion.** AFC can be simulated by a birefringent fiber cavity controlled by two electro-optic modulators (EOMs). The first EOM controls the coupling between the bipartite set of polarization and frequency modes. The second adiabatically changes the path length for one polarization mode, which changes the frequency of its cavity modes. This shifting enables avoided crossings between frequency modes in opposite polarizations, if they are coupled by the first EOM. Due to the different free spectral range (FSR) of the modes in the two polarizations of the cavity, each transition between pairs of modes should be in principle individually addressable.

As mentioned in Chapter 1 Appendix D, the most general case of linear transformations with AFC – determined by a multimode system of avoided crossings – is not completely understood.

An adiabatically-varied system of discrete modes behaves as expected in the case where the avoided crossings are well-isolated, and hence the geometric phase is close to the area underneath the Δkz cell, as seen in Fig. A.10 (by "expected" we intend that the avoided crossings do not affect each other, hence, may be considered individually towards their contribution to the total linear transformation). In the continuous frequency mode case, although the physics remains the same, the validity of this interferometer network intuition becomes tenuous. This is another reason why discrete modes would be useful for quantum information applications where we need precise control of the quantum state. However, for applications where the precise control of the state is less critical, such as quantum-enhanced sensing tasks with multimode squeezed light, a black box prediction model – to invert the pump shape to the applied transformation – might be sufficient.

We can try to quantify how much control we have over the transformation in the Chapter 1 experiment by counting the degrees of freedom in the pulse shaper. Judging by the distribution of the spectrum of the pump on the SLM, shown in Fig. A.14, and the fact that the wavelength resolution was about 10 SLM pixel columns (out of 1920), implies that there were at most approximately 75 degrees of freedom. In addition, there were constraints: we wanted a phase that yields a reasonable pulse, and with sufficient chirp to overlap with the time duration of the signal. The number of degrees of freedom could be improved by increasing the pulse shaper resolution (improved choice of diffraction grating, cylindrical lens and SLM). However, it is not necessarily guaranteed that if we had more resolution it would make a proportional difference in the space of linear transformations that we could achieve.

In addition, there is the problem of individually addressing the conversion between pairs of modes. This is due to the frequency translation symmetry when the group velocity dispersion

is negligible: the frequency modes are spaced equally in momentum space, and equally coupled (via the pump frequencies) to the same modes, up to a shift. Therefore, the linear transformations in AFC are approximately convolutions. To apply more complex transformations would require applying a series of convolutions. Alternatively, sufficiently large discontinuities in the AFC process – to skip certain avoided crossings – might be a possibility, but this would only work in the discrete case. Finally, with ultrafast optics, the pump can be modulated before the process, but cannot be changed throughout, which also limits the degree of control.

One idea to study and demonstrate the full potential and physics of adiabatic frequency conversion classically is to perform the analogous process in a fiber-loop cavity with electro-optic modulators (EOMs), similar to Ref. [100]. This would allow repeated back-and-forth conversion, and the ability to change the driving fields (coupling) throughout. It seems likely that such a system could in principle perform universal linear transformations. This is illustrated in Fig. 3.

To make the system bipartite, as in AFC, one could use two the polarization modes of a cavity made of birefringent (polarization-maintaining) fiber. In addition to isolating different polarization modes, the cavity modes in such a fiber would have a different free spectral range (FSR) in each polarization. As a result, addressing individual mode transitions should be much simpler. As cavity modes are typically spaced far below optical frequencies – megahertz or gigahertz – the dispersion between them is negligible, hence there is no distinction between frequency and wavenumber as there is in ultrafast AFC: they are essentially the same variable.

The adiabatic variation can be performed by one EOM, to change the cavity length(s). This would be realized by a linearly varying voltage. One can assume that the free spectral ranges would remain approximately the same. However, changing the cavity length would mean that spectral modes in opposite polarizations would come in and out of coherence (at each round trip)

as their wavenumbers cross, enabling avoided crossings. A second polarization EOM could realize the coupling, transferring small amounts of energy from one polarization to the other during each round trip. It would by driven with a number of frequency tones at a given amplitude. These tones couple modes from opposite polarizations, separated by the given frequency. Any energy not transferred to a cavity mode will dissipate. Since we expect the frequency differences between the two polarizations modes to be unique (since the FSRs are real numbers with no common multiple), and the coupling can be changed throughout the evolution, we can expect to be able to address individual transitions.

Other experimental considerations

There were other minor experimental considerations that should be addressed in an ideal version of the experiment presented in Chapter 1.

As shown in Fig. 1.6, the DOPA pump is generated from the main 1030 nm laser, through an OPA process. Because it is amplified from a seed laser, this process risks being excessively noisy, meaning the DOPA pump could have slight variations in every shot. This was not the case in our experiment, as verified experimentally by measuring the pulses coupling out of the waveguide using a photodiode. However, this is an important consideration and a risk in any new and similar experiment.

Related to this was the experiment's stability. The beam path of the whole experiment, mainly due to the pulse shaper, was about 5 m to the DOPA from the 1030 nm laser, and approximately another 2 m to the camera. This made the experiment very susceptible to misalignment and vibrations, and not practical for long experiment run times. This was despite the face that a vibration

isolation table was used, as well as an enclosure to minimize thermal fluctuations and stray light.

Finally, we considered increasing the AFC pump bandwidth using self-phase modulation, to improve the quantum frequency-mode coupling, as in discussed in Chapter 1 Appendix K. However, given the power limitations, we could not afford losing any significant amount of pump power, for example by coupling into fiber (e.g. photonic crystal or highly nonlinear fibers). Similarly, in free space, self-focusing effects create significant undesired spatial-spectral coupling, unless some nontrivial and novel techniques are used to mitigate this. Therefore, the most practical solution is to reduce the power requirements by moving away from free space optics for the AFC, and moving to integrated photonics, as discussed previously.

Frequency domain in the future of quantum optics

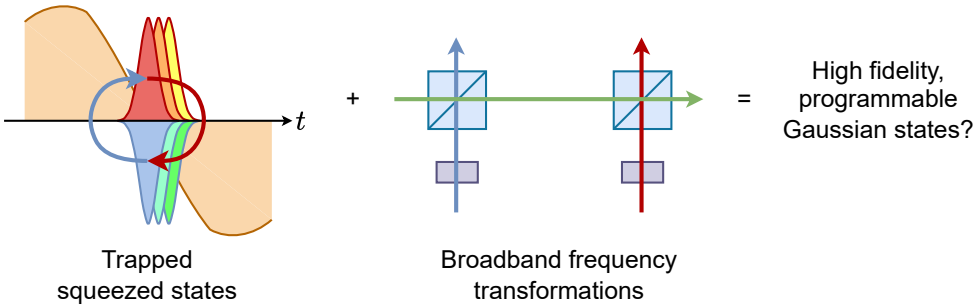

Figure 4: **Frequency domain quantum optics using spectro-temporal traps and beamsplitters.** SFG traps could be used to prepare squeezing in multiple frequency modes and without unwanted higher-order supermodes. Frequency conversion can then be used to programmably entangle the squeezed states, by appropriately tuning the classical pumps. This scheme has the potential to allow us to prepare multimode squeezed states with high fidelity and at arbitrary wavelengths, which would simplify the requirements for single-photon detection, for the choice of squeezing wavelengths, and for waveguide dispersion engineering.

Generally, there are other quantum-optical states of interest for computing and sensing, besides multimiode squeezed states. For example: cat, GKP (Gottesman–Kitaev–Preskill), and NOON

states. So far, these states have been largely out of reach of photonics other than in a few proof-of-concept demonstrations. Currently (i.e. excluding the use of few-photon nonlinearities), the most promising theoretical way to produce the first two is by partial measurement of entangled squeezed states, to (non-deterministically) project the remaining modes into the desired state [177, 178].

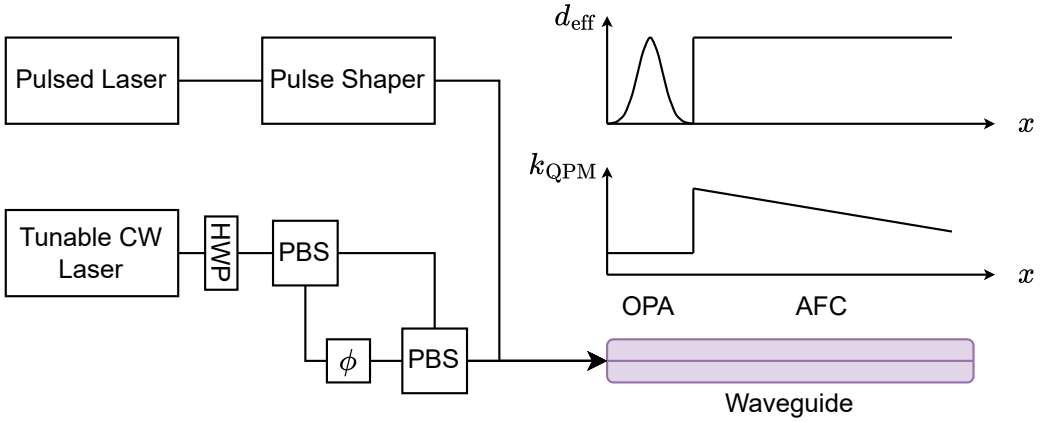

Figure 5: **Experiment demonstrating a quantum-coherent spectro-temporal beamsplitter.** This is an experimental sketch of a frequency-domain beamsplitter converting two-mode squeezed states into two single-mode squeezed states, as discussed in the first part of Chapter 2, thereby demonstrating the idea. We can design a waveguide to perform two-mode squeezing, followed by AFC, within two contiguous poling regions. The poling frequency is denoted as k_{QPM}, and effective nonlinearity (reduced frequency component in the poling grating) is denoted as d_{eff}. The most straightforward design uses Type-II two-mode squeezing: degenerate signal wavelengths, but in different polarizations. The waveguide must be dispersion engineered such that the two signal polarization modes have equal and opposite group velocity in the OPA pump frame, and minimal group velocity dispersion, as discussed in Chapter 2 Appendix E. The two-mode squeezing requires a pulsed laser, shaped to the correct bandwidth and chirp, also reviewed in Appendix E. The conversion can be performed using a single (quasi-)continuous-wave laser and using both Type-II and Type-0 sum frequency generation to convert both signal polarizations into one. These two processes require: both polarizations to be pumped; that the conversions must yield 100% and 50% respectively; and that the pumps have a phase difference of ϕ. This can be realized by adjusting the power ratio between the two polarizations (with a half-wave plate (HWP) and polarizing beam splitter (PBS)), applying a tunable phase to one pump, and recombining them. Finally, tuning the AFC pump wavelength can compensate for small fabrication imperfections resulting in time delay errors. Shifting the pump wavelength shifts the position of the two conversion points such that the two signals can be made to overlap at the second point.

However, we do not currently have a way to robustly generate single-mode squeezed states. As vacuum squeezing is increased and the photon numbers increase, the process transitions from spontaneous to stimulated emission. This changes the state evolution in ways that are difficult to predict *a priori*, and single-mode squeezed vacuum usually evolves to become multimode, introducing undesired degrees of freedom and distinguishability. This is a widely recognized problem [7]. Outside of achieving high (few-photon-induced) nonlinearites to potentially avoid using highly squeezed states as the precursor altogether, this implies the need to discover ways to produce squeezing with theoretical guarantees of single-modedness, as well as reprogrammable photonics to allow feedback throughout the squeezing process. This was one another motivation for the work presented in Chapter 2, in which we theoretically explored some promising approaches for achieving single-mode quantum optics. Furthering our understanding of how to obtain single-mode squeezing, and eventual experimental demonstrations of these techniques, is likely to be impactful. Ideally, it should be possible to trap multiple frequency modes simultaneously, interfere them using spectrotemporal beamsplitters using AFC, and perform frequency-based measurements. This is illustrated in Fig. 4.

The two concepts could initially be demonstrated separately. Demonstrating the beamsplitter would essentially involve a demonstration of the concepts presented in Chapter 2 Section 2; a tentative experimental sketch is shown in Fig. 5. Demonstrating traps, without including the OPA, might be somewhat more straightforward experimentally. It would involve measuring the spectral response of an SFG crystal pumped with the shaped pulse, and observing an immutable spectrum with respect to the input seed – that of the trapped mode. The constant shape of this spectrum would be evidence of the trapping process.

REFERENCES

[1] J. Aasi, J. Abadie, B.P. Abbott, R. Abbott, T.D. Abbott, M.R. Abernathy, C. Adams, T. Adams, P. Addesso, R.X. Adhikari, et al., Enhanced sensitivity of the ligo gravitational wave detector by using squeezed states of light. *Nature Photonics* **7**(8), 613–619 (2013)

[2] E.R. Caianiello, On quantum field theory – I: explicit solution of Dyson's equation in electrodynamics without use of Feynman graphs. *Nuovo Cim.* **10**(12), 1634–1652 (1953)

[3] L. Troyansky, N. Tishby, On the quantum evaluation of the determinant and the permanent of a matrix. *Proc. Phys. Comput* **96** (1996)

[4] S. Aaronson, A. Arkhipov, The computational complexity of linear optics. In: *Proceedings of the Forty-Third Annual ACM Symposium on Theory of Computing*. STOC '11, pp. 333–342. Association for Computing Machinery, New York, NY, USA (2011)

[5] S. Aaronson, The limits of quantum computers. *Scientific American* **298**(3) (2008)

[6] E. Knill, R. Laflamme, G.J. Milburn, A scheme for efficient quantum computation with linear optics. *Nature* **409**(6816), 46–52 (2001)

[7] M. Houde, N. Quesada, Waveguided sources of consistent, single-temporal-mode squeezed light: The good, the bad, and the ugly. *AVS Quantum Science* **5**(1), 011404 (2023)

[8] R.W. Boyd, A.L. Gaeta, E. Giese, *Nonlinear Optics*. Elsevier, London, United Kingdom (2020)

[9] P.D. Drummond, M. Hillery, *The Quantum Theory of Nonlinear Optics*. Cambridge University Press, Cambridge, United Kingdom (2014)

[10] F. Presutti, L.G. Wright, S.-Y. Ma, T. Wang, B.K. Malia, T. Onodera, P.L. McMahon, Highly multimode visible squeezed light with programmable spectral correlations through broadband up-conversion (2024) arXiv:2401.06119 [quant-ph]

[11] N.C. Menicucci, P. Loock, M. Gu, C. Weedbrook, T.C. Ralph, M.A. Nielsen, Universal quantum computation with continuous-variable cluster states. *Phys. Rev. Lett.* **97**(11), 110501 (2006)

[12] S.-H. Tan, B.I. Erkmen, V. Giovannetti, S. Guha, S. Lloyd, L. Maccone, S. Pirandola, J.H. Shapiro, Quantum illumination with Gaussian states. *Phys. Rev. Lett.* **101**(25), 253601 (2008)

[13] C. Weedbrook, S. Pirandola, R. García-Patrón, N.J. Cerf, T.C. Ralph, J.H. Shapiro, S. Lloyd, Gaussian quantum information. *Rev. Mod. Phys.* **84**(2), 621–669 (2012)

[14] J.E. Bourassa, R.N. Alexander, M. Vasmer, A. Patil, I. Tzitrin, T. Matsuura, D. Su, B.Q. Baragiola, S. Guha, G. Dauphinais, et al., Blueprint for a scalable photonic fault-tolerant quantum computer. *Quantum* **5**, 392 (2021)

[15] S. Rahimi-Keshari, A.P. Lund, T.C. Ralph, What can quantum optics say about computational complexity theory? *Phys. Rev. Lett.* **114**(6), 060501 (2015)

[16] C.S. Hamilton, R. Kruse, L. Sansoni, S. Barkhofen, C. Silberhorn, I. Jex, Gaussian boson sampling. *Phys. Rev. Lett.* **119**(17), 170501 (2017)

[17] D. Hangleiter, J. Eisert, Computational advantage of quantum random sampling. *Rev. Mod. Phys.* **95**(3), 035001 (2023)

[18] H.-S. Zhong, H. Wang, Y.-H. Deng, M.-C. Chen, L.-C. Peng, Y.-H. Luo, J. Qin, D. Wu, X. Ding, Y. Hu, et al., Quantum computational advantage using photons. *Science* **370**(6523), 1460–1463 (2020)

[19] H.-S. Zhong, Y.-H. Deng, J. Qin, H. Wang, M.-C. Chen, L.-C. Peng, Y.-H. Luo, D. Wu, S.-Q. Gong, H. Su, et al., Phase-programmable Gaussian boson sampling using stimulated squeezed light. *Phys. Rev. Lett.* **127**(18), 180502 (2021)

[20] Y.-H. Deng, Y.-C. Gu, H.-L. Liu, S.-Q. Gong, H. Su, Z.-J. Zhang, H.-Y. Tang, M.-H. Jia, J.-M. Xu, M.-C. Chen, et al., Gaussian boson sampling with pseudo-photon-number-resolving detectors and quantum computational advantage. *Phys. Rev. Lett.* **131**(15), 150601 (2023)

[21] L.S. Madsen, F. Laudenbach, M.F. Askarani, F. Rortais, T. Vincent, J.F.F. Bulmer, F.M. Miatto, L. Neuhaus, L.G. Helt, M.J. Collins, et al., Quantum computational advantage with a programmable photonic processor. *Nature* **606**(7912), 75–81 (2022)

[22] J.M. Lukens, P. Lougovski, Frequency-encoded photonic qubits for scalable quantum information processing. *Optica* **4**(1), 8–16 (2017)

[23] C. Joshi, A. Farsi, S. Clemmen, S. Ramelow, A.L. Gaeta, Frequency multiplexing for quasi-deterministic heralded single-photon sources. *Nature Communications* **9**(1) (2018)

[24] C. Joshi, A. Farsi, A. Gaeta, Frequency-domain boson sampling. In: *Conference on Lasers and Electro-Optics*. FTu1F.1. Optica Publishing Group, San Jose, CA, United States (2017)

[25] T. Hiemstra, T.F. Parker, P. Humphreys, J. Tiedau, M. Beck, M. Karpiński, B.J. Smith, A. Eckstein, W.S. Kolthammer, I.A. Walmsley, Pure single photons from scalable frequency multiplexing. *Phys. Rev. Appl.* **14**(1), 014052 (2020)

[26] C. Reimer, M. Kues, P. Roztocki, B. Wetzel, F. Grazioso, B.E. Little, S.T. Chu, T. Johnston, Y. Bromberg, L. Caspani, et al., Generation of multiphoton entangled quantum states by means of integrated frequency combs. *Science* **351**(6278), 1176–1180 (2016)

[27] M. Cabrejo-Ponce, A.L.M. Muniz, M. Huber, F. Steinlechner, High-dimensional entanglement for quantum communication in the frequency domain. *Laser & Photonics Reviews*, 2201010 (2023)

[28] J.R. Basani, M. Heuck, D.R. Englund, S. Krastanov, All-photonic artificial-neural-network processor via nonlinear optics. *Phys. Rev. Appl.* **22**(1), 014009 (2024)

[29] N. Liu, Y. Liu, J. Li, L. Yang, X. Li, Generation of multi-mode squeezed vacuum using pulse pumped fiber optical parametric amplifiers. *Optics Express* **24**(3), 2125–2133 (2016)

[30] A. Omi, A. Hosaka, M. Tomita, Y. Yamagishi, K. Wakui, S. Niimura, K. Takahashi, M. Takeoka, F. Kannari, Independently programmable frequency-multiplexed phase-sensitive optical parametric amplification in the optical telecommunication band. *Opt. Express* **29**(14), 21683–21697 (2021)

[31] Y. Yamagishi, A. Hosaka, K. Tanji, S. Kurimura, F. Kannari, Arbitrary mixing of frequency-range multimode quantum states using nonlinear waveguide crystals based on dispersion engineering. In: *OSA Nonlinear Optics 2021*. NM2B.4. Optica Publishing Group, Washington, DC, United States (2021)

[32] J. Roslund, R.M. Araújo, S. Jiang, C. Fabre, N. Treps, Wavelength-multiplexed quantum networks with ultrafast frequency combs. *Nature Photonics* **8**(2), 109–112 (2014)

[33] Y. Cai, J. Roslund, G. Ferrini, F. Arzani, X. Xu, C. Fabre, N. Treps, Multimode entanglement in reconfigurable graph states using optical frequency combs. *Nature Communications* **8**(1), 15645 (2017)

[34] V. Roman-Rodriguez, D. Fainsin, G.L. Zanin, N. Treps, E. Diamanti, V. Parigi, Multimode squeezed state for reconfigurable quantum networks at telecommunication wavelengths (2023) arXiv:2306.07267 [quant-ph]

[35] Z. Yang, M. Jahanbozorgi, D. Jeong, S. Sun, O. Pfister, H. Lee, X. Yi, A squeezed quantum microcomb on a chip. *Nature Communications* **12**(1), 4781 (2021)

[36] M. Jahanbozorgi, Z. Yang, S. Sun, H. Chen, R. Liu, B. Wang, X. Yi, Generation of squeezed quantum microcombs with silicon nitride integrated photonic circuits. *Optica* **10**(8), 1100–1101 (2023)

[37] M. Pysher, Y. Miwa, R. Shahrokhshahi, R. Bloomer, O. Pfister, Parallel generation of quadripartite cluster entanglement in the optical frequency comb. *Phys. Rev. Lett.* **107**(3), 030505 (2011)

[38] M. Chen, N.C. Menicucci, O. Pfister, Experimental realization of multipartite entanglement of 60 modes of a quantum optical frequency comb. *Phys. Rev. Lett.* **112**(12), 120505 (2014)

[39] Z. Xie, T. Zhong, S. Shrestha, X. Xu, J. Liang, Y.-X. Gong, J.C. Bienfang, A. Restelli, J.H. Shapiro, F.N.C. Wong, C.W. Wong, Harnessing high-dimensional hyperentanglement through a biphoton frequency comb. *Nature Photonics* **9**(8), 536–542 (2015)

[40] K.-C. Chang, X. Cheng, M.C. Sarihan, A.K. Vinod, Y.S. Lee, T. Zhong, Y.-X. Gong, Z. Xie, J.H. Shapiro, F.N.C. Wong, C.W. Wong, 648 Hilbert-space dimensionality in a biphoton fre-

quency comb: entanglement of formation and Schmidt mode decomposition. *npj Quantum Information* **7**(1), 48 (2021)

[41] A. Eldan, O. Gilon, A. Lagimi, E. Forman, A. Pe'er, Multiplexed processing of quantum information across an ultra-wide optical bandwidth (2023) arXiv:2310.17819 [quant-ph]

[42] H.-H. Lu, J.M. Lukens, N.A. Peters, O.D. Odele, D.E. Leaird, A.M. Weiner, P. Lougovski, Electro-optic frequency beam splitters and tritters for high-fidelity photonic quantum information processing. *Phys. Rev. Lett.* **120**(3), 030502 (2018)

[43] H.-H. Lu, E.M. Simmerman, P. Lougovski, A.M. Weiner, J.M. Lukens, Fully arbitrary control of frequency-bin qubits. *Phys. Rev. Lett.* **125**(12), 120503 (2020)

[44] U.A. Javid, R. Lopez-Rios, J. Ling, A. Graf, J. Staffa, Q. Lin, Chip-scale simulations in a quantum-correlated synthetic space. *Nature Photonics* **17**(10), 883–890 (2023)

[45] L. Yuan, A. Dutt, S. Fan, Synthetic frequency dimensions in dynamically modulated ring resonators. *APL Photonics* **6**(7), 071102 (2021)

[46] X. Zhu, C.-H. Chang, C. González-Arciniegas, A. Pe'er, J. Higgins, O. Pfister, Hypercubic cluster states in the phase-modulated quantum optical frequency comb. *Optica* **8**(3), 281–290 (2021)

[47] H.-H. Lu, M. Liscidini, A.L. Gaeta, A.M. Weiner, J.M. Lukens, Frequency-bin photonic quantum information. *Optica* **10**(12), 1655–1671 (2023)

[48] C. Joshi, A. Farsi, A. Dutt, B.Y. Kim, X. Ji, Y. Zhao, A.M. Bishop, M. Lipson, A.L. Gaeta, Frequency-domain quantum interference with correlated photons from an integrated microresonator. *Phys. Rev. Lett.* **124**(14), 143601 (2020)

[49] C.M. Natarajan, M.G. Tanner, R.H. Hadfield, Superconducting nanowire single-photon detectors: physics and applications. *Superconductor Science and Technology* **25**(6), 063001 (2012)

[50] I. Esmaeil Zadeh, J. Chang, J.W.N. Los, S. Gyger, A.W. Elshaari, S. Steinhauer, S.N. Dorenbos, V. Zwiller, Superconducting nanowire single-photon detectors: A perspective on evolution, state-of-the-art, future developments, and applications. *Applied Physics Letters* **118**(19), 190502 (2021)

[51] H. Defienne, B. Ndagano, A. Lyons, D. Faccio, Polarization entanglement-enabled quantum holography. *Nature Physics* **17**(5), 591–597 (2021)

[52] E. Bolduc, D. Faccio, J. Leach, Acquisition of multiple photon pairs with an EMCCD camera. *Journal of Optics* **19**(5), 054006 (2017)

[53] H. Defienne, J. Zhao, E. Charbon, D. Faccio, Full-field quantum imaging with a single-photon avalanche diode camera. *Phys. Rev. A* **103**(4), 042608 (2021)

[54] A. Kumar, A.M. Marino, Spatial squeezing in bright twin beams generated with four-wave mixing: Constraints on characterization with an electron-multiplying charge-coupled-device camera. *Phys. Rev. A* **100**(6), 063828 (2019)

[55] F. Li, T. Li, M.O. Scully, G.S. Agarwal, Quantum advantage with seeded squeezed light for absorption measurement. *Phys. Rev. Appl.* **15**(4), 044030 (2021)

[56] P. Svihra, Y. Zhang, P. Hockett, S. Ferrante, B. Sussman, D. England, A. Nomerotski, Multivariate discrimination in quantum target detection. *Applied Physics Letters* **117**(4), 044001 (2020)

[57] K. Dhimitri, S.M. Fullerton, B. Coyle, K.E. Bennett, T. Miura, T. Higuchi, T. Maruno, Scientific CMOS (sCMOS) camera capabilities with a focus on quantum applications. In:

D.F. Figer (ed.) *Photonics for Quantum 2022*. PC122430L, vol. PC12243. SPIE, Rochester, NY, United States (2022). International Society for Optics and Photonics

[58] J. Ma, S. Masoodian, D.A. Starkey, E.R. Fossum, Photon-number-resolving megapixel image sensor at room temperature without avalanche gain. *Optica* **4**(12), 1474–1481 (2017)

[59] P. Kumar, Quantum frequency conversion. *Opt. Lett.* **15**(24), 1476–1478 (1990)

[60] X. Wang, X. Jiao, B. Wang, Y. Liu, X.-P. Xie, M.-Y. Zheng, Q. Zhang, J.-W. Pan, Quantum frequency conversion and single-photon detection with lithium niobate nanophotonic chips. *npj Quantum Information* **9**(1) (2023)

[61] C.E. Vollmer, C. Baune, A. Samblowski, T. Eberle, V. Händchen, J. Fiurášek, R. Schnabel, Quantum up-conversion of squeezed vacuum states from 1550 to 532 nm. *Phys. Rev. Lett.* **112**(7), 073602 (2014)

[62] C. Baune, J. Gniesmer, A. Schönbeck, C.E. Vollmer, J. Fiurášek, R. Schnabel, Strongly squeezed states at 532 nm based on frequency up-conversion. *Opt. Express* **23**(12), 16035–16041 (2015)

[63] A. Samblowski, C.E. Vollmer, C. Baune, J. Fiurášek, R. Schnabel, Weak-signal conversion from 1550 to 532 nm with 84% efficiency. *Opt. Lett.* **39**(10), 2979–2981 (2014)

[64] K.A.G. Bonsma-Fisher, P.J. Bustard, C. Parry, T.A. Wright, D.G. England, B.J. Sussman, P.J. Mosley, Ultratunable quantum frequency conversion in photonic crystal fiber. *Phys. Rev. Lett.* **129**(20), 203603 (2022)

[65] M. Allgaier, V. Ansari, L. Sansoni, C. Eigner, V. Quiring, R. Ricken, G. Harder, B. Brecht, C. Silberhorn, Highly efficient frequency conversion with bandwidth compression of quantum light. *Nature Communications* **8**(1) (2017)

[66] H. Suchowski, B.D. Bruner, Y. Israel, A. Ganany-Padowicz, A. Arie, Y. Silberberg, Broadband photon pair generation at $3\omega/2$. *Applied Physics B* **122**, 1–5 (2016)

[67] H. Suchowski, V. Prabhudesai, D. Oron, A. Arie, Y. Silberberg, Robust adiabatic sum frequency conversion. *Opt. Express* **17**(15), 12731–12740 (2009)

[68] J. Moses, H. Suchowski, F.X. Kärtner, Fully efficient adiabatic frequency conversion of broadband Ti:sapphire oscillator pulses. *Opt. Lett.* **37**(9), 1589–1591 (2012)

[69] A.I. Lvovsky, Squeezed light. *Photonics: Scientific Foundations, Technology and Applications* **1**, 121–163 (2015). Chap. 5

[70] W. Wasilewski, A.I. Lvovsky, K. Banaszek, C. Radzewicz, Pulsed squeezed light: Simultaneous squeezing of multiple modes. *Phys. Rev. A* **73**(6), 063819 (2006)

[71] A. Hosaka, T. Kawamori, F. Kannari, Multimode quantum theory of nonlinear propagation in optical fibers. *Phys. Rev. A* **94**(5), 053833 (2016)

[72] V.D. Vaidya, B. Morrison, L.G. Helt, R. Shahrokshahi, D.H. Mahler, M.J. Collins, K. Tan, J. Lavoie, A. Repingon, M. Menotti, et al., Broadband quadrature-squeezed vacuum and nonclassical photon number correlations from a nanophotonic device. *Science Advances* **6**(39), 9186 (2020)

[73] Nuvu Cameras, HNü 512 – 512 x 512 EMCCD. `https://www.nuvucameras.com/products/hnu-512/`. Accessed: 2024-01-07.

[74] E. Lantz, J.-L. Blanchet, L. Furfaro, F. Devaux, Multi-imaging and Bayesian estimation for photon counting with EMCCDs. *Monthly Notices of the Royal Astronomical Society* **386**(4), 2262–2270 (2008)

[75] M.J. Fitch, B.C. Jacobs, T.B. Pittman, J.D. Franson, Photon-number resolution using time-multiplexed single-photon detectors. *Phys. Rev. A* **68**(4), 043814 (2003)

[76] H. Paul, P. Törmä, T. Kiss, I. Jex, Photon chopping: New way to measure the quantum state of light. *Phys. Rev. Lett.* **76**(14), 2464–2467 (1996)

[77] J. Sperling, W. Vogel, G.S. Agarwal, True photocounting statistics of multiple on-off detectors. *Phys. Rev. A* **85**(2), 023820 (2012)

[78] R. Nehra, R. Sekine, L. Ledezma, Q. Guo, R.M. Gray, A. Roy, A. Marandi, Few-cycle vacuum squeezing in nanophotonics. *Science* **377**(6612), 1333–1337 (2022)

[79] L. Ledezma, R. Sekine, Q. Guo, R. Nehra, S. Jahani, A. Marandi, Intense optical parametric amplification in dispersion-engineered nanophotonic lithium niobate waveguides. *Optica* **9**(3), 303–308 (2022)

[80] I. Hurvitz, A. Karnieli, A. Arie, Frequency-domain engineering of bright squeezed vacuum for continuous-variable quantum information. *Optics Express* **31**(12), 20387 (2023)

[81] C. Drago, A.M. Brańczyk, Tunable frequency-bin multimode squeezed vacuum states of light. *Phys. Rev. A* **106**(4), 043714 (2022)

[82] C.L. Morrison, F. Graffitti, P. Barrow, A. Pickston, J. Ho, A. Fedrizzi, Frequency-bin entanglement from domain-engineered down-conversion. *APL Photonics* **7**(6), 066102 (2022)

[83] P. Folge, M. Santandrea, M. Stefszky, B. Brecht, C. Silberhorn, Multimode squeezed states in frequency conversion based time-frequency networks. In: *Frontiers in Optics + Laser Science 2022 (FIO, LS)*. FM5B.5. Optica Publishing Group, Rochester, NY, United States (2022)

[84] E. Rozenberg, A. Karnieli, O. Yesharim, J. Foley-Comer, S. Trajtenberg-Mills, D. Freedman, A.M. Bronstein, A. Arie, Inverse design of spontaneous parametric downconversion for generation of high-dimensional qudits. *Optica* **9**(6), 602–615 (2022)

[85] E. Frumker, Y. Silberberg, Phase and amplitude pulse shaping with two-dimensional phase-only spatial light modulators. *J. Opt. Soc. Am. B* **24**(12), 2940–2947 (2007)

[86] S. Olivares, Quantum optics in the phase space: a tutorial on gaussian states. *The European Physical Journal Special Topics* **203**(1), 3–24 (2012)

[87] A. Ferraro, S. Olivares, M.G.A. Paris, Gaussian states in continuous variable quantum information (2005) arXiv:quant-ph/0503237 [quant-ph]

[88] T. Opatrný, N. Korolkova, G. Leuchs, Mode structure and photon number correlations in squeezed quantum pulses. *Phys. Rev. A* **66**(5), 053813 (2002)

[89] G. Adesso, S. Ragy, A.R. Lee, Continuous variable quantum information: Gaussian states and beyond. *Open Systems & Information Dynamics* **21**(01n02), 1440001 (2014)

[90] K.E. Cahill, R.J. Glauber, Ordered expansions in boson amplitude operators. *Phys. Rev.* **177**(5), 1857–1881 (1969)

[91] J. Katriel, Combinatorial aspects of boson algebra. *Lett. Nuovo Cimento* **10**(13), 565–567 (1974)

[92] H.-Y. Fan, Operator ordering in quantum optics theory and the development of Dirac's symbolic method. *Journal of Optics B: Quantum and Semiclassical Optics* **5**(4), 147–163 (2003)

[93] S. Brundobler, V. Elser, S-matrix for generalized Landau–Zener problem. *Journal of Physics A: Mathematical and General* **26**(5), 1211 (1993)

[94] Y.N. Demkov, V.N. Ostrovsky, Crossing of two bands of potential curves. *Journal of Physics B: Atomic, Molecular and Optical Physics* **28**(3), 403 (1995)

[95] T. Usuki, Theoretical study of Landau–Zener tunneling at the $M + N$ level crossing. *Phys. Rev. B* **56**(20), 13360–13366 (1997)

[96] A.V. Shytov, Landau–Zener transitions in a multilevel system: An exact result. *Phys. Rev. A* **70**(5), 052708 (2004)

[97] R.K. Malla, V.Y. Chernyak, N.A. Sinitsyn, Nonadiabatic transitions in Landau–Zener grids: Integrability and semiclassical theory. *Phys. Rev. B* **103**(14), 144301 (2021)

[98] S.N. Shevchenko, S. Ashhab, F. Nori, Landau–Zener–Stückelberg interferometry. *Physics Reports* **492**(1), 1–30 (2010)

[99] D.A. Harmin, Coherent time evolution on a grid of Landau–Zener anticrossings. *Phys. Rev. A* **56**(1), 232–251 (1997)

[100] D. Bouwmeester, I. Marzoli, G.P. Karman, W. Schleich, J.P. Woerdman, Optical Galton board. *Phys. Rev. A* **61**(1), 013410 (1999)

[101] K. Fradkin, A. Arie, A. Skliar, G. Rosenman, Tunable midinfrared source by difference frequency generation in bulk periodically poled KTiOPO4. *Applied Physics Letters* **74**(7), 914–916 (1999)

[102] S. Emanueli, A. Arie, Temperature-dependent dispersion equations for KTiOPO4 and KTiOAsO4. *Appl. Opt.* **42**(33), 6661–6665 (2003)

[103] S. Hegde, K. Schepler, R. Peterson, D. Zelmon, Room-temperature, near IR fluorescence of high optical quality KTP. In: G.L. Wood, M.A. Dubinskii (eds.) *Laser Source Technology*

for Defense and Security III, vol. 6552, pp. 177–184. SPIE, Orlando, FL, United States (2007). International Society for Optics and Photonics

[104] L. Xu, D. Chang, H. Niu, S. Jia, Observation of Raman scattering and fluorescent spectra of $KTiOPO_4$(KTP) crystal. *Chinese Physics Letters* **6**(5), 65520 (1989)

[105] M. Tillmann, B. Dakić, R. Heilmann, S. Nolte, A. Szameit, P. Walther, Experimental boson sampling. *Nature Photonics* **7**(7), 540–544 (2013)

[106] A. Crespi, R. Osellame, R. Ramponi, D.J. Brod, E.F. Galvão, N. Spagnolo, C. Vitelli, E. Maiorino, P. Mataloni, F. Sciarrino, Integrated multimode interferometers with arbitrary designs for photonic boson sampling. *Nature Photonics* **7**(7), 545–549 (2013)

[107] M.A. Broome, A. Fedrizzi, S. Rahimi-Keshari, J. Dove, S. Aaronson, T.C. Ralph, A.G. White, Photonic boson sampling in a tunable circuit. *Science* **339**(6121), 794–798 (2013)

[108] S. Yokoyama, R. Ukai, S.C. Armstrong, C. Sornphiphatphong, T. Kaji, S. Suzuki, J. Yoshikawa, H. Yonezawa, N.C. Menicucci, A. Furusawa, Ultra-large-scale continuous-variable cluster states multiplexed in the time domain. *Nature Photonics* **7**(12), 982–986 (2013)

[109] J. Carolan, J.D.A. Meinecke, P.J. Shadbolt, N.J. Russell, N. Ismail, K. Wörhoff, T. Rudolph, M.G. Thompson, J.L. O'Brien, J.C.F. Matthews, A. Laing, On the experimental verification of quantum complexity in linear optics. *Nature Photonics* **8**(8), 621–626 (2014)

[110] M. Bentivegna, N. Spagnolo, C. Vitelli, F. Flamini, N. Viggianiello, L. Latmiral, P. Mataloni, D.J. Brod, E.F. Galvão, A. Crespi, et al., Experimental scattershot boson sampling. *Science Advances* **1**(3), 1400255 (2015)

[111] J. Carolan, C. Harrold, C. Sparrow, E. Martín-López, N.J. Russell, J.W. Silverstone, P.J. Shadbolt, N. Matsuda, M. Oguma, M. Itoh, et al., Universal linear optics. *Science* **349**(6249), 711–716 (2015)

[112] G. Harder, T.J. Bartley, A.E. Lita, S.W. Nam, T. Gerrits, C. Silberhorn, Single-mode parametric-down-conversion states with 50 photons as a source for mesoscopic quantum optics. *Phys. Rev. Lett.* **116**(14), 143601 (2016)

[113] J. Yoshikawa, S. Yokoyama, T. Kaji, C. Sornphiphatphong, Y. Shiozawa, K. Makino, A. Furusawa, Invited Article: Generation of one-million-mode continuous-variable cluster state by unlimited time-domain multiplexing. *APL Photonics* **1**(6), 060801 (2016)

[114] H.-S. Zhong, Y. Li, W. Li, L.-C. Peng, Z.-E. Su, Y. Hu, Y.-M. He, X. Ding, W. Zhang, H. Li, et al., 12-photon entanglement and scalable scattershot boson sampling with optimal entangled-photon pairs from parametric down-conversion. *Phys. Rev. Lett.* **121**(25), 250505 (2018)

[115] H.-S. Zhong, L.-C. Peng, Y. Li, Y. Hu, W. Li, J. Qin, D. Wu, W. Zhang, H. Li, L. Zhang, et al., Experimental Gaussian boson sampling. *Science Bulletin* **64**(8), 511–515 (2019)

[116] S. Paesani, Y. Ding, R. Santagati, L. Chakhmakhchyan, C. Vigliar, K. Rottwitt, L.K. Oxenløwe, J. Wang, M.G. Thompson, A. Laing, Generation and sampling of quantum states of light in a silicon chip. *Nature Physics* **15**(9), 925–929 (2019)

[117] S. Takeda, K. Takase, A. Furusawa, On-demand photonic entanglement synthesizer. *Science Advances* **5**(5), 4530 (2019)

[118] W. Asavanant, Y. Shiozawa, S. Yokoyama, B. Charoensombutamon, H. Emura, R.N. Alexander, S. Takeda, J. Yoshikawa, N.C. Menicucci, H. Yonezawa, A. Furusawa, Generation of time-domain-multiplexed two-dimensional cluster state. *Science* **366**(6463), 373–376 (2019)

[119] M.V. Larsen, X. Guo, C.R. Breum, J.S. Neergaard-Nielsen, U.L. Andersen, Deterministic generation of a two-dimensional cluster state. *Science* **366**(6463), 369–372 (2019)

[120] J.M. Arrazola, V. Bergholm, K. Brádler, T.R. Bromley, M.J. Collins, I. Dhand, A. Fumagalli, T. Gerrits, A. Goussev, L.G. Helt, et al., Quantum circuits with many photons on a programmable nanophotonic chip. *Nature* **591**(7848), 54–60 (2021)

[121] S. Sempere-Llagostera, R.B. Patel, I.A. Walmsley, W.S. Kolthammer, Experimentally finding dense subgraphs using a time-bin encoded gaussian boson sampling device. *Phys. Rev. X* **12**(3), 031045 (2022)

[122] S. Yu, Z.-P. Zhong, Y. Fang, R.B. Patel, Q.-P. Li, W. Liu, Z. Li, L. Xu, S. Sagona-Stophel, E. Mer, et al., A universal programmable Gaussian boson sampler for drug discovery. *Nature Computational Science* (2023)

[123] J. Bao, Z. Fu, T. Pramanik, J. Mao, Y. Chi, Y. Cao, C. Zhai, Y. Mao, T. Dai, X. Chen, et al., Very-large-scale integrated quantum graph photonics. *Nature Photonics* **17**(7), 573–581 (2023)

[124] H. Qi, D.J. Brod, N. Quesada, R. García-Patrón, Regimes of classical simulability for noisy Gaussian boson sampling. *Phys. Rev. Lett.* **124**(10), 100502 (2020)

[125] A.B. U'Ren, C. Silberhorn, R. Erdmann, K. Banaszek, W.P. Grice, I.A. Walmsley, M.G. Raymer, Generation of pure-state single-photon wavepackets by conditional preparation based on spontaneous parametric downconversion (2006) arXiv:quant-ph/0611019 [quant-ph]

[126] F. Presutti, F. Monticone, Focusing on bandwidth: achromatic metalens limits. *Optica* **7**(6), 624–631 (2020)

[127] M. Khorasaninejad, F. Capasso, Metalenses: Versatile multifunctional photonic components. *Science* **358**(6367) (2017)

[128] M.L. Tseng, H.-H. Hsiao, C.H. Chu, M.K. Chen, G. Sun, A.-Q. Liu, D.P. Tsai, Metalenses: Advances and applications. *Advanced Optical Materials* **6**(18), 1800554 (2018)

[129] P. Lalanne, P. Chavel, Metalenses at visible wavelengths: past, present, perspectives. *Laser & Photonics Reviews* **11**(3), 1600295 (2017)

[130] A. Silva, F. Monticone, G. Castaldi, V. Galdi, A. Alù, N. Engheta, Performing mathematical operations with metamaterials. *Science* **343**(6167), 160–163 (2014)

[131] A. Pors, M.G. Nielsen, S.I. Bozhevolnyi, Analog computing using reflective plasmonic metasurfaces. *Nano Letters* **15**(1), 791–797 (2015)

[132] M. Born, E. Wolf, *Principles of Optics*, 6th edn. Pergamon, Oxford, United Kingdom (1980)

[133] W.T. Chen, A.Y. Zhu, V. Sanjeev, M. Khorasaninejad, Z. Shi, E. Lee, F. Capasso, A broadband achromatic metalens for focusing and imaging in the visible. *Nature Nanotechnology* **13**, 220–226 (2018)

[134] W.T. Chen, A. Y. Zhu, J. Sisler, Z. Bharwani, F. Capasso, A broadband achromatic polarization-insensitive metalens consisting of anisotropic nanostructures. *Nature Communications* **10**, 355 (2019)

[135] M. Khorasaninejad, Z. Shi, A.Y. Zhu, W.T. Chen, V. Sanjeev, A. Zaidi, F. Capasso, Achromatic metalens over 60 nm bandwidth in the visible and metalens with reverse chromatic dispersion. *Nano Letters* **17**(3), 1819–1824 (2017)

[136] S. Shrestha, A. C. Overvig, M. Lu, A. Stein, N. Yu, Broadband achromatic dielectric metalenses. *Light: Science & Applications* **7**, 85 (2018)

[137] M. Ye, V. Ray, Y.S. Yi, Achromatic flat subwavelength grating lens over whole visible bandwidths. *IEEE Photonics Technology Letters* **30**(10), 955–958 (2018)

[138] R.J. Lin, V.-C. Su, S. Wang, M.K. Chen, T.L. Chung, Y.H. Chen, H.Y. Kuo, J.-W. Chen, J. Chen, Y.-T. Huang, et al., Achromatic metalens array for full-colour light-field imaging. *Nature Nanotechnology* **14**(3), 227–231 (2019)

[139] H. Chung, O.D. Miller, High-NA achromatic metalenses by inverse design. *Optics Express* **28**(5), 6945 (2020)

[140] N. Mohammad, M. Meem, P. Wang, R. Menon, Broadband imaging with one planar diffractive lens. *Scientific Reports* **8**, 2799 (2018)

[141] S. Banerji, M. Meem, A. Majumder, F.G. Vasquez, B. Sensale-Rodriguez, R. Menon, Imaging with flat optics: metalenses or diffractive lenses? *Optica* **6**(6), 805–810 (2019)

[142] S. Zhang, A. Soibel, S. Keo, D. Wilson, S. Rafol, D. Z. Ting, A. She, S. D. Gunapala, F. Capasso, Solid-immersion metalenses for infrared focal plane arrays. *Applied Physics Letters* **113**(11) (2018)

[143] S. Wang, P.C. Wu, V.-C. Su, Y.-C. Lai, M.-K. Chen, H.Y. Kuo, B.H. Chen, Y.H. Chen, T.-T. Huang, J.-H. Wang, et al., A broadband achromatic metalens in the visible. *Nature Nanotechnology* **13**(3), 227–232 (2018)

[144] F. Balli, M.A. Sultan, S.K. Lami, J.T. Hastings, A hybrid achromatic metalens. *Nature Communications* **11**(1) (2020)

[145] B. Yu, J. Wen, X. Chen, D. Zhang, An achromatic metalens in the near-infrared region with an array based on a single nano-rod unit. *Applied Physics Express* **12**(9), 092003 (2019)

[146] Q. Cheng, M. Ma, D. Yu, Z. Shen, J. Xie, J. Wang, N. Xu, H. Guo, W. Hu, S. Wang, et al., Broadband achromatic metalens in terahertz regime. *Science Bulletin* **64**(20), 1525–1531 (2019)

[147] S. Wang, P.C. Wu, V.-C. Su, Y.-C. Lai, C. Hung Chu, J.-W. Chen, S.-H. Lu, J. Chen, B. Xu, C.-H. Kuan, et al., Broadband achromatic optical metasurface devices. *Nature Communications* **8**, 187 (2017)

[148] Z. Lin, S.G. Johnson, Overlapping domains for topology optimization of large-area metasurfaces. *Opt. Express* **27**(22), 32445–32453 (2019)

[149] D. Werdehausen, S. Burger, I. Staude, T. Pertsch, M. Decker, General design formalism for highly efficient flat optics for broadband applications. *Opt. Express* **28**(5), 6452–6468 (2020)

[150] A. Ozer, N. Yilmaz, H. Kocer, H. Kurt, Polarization-insensitive beam splitters using all-dielectric phase gradient metasurfaces at visible wavelengths. *Opt. Lett.* **43**(18), 4350–4353 (2018)

[151] D.M. Pozar, Flat lens antenna concept using aperture coupled microstrip patches. *Electronics Letters* **32**(23), 2109–2111 (1996)

[152] D.A.B. Miller, Fundamental limit to linear one-dimensional slow light structures. *Phys. Rev. Lett.* **99**(20), 203903 (2007)

[153] R.S. Tucker, P.-C. Ku, C.J. Chang-Hasnain, Slow-light optical buffers: capabilities and fundamental limitations. *Journal of Lightwave Technology* **23**(12), 4046–4066 (2005)

[154] J. Khurgin, Bandwidth limitation in slow light schemes. In: J. Khurgin, R.S. Tucker (eds.) *Slow Light: Science and Applications*, pp. 293–320. CRC Press, Taylor & Francis Group, Boca Raton, FL, United States (2008). Chap. 15

[155] A.A. Fathnan, D.A. Powell, Bandwidth and size limits of achromatic printed-circuit metasurfaces. *Opt. Express* **26**(22), 29440–29450 (2018)

[156] A.A. Fathnan, A.E. Olk, D.A. Powell, Bandwidth limit and synthesis approach for single resonance ultrathin metasurfaces. *Journal of Physics D: Applied Physics* **53**(49), 495304 (2020)

[157] J.D. Jackson, *Classical Electrodynamics*, 3rd edn. Wiley, New York, NY, United States (1999)

[158] S.A. Mann, D.L. Sounas, A. Alù, Nonreciprocal cavities and the time-bandwidth limit. *Optica* **6**(1), 104–110 (2019)

[159] H. Liang, A. Martins, B.-H.V. Borges, J. Zhou, E.R. Martins, J. Li, T.F. Krauss, High performance metalenses: numerical aperture, aberrations, chromaticity, and trade-offs. *Optica* **6**(12), 1461–1470 (2019)

[160] E. Arbabi, A. Arbabi, S.M. Kamali, Y. Horie, A. Faraon, Controlling the sign of chromatic dispersion in diffractive optics with dielectric metasurfaces. *Optica* **4**(6), 625–632 (2017)

[161] C. Pfeiffer, A. Grbic, Metamaterial Huygens' surfaces: Tailoring wave fronts with reflectionless sheets. *Phys. Rev. Lett.* **110**(19), 197401 (2013)

[162] F. Monticone, N.M. Estakhri, A. Alù, Full control of nanoscale optical transmission with a composite metascreen. *Phys. Rev. Lett.* **110**(20), 203903 (2013)

[163] A. Epstein, G.V. Eleftheriades, Huygens' metasurfaces via the equivalence principle: design and applications. *J. Opt. Soc. Am. B* **33**(2), 31–50 (2016)

[164] J.C. Wyant, K. Creath, Basic Wavefront Aberration Theory for Optical Metrology. In: R.R. Shannon, J.C. Wyant (eds.) *Applied Optics and Optical Engineering, Volume XI*, vol. 11. Academic Press, San Diego, CA, United States (1992)

[165] J.W. Hardy, Adaptive optics for astronomical telescopes. In: *Adaptive Optics for Astronomical Telescopes*, pp. 104–134. Oxford University Press, Oxford, United Kingdom (1998). Chap. 4

[166] F. Aieta, P. Genevet, M. Kats, F. Capasso, Aberrations of flat lenses and aplanatic metasurfaces. *Opt. Express* **21**(25), 31530–31539 (2013)

[167] R.M. Fano, Theoretical limitations on the broadband matching of arbitrary impedances. *Journal of the Franklin Institute* **249**(1), 57–83 (1950)

[168] F. Monticone, A. Alù, Invisibility exposed: physical bounds on passive cloaking. *Optica* **3**(7), 718–724 (2016)

[169] S. Abdollahramezani, O. Hemmatyar, H. Taghinejad, A. Krasnok, Y. Kiarashinejad, M. Zandehshahvar, A. Alù, A. Adibi, Tunable nanophotonics enabled by chalcogenide phase-change materials. *Nanophotonics* **9**(5), 1189–1241 (2020)

[170] S.A. Tretyakov, *Analytical Modeling in Applied Electromagnetics*. Artech House, Norwood, MA, United States (2003)

[171] S. Colburn, A. Zhan, A. Majumdar, Metasurface optics for full-color computational imaging. *Science Advances* **4**(2), 2114 (2018)

[172] L. Huang, J. Whitehead, S. Colburn, A. Majumdar, Design and analysis of extended depth of focus metalenses for achromatic computational imaging. *Photonics Research* **8**(10), 1613 (2020)

[173] T. Siefke, S. Kroker, K. Pfeiffer, O. Puffky, K. Dietrich, D. Franta, I. Ohlídal, A. Szeghalmi, E.-B. Kley, A. Tünnermann, Materials pushing the application limits of wire grid polarizers further into the deep ultraviolet spectral range. *Advanced Optical Materials* **4**(11), 1780–1786 (2016)

[174] R.C. Devlin, M. Khorasaninejad, W.T. Chen, J. Oh, F. Capasso, Broadband high-efficiency dielectric metasurfaces for the visible spectrum. *Proceedings of the National Academy of Sciences* **113**(38), 10473–10478 (2016)

[175] E.D. Palik, *Handbook of Optical Constants of Solids* vol. 3. Academic Press, San Diego, CA, United States (1998)

[176] R. Ferrini, M. Patrini, S. Franchi, Optical functions from 0.02 to 6 eV of AlxGa1-xSb/GaSb epitaxial layers. *Journal of Applied Physics* **84**, 4517–4524 (1998)

[177] A.I. Lvovsky, J. Mlynek, Quantum-optical catalysis: Generating nonclassical states of light by means of linear optics. *Phys. Rev. Lett.* **88**(25), 250401 (2002)

[178] S. Konno, W. Asavanant, F. Hanamura, H. Nagayoshi, K. Fukui, A. Sakaguchi, R. Ide, F. China, M. Yabuno, S. Miki, et al., Logical states for fault-tolerant quantum computation with propagating light. *Science* **383**(6680), 289–293 (2024)